Laser spectroscopy of nickel isotopes with a new data acquisition system at ISOLDE

Laserspektroskopie von Nickelisotopen mit einem neuen Datenaufnahmesystem an ISOLDE
Zur Erlangung des Grades eines Doktors der Naturwissenschaften (Dr. rer. nat.)
genehmigte Dissertation von Simon Kaufmann aus Koblenz
Tag der Einreichung: 05.09.2019, Tag der Prüfung: 04.11.2019
Darmstadt — D 17

1. Gutachten: Prof. Dr. Wilfried Nörtershäuser
2. Gutachten: Prof. Dr. Thomas Aumann

TECHNISCHE
UNIVERSITÄT
DARMSTADT

LASER
SpHERe

Laser spectroscopy of nickel isotopes with a new data acquisition system at ISOLDE
Laserspektroskopie von Nickelisotopen mit einem neuen Datenaufnahmesystem an ISOLDE

Genehmigte Dissertation von Simon Kaufmann aus Koblenz

1. Gutachten: Prof. Dr. Wilfried Nörtershäuser
2. Gutachten: Prof. Dr. Thomas Aumann

Tag der Einreichung: 05.09.2019
Tag der Prüfung: 04.11.2019

Darmstadt — D 17

Erklärung zur Dissertation

Hiermit versichere ich, die vorliegende Dissertation ohne Hilfe Dritter nur mit den angegebenen Quellen und Hilfsmitteln angefertigt zu haben. Alle Stellen, die aus Quellen entnommen wurden, sind als solche kenntlich gemacht. Diese Arbeit hat in gleicher oder ähnlicher Form noch keiner Prüfungsbehörde vorgelegen.

Darmstadt, den 11ten November, 2019

(Simon Kaufmann)

Bitte zitieren Sie dieses Dokument als:
URN: urn:nbn:de:tuda-tuprints-92866
URL: http://tuprints.ulb.tu-darmstadt.de/9286

Dieses Dokument wird bereitgestellt von tuprints,
E-Publishing-Service der TU Darmstadt
http://tuprints.ulb.tu-darmstadt.de
tuprints@ulb.tu-darmstadt.de

Die Veröffentlichung steht unter folgender Creative Commons Lizenz:
Namensnennung – Weitergabe unter gleichen Bedingungen 4.0 International
https://creativecommons.org/licenses/by-sa/4.0/deed.de

Abstract

Collinear laser spectroscopy is a versatile technique to study properties of nuclear ground states by the signature of nuclear structure encoded in the optical spectrum. Its sensitivity has been recently improved by the combination with bunched and cooled beams delivered from gas filled radio frequency quadrupole ion traps. In this work a new Data Acquisition (DAQ) system called TILDA (TrIga Laser Data Acquisition) was developed at the TRIGA research reactor in Mainz and transferred to the COLLAPS experiment at ISOLDE/CERN where it was applied for the first time for laser spectroscopy of Ni isotopes. TILDA is based on an Field Programmable Gate Array (FPGA) and allows to resolve the time structure of the resonance signal while the bunch traverses the optical detection region with a time resolution of 10 ns. This allows for a detailed analysis of the bunch structure during the measurement but also in the off-line analysis.
With the new DAQ system, the proton magic nickel ($Z = 28$) chain was investigated and the isotopes $^{58-68,70}$Ni were measured at the COLLAPS experiment in the [Ar]3d^9[^{2}D$_{5/2}$]4s ^{3}D$_3$→[Ar]3d^9[^{2}D$_{5/2}$]4p ^{3}P$_2$ transition of neutral nickel. The change in the mean-square charge radius δr_c^2 was extracted relative to the reference isotope ^{60}Ni. An increase in the differential change in δr_c^2 across the neutron sub-shell gap at $N = 40$ is observed. Results are compared with nuclear density functional theory calculations and show surprisingly less agreement than in other elements across shell closures in Ca, Cd, Sn or Pb. The isotope ^{68}Ni is of special interest. It is now the first short-lived isotope in which the root-mean-square charge radius r_c and the dipole polarizability are known and this provides a benchmark to investigate the predictive power of several interactions based on chiral effective field theory embodied in coupled-cluster calculations. This is shown in this work in comparison to a similar test case in the doubly magic ^{48}Ca. In both cases, theory matched the experimental findings when 3-particle-3-hole excitations in the ground state were included in the coupled-cluster calculations. The determined hyperfine structure constants agree with the literature and are up to two orders of magnitude more precise than the previous values. The extracted moments indicate a strongly mixed wave-function especially at the $I = 3/2$ states but a single-particle like behavior in the $I = 1/2$ isotopes especially for ^{67}Ni right at the sub-shell closure.

Zusammenfassung

Kollineare Laserspektroskopie ist eine vielseitige Technik zur Untersuchung von Kern Grundzustandseigenschaften anhand der Signaturen die durch die Kernstruktur im optischen Spektrum, hervorgerufen wird. Die Empfindlichkeit/Leistungsfähigkeit dieser Technik konnte zuletzt durch die Verwendung von gepulsten gekühlten Ionenstrahlen mittels Gas gefüllter linearen Radiofrequenz-Quadrupol-Ionenfallen, die dem Akkumulieren und Kühlen der Ionen dienen, signifikant gesteigert werden. In dieser Arbeit wurde ein neues Datenaufnahmesystem mit dem Namen TILDA (TrIga Laser Data Acquisition) am TRIGA Forschungsreaktor in Mainz entwickelt. Dieses wurde dann an das COLLAPS Experiment, welches sich an ISOLDE/CERN befindet, übertragen und kam dort im Rahmen der Laserspektroskopie an Nickel zu seinem ersten Einsatz. TILDA basiert auf rekonfigurierbarer Hardware (Field Programmable Gate Array (FPGA)) und erlaubt eine zeitliche Auflösung der Fluoreszenzsignale von bis zu 10 ns. Dies ermöglicht eine detaillierte Analyse der zeitlichen Struktur der Ionenpulse, die sowohl bei der experimentellen Optimierung als auch bei der späteren Analyse extrem hilfreich ist.

Mit dem neuen Datenaufnahmesystem wurden die Nickelisotope ($Z = 28$) $^{58-68,70}$Ni an ISOLDE untersucht. Die Spektroskopie erfolgte im $[\mathrm{Ar}]3d^9[^2\mathrm{D}_{5/2}]4s\,^3\mathrm{D}_3 \rightarrow [\mathrm{Ar}]3d^9[^2\mathrm{D}_{5/2}]4p\,^3\mathrm{P}_2$ Übergang neutraler Nickelatome. Die Änderung des mittleren quadratischen Ladunsgradius δr_c^2 relativ zum Referenzisotop ^{60}Ni wurde aus der Isotopieverschiebung extrahiert. Der Trend der Ladungsradien zeigt einen leichten Knick bei ^{68}Ni ($N = 40$), welches ein Indiz für einen Unterschalenabschluss darstellt. Die Ergebnisse wurden mit Berechnungen der Kern-Dichtefunktionaltheorie (nDFT) verglichen. Diese waren in der Beschreibung der Ladungsradien von Ca, Cd, Ni und Pb überaus erfolgreich, können die Daten der Nickelisotope aber nicht in vergleichbarer Güte wiedergeben. Die Ergebnisse für das Isotop ^{68}Ni sind von besonderen Interesse: es ist das erste kurzlebige Isotop, für das nun sowohl der Kern-Ladungsradius r_c, als auch die Dipol-Polarisierbarkeit gemessen wurde. Damit stellt es einen hervorragenden Test für die Vorhersagekraft verschiedener Wechselwirkungen der chiralen effektiven Feldtheorie (χEFT) im Rahmen von Coupled-Cluster (CC) Berechnungen dar. In dieser Arbeit wird dieser Vergleich parallel zu dem sehr ähnlichen Fall des doppelt magischen ^{48}Ca präsentiert. Es zeigt sich in beiden Fällen, dass eine Berücksichtigung von 3-Teilchen-3-Loch Anregungen die Berechnungen deutlich beeinflussen und zu einer besseren Übereinstimmung mit den experimentellen Werten führen.

Die ermittelten Hyperfeinstrukturkonstanten stimmen sehr gut mit den Literaturwerten überein und sind bis zu zwei Größenordnungen genauer. Die extrahierten Momente weisen auf stark gemischte Wellenfunktionen für die $I = 3/2$ Zustände hin und deutlich reinere ein-Teilchen-dominierte Wellenfunktionen für die $I = 1/2$ Zustände insbesondere für ^{67}Ni.

Contents

4. Spectroscopy of nickel at COLLAPS 43

List of Figures

List of Tables

Table of acronyms

ABMR	Atomic Beam Magnetic Resonance
AI	Analog Input
AO	Analog Output
AV18	Argonne V18 potential
CARIBU	Californium Rare Isotope Breeder Upgrade
CC	Coupled-Cluster
CEC	Charge Exchange Cell
CERN	Conseil Européen pour la Recherche Nucléaire
χ**EFT**	Chiral Effective Field Theory
CLS	Collinear Laser Spectroscopy
COALA	COllinear Apparatus for Laser spectroscopy and Applied science
COLLAPS	COLLinearly APplied Spectroscopy
COF	control FPGA

DAC	Digital-to-Analog Converter
DAF	Data Acquisition FPGA
DAQ	Data Acquisition
DMAC	Direct Memory Access Controller
EDF	Energy Density Functional
FAIR	Facility for Antiproton and Ion Research
FPGA	Field Programmable Gate Array
GPS	General Purpose Separator
GSI	GSI Helmholtzzentrum für Schwerionenforschung
HDL	Hardware Description Language
HFB	Hartree-Fock-Bogoliubov
HRS	High-Resolution Separator
HSB	High-voltage Switch Box
INL	Integrated Non Linearity
ISCOOL	ISolde COOLer
ISOLDE	Isotope Separator OnLine DEvice
LEC	Low-Energy Constant
LSB	Least Significant Bit
MCP	Master Control Program
MSU	Michigan State University
nDFT	nuclear Density Functional Theory
NI	National Instruments
NIM	Nuclear Instrumentation Module
NMR	Nuclear Magnetic Resonance
NSCL	National Superconducting Cyclotron Facility
ODR	Optical Detection Region
PMT	Photomultiplier-Tube
PolliFit	Python cOLLInear FITter
PPG	Pulse Pattern Generator

PSB Proton Synchrotron Booster

PXI PCI eXtensions for Instrumentations

QCD Quantum Chromo Dynamics

RIB Radioactive Ion Beam

RIS Resonance Ionization Spectroscopy

RFQCB Radio Frequency Cooler and Buncher

SEM Secondary Electron Multiplier

SPI Serial Peripheral Interface

TILDA TrIga Laser Data Acquisition

TOF Time Of Flight

TTL Transistor-Transistor Logic

TRIGA Training Research Isotopes General Atomics

TRITON TRIga pyThon cONtrol

1 Introduction

Nuclear physics has flourished since Rutherford's [Rut11] scattering experiment a little bit more than 100 years ago, in which he could prove the existence of the compact nucleus within the center of an atom. While data of alpha particles at low energy and small scattering angles could be well explained by Coulomb scattering at a point-like positive charge, deviations appeared at higher energies and large scattering angles. This could be interpreted as the effect of the strong interaction at very short distances and gave a first idea of the nuclear size. It turned out that the compact object inside the nucleus has a diameter of a few femtometers (Fermi). Nuclear reactions mediated by the strong force are still today a tool to determine the matter radii of nuclei but require a nuclear model-dependent description of the interaction process. It should be noted that nuclear charge exchange reactions have also been used to extract charge radii [Bla92; Yam11] but do not provide a precision as high as electromagnetic techniques.
In the 1950th the technique of elastic electron scattering was developed by Hofstadter et al. to determine the charge radius of stable nuclei [Hof56]. An electron interacts primarily electromagnetically with the nucleus (besides a very small contribution of the weak force) and allows to measure the electromagnetic form factor from which the mean-square nuclear charge radius can be extracted from the behavior at very low momentum transfer. Another important source of information were X-rays in muonic atoms that also allowed to determine nuclear charge radii. Energies of K-α and other X-ray transitions are sensitive to the so-called Barrett radii, which can be translated into mean-square charge radii when combined with information from elastic electron scattering [Fri04]. Both methods have been used so far only for stable isotopes (apart from the rather long-lived cases ^{3}H, ^{14}C, ^{41}Ca), but ideas to study elastic electron scattering on unstable nuclei in storage rings have been worked out and are under development at the SCRIT Electron Scattering Facility at RIKEN where proof-of-principle studies were performed with stable isotopes (^{208}Pb and ^{132}Xe) [Sud17] and have also been included in the conceptual design report for FAIR (Facility for Antiproton and Ion Research).
The most precise and nuclear-model independent technique to extract nuclear charge radii of unstable isotopes is laser spectroscopy. The hyperfine structure of an atomic spectrum reveals substantial information on the nuclear structure. While the hyperfine splitting allows to determine the nuclear spin, the magnetic dipole moment and the electric quadrupole moment of a nucleus, the so-called isotope shift provides access to the nuclear charge radius. This was already known early in the last century and indeed the isotope shift between hydrogen and its heavier isotope ^{2}H was employed in the discovery of deuterium for which Harold Urey received the Nobel prize in Chemistry in 1934. Optical spectroscopy of short-lived isotopes became a vivid field with the application of lasers and the development of Collinear Laser Spectroscopy (CLS) [Kau76], which was first realized for this purpose at the Training Research Isotopes General Atomics (TRIGA) reactor in Mainz in 1978 [Sch78] and then quickly introduced at ISOLDE/CERN in 1979 [Neu81a; Neu81b]. At the end of the 1980's, the on-line application of Resonance Ionization Spectroscopy (RIS) was suggested and developed in parallel in Mainz [Neu86] and in Dubna [Let87] and became the second working horse for these kind of investigations. The success of these approaches is documented in Fig. 1.1 which shows a nuclear chart with the long chains of isotopes (red) which have been investigated by laser spectroscopy online. From these studies a wealth of nuclear structure information was harvested, reaching from

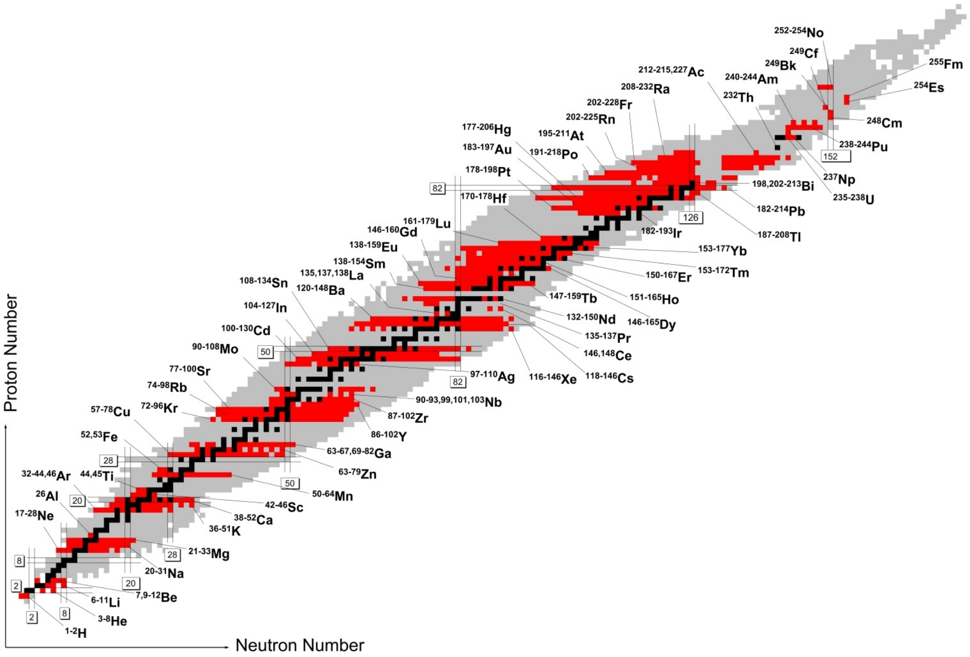

Figure 1.1.: Chart of nuclides with all optically measured radionuclides depicted in red for the radio active ones and black for the stable ones. Taken from the LaserSphere homepage[1].

shape coexistence in the mercury region [Bon72], across the odd-even staggering to the famous kinks of nuclear charge radii trends at magic numbers [Sor08]. Also, long-lived nuclear isomers can be studied and the isomer shift can reveal the small differences in charge radii between nuclear ground and excited states as it was demonstrated, e.g. in [Yor16].

The collinear laser spectroscopy station at the Isotope Separator OnLine DEvice (ISOLDE) operated by the COLLinearly APplied Spectroscopy (COLLAPS) collaboration is now in use for exactly 40 years and is still one of the most productive places for on-line laser spectroscopy [Neu17].

Its performance has been boosted considerably with the introduction of the radiofrequency cooler and buncher ISolde COOLer (ISCOOL) [Fra08]. This device allows to accumulate rare species in a longitudinally segmented gas-filled linear Paul trap for some time, typically some milliseconds and to then extract short bunches of ions that have microseconds length and therefore decrease background from scattered laser light by up to four orders of magnitude. This technique was developed at Jyväskylä [Nie02] and is now applied at many on-line facilities. While first studies at COLLAPS using ISCOOL where still carried out with the old Data Acquisition (DAQ) system developed at the end of the 1990's, it became clear that an improved DAQ system would be highly desirable. Within this thesis an entirely new DAQ system was developed and tested at the collinear beamline TRIGA-LASER at the TRIGA reactor in the Institute of Nuclear Chemistry at the Johannes Gutenberg-University Mainz, from where it earned its name: TILDA, standing for TrIga Laser Data Acquisition. TILDA is based on reprogrammable hardware using an Field Programmable Gate Array (FPGA) embedded in a commercial PCI eXtensions for Instrumentations (PXI)-system in order to minimize the hardware development branch, but still have a high-level of flexibility in order to adapt it to future developments in the experiment.

---

[1] `https://www.ikp.tu-darmstadt.de/gruppen_ikp/ag_noertershaeuser/research_wn/exotic_nuclei_wn/uebersicht_2/laserspectroscopy_survey.de.jsp`

The time-resolving features are handled by the real-time calculations on the FPGA, hence the operating system can run asynchronously with a standard operating system. The programming was chosen with high-level languages in order to have new developers get settled in quickly. The host part is programmed using the nowadays common language python and the programming of the FPGA is realized using Labview. After its development, TILDA was installed at COLLAPS and applied in the spectroscopy of nickel isotopes and the results are documented in this work. The focus here lies on the investigation of nuclear charge radii, while the nuclear moments are presented but not discussed in depth, since they will be part of another work. The interest in charge radii of the nickel isotopes is threefold:

(A) The possible sub-shell closure at $N = 40$ can be revealed by a kink in the charge radius at ^{68}Ni. Indications have been seen in the neighboring elements Cu and Zn [Bis16; Xie18] and it is expected to be pronounced in nickel, as indicated by the relativley high energy of the first 2^+ state in ^{68}Ni [Bro95]. The precise reason for this is still under discussion [Pau08; Pau10], although it could be debated that the parity change from the νpf to the $\nu g_{9/2}$ is mostly responsible for this effect [Lan03]. Mass measurements across $N = 40$ could not find any evidence for a significant sub-shell closure [Gue07; Rah07], so it is very interesting to see what the radii of this isotonic sequence will reveal around this sub-shell closure.

(B) New nuclear structure models recently provided an improved description of nuclear charge radii. Particularly successful were models based on Chiral Effective Field Theory (χEFT) and nuclear Energy Density Functional (EDF) theory. χEFT is an ab-initio approach closely linked to the underlying Quantum Chromo Dynamics (QCD) and provides the interaction between nucleons by an effective Lagrangian which is expressed in nucleons and pions [Ent03; Epe09; Mac11; Eks15]. Today the most successful χEFT interactions are using three nucleon (3N) forces and the best results are obtained in the vicinity of doubly magic shell closures. Recently the experimental results in neutron-rich calcium showed a good agreement with these calculations [GR16], but could not describe the fast rise of radii towards ^{52}Ca, neither could any other theory at that time. The EDF theory is using a different approach by creating a nuclear mean-field and effective interactions are employed by carefully tuning the parametrizations to experimental results [Ben03; Dug14]. This has been very successful all across the chart of nuclides. This semi empirical approach requires an updated fine tuning from time to time due to new experimental findings, as it was the case recently for the Fayans [Fay00] parametrization, which was optimized to the new findings in calcium [Rei17]. This lead to the *activation* of its gradient term and its predictive power showed very good results not only in Ca, but also in Cd, Sn and Pb [Mil19; Ham18; Gor19]. The Ni region is currently at the forefront of χEFT for radii and therefore an ideal testing ground since this works best at magic numbers and for EDF it is in the middle between the two regions where it has been successfully employed.

(C) A third motivation is the fact that ^{68}Ni is the only radioactive isotope for which the dipole polarizability α_D has been measured so far. Work on Ca revealed a strong correlation of this property with the nuclear charge radius in the investigated χEFT-interactions [Hag15]. The dipole polarizability in ^{48}Ca was recently measured [Bir17] and showed that the predicted α_D from the correlation to the charge radius was in good agreement with the value for α_D extracted from the α_D-charge radius correlation. This was further improved, when the theoretical calculations were extended by including also 3-particle-3-hole (3p-3h) excitations in the ground state [Mio18]. The dipole polarizability ^{68}Ni measured by Rossi et al. and expanded to the full energy scale by Roca-Maza et al. [Ros13; RM15] is a good benchmark to test the predictive power of this correlation in a radioactive isotope.

2 Theory

This section will focus on the theoretical background required for this work. In collinear Laser spectroscopy energy levels in an atom are probed by using lasers and to obtain the underlying nuclear structure, namely the nuclear spin, the electrical quadrupole moment, the magnetic dipole moment and the nuclear charge radius. This is possible due to the appearance of the hyperfine interaction that represents all nuclear effects influencing the atomic energy levels apart from the central Coulomb force of a point-like infinitely heavy nucleus. Theoretical nuclear aspects will be covered first by the relevant theories necessary to follow the discussion in the experimental results section. The interaction of the nickel atoms with the laser and the involved atomic theory backgrounds will be discussed in the atomic theory in chapter 2.2 followed by chapter 2.3 focusing on the basis of collinear laser spectroscopy.

2.1 Nuclear theory

Understanding nuclear structure has been an ongoing endeavour of nuclear theorists for many decades but so far no universal theory could be developed that covers the full nuclear landscape. While the fundamental theory of Quantum Chromo Dynamics (QCD) is known and is used successfully for high-energy physics calculations, the low-energy frontier is still at the level of the structure of individual nucleons. In order to calculate the structure of the lightest nuclei, effective nucleon-nucleon forces have to be used. Those can be derived from interaction potentials motivated by the properties of QCD and parameters fitted to nucleon-nucleon scattering data, like e.g. the Argonne V18 potential (AV18) [Wir95]. Alternatively, Chiral Effective Field Theory (χEFT) can be used to establish interaction potentials. In both cases, three-body forces are required to describe the structure of even the simplest nuclei. These have to be established ad-hoc and to be fitted to the respective two-body interactions, like in the case of the Illinois potentials that come along with the AV18. Contrary, χEFT offers a systematic way of establishing the three-body forces and improve the theory by including increasing orders (LO, NLO, NNLO, N^3LO, etc.) in the interaction. Also here some properties of the lightest nuclei have to be used to determine the low-energy constants. Applying such potentials in nuclear structure calculations, is referred to as an *ab-initio nuclear structure approach*. With increasing nuclear mass, such calculations become increasingly difficult and it was only recently possible to extend them beyond the oxygen region.

The most important microscopic nuclear structure theory in the range of medium masses is the nuclear shell-model which will be described in chapter 2.1.2. Another very successful semi empirical microscopic model is the nuclear energy density functional theory which will be discussed in chapter 2.1.3. But first, the more ordinary droplet model will be discussed since it is later used in the discussion.

2.1.1 Liquid drop and droplet model

In the liquid drop model the nucleus is seen as a liquid with a sharp boundary and a homogeneus distribution of protons and neutrons within the drop [Bet08]. One of the outcomes of

Table 2.1.: Parameters for the calculation of the mean-square charge radius of a spherical nuclei in the droplet model.

parameter	value	description
r_0	1.18 fm	nuclear radius constant
b	0.99 fm	nuclear diffuseness
c_1	0.7322 MeV	Coulomb energy coefficient
a_2	20.69 MeV	surface energy coefficient
J	36.8 MeV	symmetry energy coefficient
Q	17 MeV	effective surface stiffness
K	240 MeV	compressibility coefficient
L	100 MeV	density symmetry coefficient

this model is the *Bethe-Weizsäcker-Mass-formula* which yields the binding energies across the nuclear chart in a good approximation.

A refined model, called the droplet model, was developed that differentiates between the neutron and proton distribution and softens the edge of the drop by taking a surface diffuseness into account [Mey83]. The mean-square (ms) charge radius $\langle r_c^2\rangle$ can be calculated based on this model and since it provides a comparison for the results obtained by Collinear Laser Spectroscopy (CLS), this parametrization will be summarized for spherical nuclei in the following.

The size of the droplet (including protons and neutrons) is given as

$$R = r_0 A^{1/3}(1+\epsilon), \tag{2.1}$$

with

$$\epsilon = (-2a_2 A^{-1/3} + L\delta^2 + c_1 Z^2 A^{-4/3})/K, \tag{2.2}$$

$$\delta = \frac{I + \frac{3}{16}(c_1/Q)ZA^{-2/3}}{1+\frac{9}{4}(J/Q)A^{-1/3}}, \tag{2.3}$$

$$I = (N-Z)/A. \tag{2.4}$$

r_0 is the nuclear radius constant, c_1 is the Coulomb- energy coefficient and the other parameters describe the properties of a drop, like the compressibility coefficient K and are listed in the Table 2.1 from [Mey83]. The neutron-skin thickness is given by $t = \frac{2}{3}R(I-\delta)$ and the radii R_n of the neutron distribution and R_p for the proton distribution can be calculated by

$$R_n = R + \frac{Z}{A}t, \quad R_p = R - \frac{N}{A}t. \tag{2.5}$$

Using the proton radius R_p one can calculate the ms charge radius $\langle r_c^2\rangle$ with the following expression

$$\langle r_c^2\rangle = \langle r_c^2\rangle_u + \langle r_c^2\rangle_r + \langle r_c^2\rangle_d, \tag{2.6}$$

where

$$\langle r_c^2 \rangle_u = \frac{3}{5} R_p^2 \tag{2.7}$$

is the contribution from the size of the uniform distribution.

$$\langle r_c^2 \rangle_r = \frac{12}{175} C R_p^2 \tag{2.8}$$

is the contribution of the redistribution of the protons within the nucleus and C is proportional to the number of protons Z. The last term corresponds to the diffuseness of the nuclear surface

$$\langle r_c^2 \rangle_d = 3b^2. \tag{2.9}$$

This mean-square charge radius is assuming a spherical nucleus and in reality this is only approximately valid in the vicinity of a closed neutron-/proton shell. Deformations of the nucleus in between shell closures will become visible by an increased mean-square charge radius which deviates from the spherical mean-square charge radius in Eq. (2.6). This could be shown in the neighboring isotopic chains of Cu and Ga [Bis16] and will be used again in the discussion of the nickel results in chapter 6.

2.1.2 Nuclear shell model

Early on in nuclear physics, it was noticed that certain numbers of neutrons and protons seem to result in a more stable nucleus than their neighboring nuclides. For example it was noted, that elements like helium, oxygen, calcium and nickel occur in a relative large amount within the universe. Another observable for the strengthened stability is often an increased binding energy per nucleon. These proton and neutron numbers are the so called *magical* numbers 2, 8, 20, 28, 50, 82 and 126 where the separation and excitation energies are especially high corresponding to their neighbors. Magical numbers cannot be explained by the droplet model, but since they seem similar to the noble gases in the atomic shell theory, with their increased ionization and first excitation energy, the nuclear shell theory was derived. But in contrast to the atomic shell, no central potential is existing in the nucleus, but the short-ranged strong nuclear force is dominant which acts between each pair of nucleons. Nucleons cannot collide due to their fermionic nature and therefore one can assume that each nucleon moves freely in a mean potential created by the remaining nucleons. Hence, the potential depends on the density distribution of the nucleons in the nucleus. For heavy nuclei the potential is often approximated by the *Woods-Saxon* potential

$$V_{\mathrm{WS}}(r) = \frac{-V_0}{1 + \exp\left((r - R)/a\right)} , \tag{2.10}$$

with a as a fit-parameter for the diffuseness in the nuclear skin and R as the size of the nucleus. By filling the shells according to the Pauli principle, the first three magic numbers (2, 8 and 20) can be explained by this model. Higher magic numbers were explained by taking a spin-orbit coupling into account, in a similar way as in the atomic electromagnetic interaction [GM48;

GM49]. The spin **s** couples with the orbital angular momentum **l** to a total angular momentum $j = l \pm s$. Adding this effect to the *Woods-Saxon* potential gives a new potential with the form

$$V(r) = V_{\text{WS}}(r) + V_{ls}(r)\frac{\langle \mathbf{l} \cdot \mathbf{s} \rangle}{\hbar^2}. \tag{2.11}$$

The expectation values of the coupling

$$\frac{\langle \mathbf{l} \cdot \mathbf{s} \rangle}{\hbar^2} = \frac{j(j+1) - l(l+1) - s(s+1)}{2} = \begin{cases} l/2 & \text{for } j = l + 1/2 \\ -(l+1)/2 & \text{for } j = l - 1/2 \end{cases} \tag{2.12}$$

lead to an energy splitting $\Delta E_{ls} \propto l + 1/2$ and Figure 2.1 shows the resulting energy levels for protons and neutrons. At the encircled magic numbers one can clearly see the wide energy gaps between the two energy levels. Nuclei with a magic proton- and neutron number are called doubly magic and are almost spherical. For example, nickel has two doubly magic nuclei, ^{56}Ni ($Z = N = 28$) and ^{78}Ni ($N = 50$) the latter one just recently being confirmed as doubly magic by mass measurements in copper [Wel17] and γ-spectroscopy [Tan19]. Realistically though, not only one of these states will be occupied, but usually a configuration mixture is assumed even in single-particle calculations. Depending on the complexity of the system a lot of possibilities have to be accounted for, thus the computing times can become challenging for complex nuclear systems.

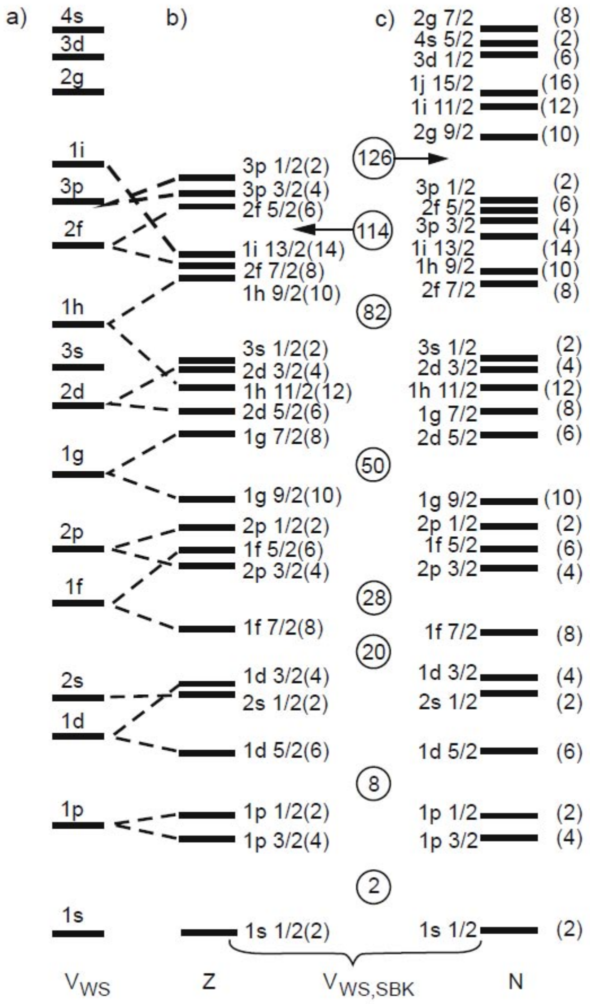

Figure 2.1.: Energy levels calculated from the single particle shell model using a) the Woods-Saxon potential and b) the spin-orbit coupling of the protons and c) the neutrons [Bet08].

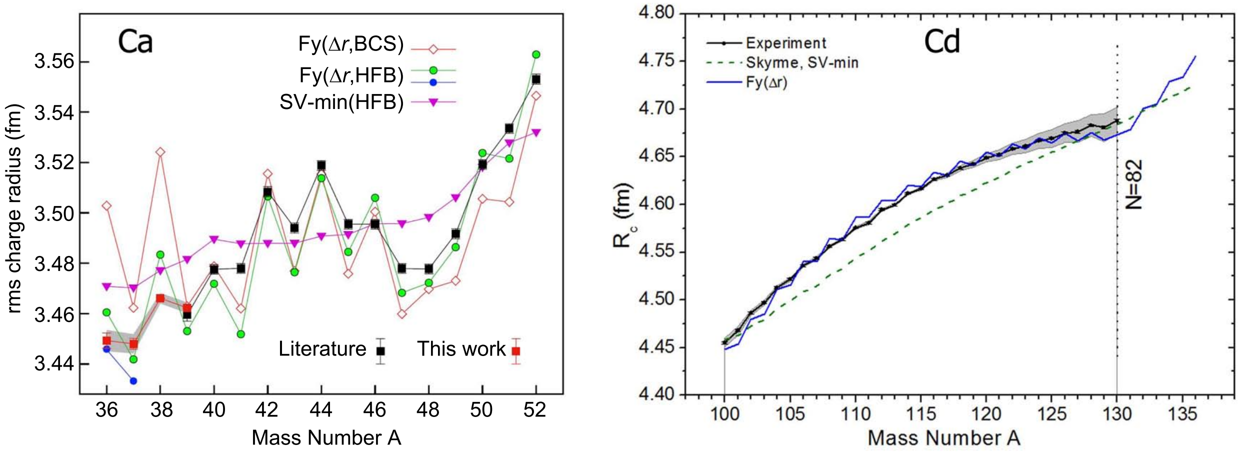

Figure 2.2.: Left: Root-mean-square (rms) charge radii of the calcium isotopes $^{36-52}$Ca [Mil19]. Right: Cadmium isotopes $^{100-130}$Cd [Ham18]. Each in comparison to EDF calculations.

EDF theory [Ben03; Dug14] is a very successful tool for calculating nuclear ground state properties across the chart of nuclides. The global description of medium- and heavy mass nuclei to a microscopic level is one of the key features of the EDF theory. In complex nuclei, ab-initio calculations are not feasible, hence, the EDF approach is realized by establishing a nuclear mean-field and employing effective interactions with parameters that are carefully tuned to empirical results. The nuclear mean-field is usually calculated by the Hartree-Fock-Bogoliubov (HFB) method and several effective energy functionals have been developed based on this. Here we will discuss the widely-used Skyrme functional in order to illustrate the idea of the EDF theory. As in the other functionals, the mean-field is created from a set of single-nucleon wave functions $\psi_i(\mathbf{x})$, with $\mathbf{x} = (\mathbf{r}, \sigma, \tau)$ (spatial coord., spin, isospin). The state of the nucleus $|\Phi\rangle$ is described in the independent-particle model, by a Slater determinant $|\Phi\rangle = \det \psi_i(\mathbf{x}), i = 1, ..., A$. In order to account for pairing correlations, the Bogoliubov transformation is introduced, which connects single-particle states to quasiparticle states:

$$\hat{b}_n^+ = \sum_i (U_{in} \hat{a}_i^+ + V_{in} \hat{a}_i), \tag{2.13}$$

with the creation operator $\hat{a}_i^+$. Now it is useful to introduce a one-body density matrix ρ and a pair tensor κ by

$$\rho_{ij} = \langle \Phi | \hat{a}_j^+ \hat{a}_i | \Phi \rangle = \rho_{ji}^* \,, \tag{2.14}$$

$$\kappa_{ij} = \langle \Phi | \hat{a}_j \hat{a}_i | \Phi \rangle = -\kappa_{ji} \,. \tag{2.15}$$

These can be seen as components of a generalized quasiparticle density

$$R = \begin{pmatrix} \rho & \kappa \\ -\kappa^* & 1 - \rho^* \end{pmatrix}. \tag{2.16}$$

Minimizing the total energy $E[\rho,\kappa,\kappa*] = \langle\Psi|\hat{H}|\Psi\rangle$ yields the ground state of the HFB $|\phi\rangle$. In reality very often effective energy density functionals $E[\rho,\kappa,\kappa*]$ are used without explicit knowledge of the underlying Hamiltonian $\hat{H}$.

The Skyrme Hartree-Fock parametrization is a local energy functional, which is expressed by local energy densities and currents: local density ρ, kinetic-energy density τ, spin-orbit density $\mathbf{J}$, current $\mathbf{j}$, spin density σ, kinetic spin density τ and pair current ξ. Each appears twice, for protons and neutrons, e.g. ρ_p and ρ_n. The formula of these local energy densities and currents would exceed the purpose of this chapter and the interrested reader is invited to find them elsewhere, e.g. in [Klü09; Dug14]. The Skyrme energy in the most general form can be written as

$$
\begin{aligned}
E =& \int d^3r(\epsilon_{\text{kin}} + \epsilon_{\text{Skyrme}}) + E_{\text{Coulomb}} + E_{\text{pair}} + E_{\text{cm}} \ , && (2.17)\\
\epsilon_{\text{kin}} =& \frac{\hbar^2}{2m_p}\tau_p + \frac{\hbar^2}{2m_n}\tau_n \ , && (2.18)\\
\epsilon_{\text{Skyrme}} =& \frac{B_0 + B_3\rho^{\alpha}}{2}\rho^2 - \frac{B_0' + B_3'\rho^{\alpha}}{2}\tilde{\rho}^2 + B_1(\rho\tau - \mathbf{j}^2)\\
& - B_1'(\tilde{\rho}\tilde{\tau} - \tilde{\mathbf{j}}^2) - \frac{B_2}{2}\rho\Delta\rho + \frac{B_2'}{2}\tilde{\rho}\Delta\tilde{\rho}\\
& - \frac{1}{2}B_4[\rho\nabla\cdot\mathbf{J} + \sigma\cdot(\nabla\times\mathbf{j})]\\
& - \frac{1}{2}(B_4 + b_4')[\tilde{\rho}\nabla\cdot\tilde{\mathbf{J}} + \tilde{\sigma}\cdot(\nabla\times\tilde{\mathbf{j}})]\\
& + \frac{C_1}{2}(\mathbf{J}^2 - \sigma\cdot\tau) - \frac{C_1'}{2}(\tilde{\mathbf{J}}^2 - \tilde{\sigma}\cdot\tilde{\tau}), && (2.19)\\
E_{\text{Coulomb}} =& e^2\frac{1}{2}\int d^3r d^3r' \frac{\rho_p(\mathbf{r})\rho_p(\mathbf{r}')}{|\mathbf{r}-\mathbf{r}'|}\\
& - \frac{3}{4}e^2\left(\frac{3}{\pi}\right)^{1/3}\int d^3r[\rho_p]^{4/3}, && (2.20)\\
E_{\mathbf{pair}} =& \frac{1}{4}\sum_q v_{0,q}\int d^3r\xi_q^2\left[1 - \frac{\rho}{\rho_{\text{pair}}}\right], && (2.21)\\
E_{\text{cm}} =& -\frac{1}{2mA}\langle(\hat{P}_{\text{cm}})^2\rangle, \ \ \hat{P}_{\text{cm}} = \sum_i \hat{p}_i \ . && (2.22)
\end{aligned}
$$

The scalar and vector densities ρ and $\tilde{\rho}$, respectively are given by

$$
\rho = \rho_p + \rho_n, \ \ \tilde{\rho} = \rho_p - \rho_n, \tag{2.23}
$$

and similarly for the currents and densities. The individual components are the kinetic energy ϵ_{kin}, the Skyrme term ϵ_{Skyrme}, the Hartree Coulomb term E_{Coulomb}, the pairing term E_{pair} and the center-of-mass term E_{cm}. This effective energy term is now adjusted by tuning the B_i (B_i') parameters, which set the strength of the isoscalar (isovector $\tilde{\rho}$) forces. In the SV-min parametrization, the main idea is to perform this optimization by a χ^2 minimization to an experimental set of nuclei carefully chosen [Klü09]. Nuclei around shell closures are of high interest for this data set, since they are almost spherical and do not exhibit large deformations. As observables the total binding energy E_B sticks out naturally since it is directly provided by the numerical solution of the mean-field equations. But also long-range related observables like the root-mean-square (rms) charge radius, which can be provided from laser spectroscopic measurements, are of high-interest for the fitting routine. The SV-min functional provides a reasonable description of the charge radius across the nuclear chart, but it fails to describe subtle effects like the odd-even staggering or the kink at shell closures with an appropriate magnitude.

In the aim to describe these subtle effects in the charge radius, the Fayans-EDF was developed [Fay00]. It is very similar to the Skyrme parametrization, hence the Hartree Coulomb and the kinetic energy terms are exactly the same. The major difference is, that the Fayans formalism introduces density dependent terms, which are decomposed into a volume, surface and spin-orbit term,

$$\epsilon_{\mathrm{Fy}} = \epsilon^{V}_{\mathrm{Fy}}(\rho) + \epsilon^{s}_{\mathrm{Fy}}(\rho) + \epsilon^{ls}_{\mathrm{Fy}}(\rho, \mathbf{J}). \tag{2.24}$$

Here the surface term makes a lot of a difference to Skyrme, since it involves a gradient of the density. Also the Fayans pairing functional $\epsilon^{\mathrm{pair}}_{\mathrm{Fy},q}$ is quite different to Skyrme, since it goes beyond the density-dependent ansatz and it can account for the coupling to surface vibrations. The novel density-gradient term included in this pairing functional, is the key ingredient to explain the odd-even staggering in r_{ch}. Especially after optimizing the functional with inclusion of the charge radius changes from the calcium chain (^{40,44,52}Ca), the new functional called Fy(Δr) has proven to be able to describe the steep rise of the charge radii towards ^{52}Ca [Rei17]. The success of this functional continued also on the proton rich side of calcium [Mil19], which is shown in Fig. 2.2. But not only in calcium the functional worked well, but also in other elements: The radii of Cd isotopes between the $N = 50$ and $N = 82$ shell closures was described very well [Ham18], even though with an over pronounced odd-even staggering, see also Fig. 2.2. In the even tin isotopes [Gor19] (see chapter 6) it performed very well to describe the kink at shell closure across $N = 82$. This naturally raises the question how it will perform in the nickel chain between $N = 28$ and $N = 40$. This will be discussed based on the results obtained in this work in chapter 6.1.2.

2.1.4 Coupled-cluster theory

Coupled-Cluster (CC) [Hag14] theory is an ab-initio method, which aims to solve the Schrödinger equation for a many-body system. In nuclear physics it can be linked to the underlying QCD by Chiral Effective Field Theory (χEFT) interactions including three-nucleon forces (3N). CC is very efficient in doubly magic nuclei or nuclei with a closed sub-shell structure, hence it is ideal to investigate shell evolution in semi-magic nuclei.

The starting point is a many-body wave function, which can written as an exponential ansatz

$$|\psi_0\rangle = e^{T}|\phi_0\rangle, \tag{2.25}$$

with the Slater determinant $|\phi_0\rangle$ constructed by the Hartree-Fock formalism. The cluster operator T can be expanded to

$$T = T_1 + T_2 + \cdots + T_A\,, \tag{2.26}$$

with each term T_n generating n-particle - n-hole (np-nh) excitations from the reference state. These can be expressed as

$$T_1 = \sum_{ia} t_i^a a_a^+ a_i, \tag{2.27}$$

$$T_2 = \frac{1}{4} \sum_{ijab} t_{ij}^{ab} a_a^+ a_b^+ a_j a_i, \tag{2.28}$$

$$\cdots \tag{2.29}$$

with the indices $i, j, ...$ labeling occupied single-particle (hole) states and the indices $a, b, ...$ indicate unoccupied states in the reference Slater determinant. Orbitals are labeled by p, q, r, s. $a_a^+, \ldots$ and $a_j, \ldots$ are the corresponding creation and annihilation operators. t_i^a, t_{ij}^{ab} are the amplitudes of the cluster operator, which can be obtained by solving the set of non-linear equations obtained by

$$0 = \langle \phi_i^a | \bar{H}_N | \phi_0 \rangle \tag{2.30}$$

$$0 = \langle \phi_{ij}^{ab} | \bar{H}_N | \phi_0 \rangle \tag{2.31}$$

$$\cdots . \tag{2.32}$$

Here, $\langle \phi_i^a |$, $\langle \phi_{ij}^{ab} |$, $\ldots$ are Slater determinants constructed as $1p - 1h,\ 2p - 2h,\ \ldots$ excitations from $|\phi_0\rangle$.

The Schrödinger equation of the ground state then becomes

$$\bar{H}_N |\phi_0\rangle = E_0 |\phi_0\rangle\ , \tag{2.33}$$

with the similarity-transformed normal-ordered Hamiltonian

$$\bar{H}_N = e^{-T} H_N e^T\ . \tag{2.34}$$

Here H_N is the normal ordered Hamiltonian in respect to the reference Slater determinant. The normal ordered Hamiltonian is defined for a two-body Hamiltonian

$$H = \sum_{pq} \epsilon_{pq} a_p^+ a_q + \frac{1}{4} \sum_{pqrs} \langle pq || rs \rangle a_p^+ a_q^+ a_s a_r\ , \tag{2.35}$$

as the sum $H = H_N + E_0$ with the vacuum expectation value as

$$E_0 = \sum_i \epsilon_{ii} + \sum_{ij} \langle ij || ij \rangle\ . \tag{2.36}$$

In the Hartree-Fock basis this is called the Hartree-Fock energy. The normal ordered Hamiltonian is then defined as

$$H_N = \sum_{pq} f_{pq} \{a_p^+ a_q\} + \frac{1}{4} \sum_{pqrs} \langle pq || rs \rangle \{a_p^+ a_q^+ a_s a_r\}\ , \tag{2.37}$$

with the brackets indicating the normal ordering, meaning the creation operator a^+ is always to the left of its corresponding annihilation operator a.

Expanding the cluster operator T up to $Ap - Ah$ excitations will yield an exact solution using coupled-cluster theory. In typical CC computations, the cluster operator is not expanded up to $Ap - Ah$ excitations and it has been shown that for closed (sub-) shell nuclei expansions up to only $2p - 2h$ excitations (called D for doubles) include already 90% of the correlation energy. Including triples (T) expands to about 99% of the correlation energy [Bar07; Hag09].

As an ab-initio approach to nuclear structure in the vicinity of semi-magic or doubly magic nuclei, CC theory is combined with χEFT that provide the underlying nucleon-nucleon interaction. χEFT is closely linked to the underlying QCD [Wei90; Epe09; Mac11]. Therefore effective Lagrangians, expressed in nucleons and pions are created in order to preserve the required symmetries, especially the chiral symmetry, required in the low-energy regime of the QCD. This chiral effective Lagrangian is given by an infinite series of terms and applying it to NN scattering generates an unlimited number of Feynman diagrams. Only a systematic expansion in powers of $(Q/\Lambda_\chi)^\nu$, with the pion mass or momentum Q and the chiral symmetry breaking scale $\Lambda_\chi \approx 1\,\mathrm{GeV}$, the problem becomes computable, since the number of terms becomes finite. The coefficients in this expansion are called Low-Energy Constants (LECs) responsible to embed the very short-range physics which is not resolved and they are adapted to experimental data.

The χEFT-interactions used in this work follow the notation from [Heb11] and are based in the work of Entem and Machleidt [Ent03; Mac11]. Hence they follow the naming scheme EM1-4 and the cut-off energy for the calculation is noted by $\Lambda/\Lambda_{\mathrm{3NF}}$, e.g. EM1 (2.0/2.0).

2.1.5 Nuclear moments

2.1.5.1 Magnetic dipole moment

The nuclear magnetic dipole moment arises from the spins and the orbital momenta of the involved nucleons

$$\mu_{\text{nucleus}} = \mu_{\text{N}} \cdot \frac{1}{\hbar} \sum_{i=1}^{A} (\mathbf{l}_i g_l + \mathbf{s}_i g_s) \ , \tag{2.38}$$

with the nuclear magneton $\mu_{\text{N}} = e\hbar/(2m_p c)$ and the g-factors given by [Neu06]:

$$\text{protons}: g_l = 1 \quad g_s = +5.587 \tag{2.39}$$

$$\text{neutrons}: g_l = 0 \quad g_s = -3.826. \tag{2.40}$$

Even numbers of protons or neutrons do not contribute to the magnetic moment in the ground state due to their pairing, so the magnetic moment of an even-even nucleus in its ground-state is zero, but for odd-even or even-odd nuclei, the magnetic moment is determined by the valence nucleon. Therefore Eq. (2.38) simplifies to

$$\mu_{\text{nucleus}} = \mu_{\text{N}} \cdot \frac{1}{\hbar} \langle \psi_{\text{nucleus}} | \mathbf{l} g_l + \mathbf{s} g_s | \psi_{\text{nucleus}} \rangle \ . \tag{2.41}$$

Since the g-factors differ from 1 the direction of the magnetic moment is different from the nuclear spin $\mathbf{I} = \mathbf{j}$ and processes around $\mathbf{j}$. Hence the resulting moment is the projection onto the spin axis

$$\mu_{\text{nucleus}} = g_{\text{nucleus}} \cdot \mu_N \cdot \frac{\langle \mu \cdot \mathbf{I} \rangle}{\hbar} \tag{2.42}$$

which leads to

$$\mu_{\text{nucleus}} = \left[\left(I - \frac{1}{2} \right) g_l + \frac{1}{2} g_s \right] \mu_N \qquad \text{for } \ I = l + \frac{1}{2} \tag{2.43}$$

$$\mu_{\text{nucleus}} = \frac{I}{I+1} \left[\left(I + \frac{3}{2} \right) g_l - \frac{1}{2} g_s \right] \mu_N \qquad \text{for } \ I = l - \frac{1}{2} \tag{2.44}$$

This model works quite well for light nuclei, but in heavier ones the valence nucleon leads to a polarization of the core and a corresponding contribution to the magnetic moment. Therefore it has become common to use an effective g-factor g_{eff} which is smaller than the free g-factor in order to account for this coupling as well as other effects like meson-exchange currents.

2.1.5.2 Electric quadrupole moment

The shell model assumes a nucleus with spherical symmetry, but this is only valid close to a magic number. In between shell closures and especially in half-filled shells the nucleus can become deformed and the potential is not spherically-symmetric anymore. In a mathematical representation, the charge distribution of the nucleus is described using electric multipole moments and the first non vanishing term is the quadrupole moment with the classical definition,

$$Q = \int (3z^2 - r^2)\rho(r) d^3 r \, . \tag{2.45}$$

For an ellipsoid as in Fig. 2.1.5.2 with the radius a in z direction and b for x and y directions leads to the quadrupole moment:

$$Q = \frac{2}{5} Ze(a^2 - b^2) \, . \tag{2.46}$$

Therefore, a positive quadrupole moment means, that a is larger than b, which is called a *prolate* shape and if the opposite is the case it is called an *oblate* shape. Across the nuclear chart more nuclei show a prolate deformation than an oblate deformation. Additionally, one should note that a spectroscopic quadrupole moment can only exist for $I > 1/2$.

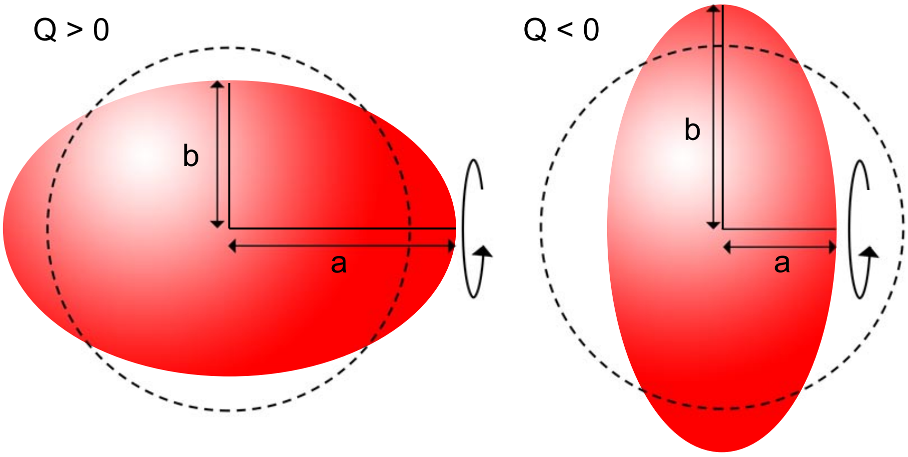

Figure 2.3.: Shapes of deformed nuclei, with a quadrupole moment larger than zero, the shape is prolate and shaped like a cigar (left) and with $Q < 0$ it is oblate and shaped like a lense (right).

2.2 Atomic theory

Nuclear properties discussed in chapter 2.1 have an impact on the electronic energy levels in the atom and the energy difference between those levels can be probed with collinear laser spectroscopy. Probing these energy levels started with the discovery of the spectral lines by Fraunhofer and increasing precision of measurement methods led to the discovery of the fine- and hyperfine-structure levels. The central coulomb field of the nucleus, which can in zeroth order be simplified as a point-like electric charge, acts on the electrons and the resulting energy levels can in-principle be calculated with the Dirac theory. These fine-structure terms are modified by the nuclear structure and this is called hyperfine structure. The effect is small compared to the energy splittings of the fine structure and only became observable with increasing resolution. This chapter will cover the underlying theory.

2.2.1 Hyperfine splitting

The coupling of the electrons total angular momentum **J** with the nuclear spin **I** gives rise to a splitting of the fine structure level. The energy shift arises from the interaction of the magnetic moment μ_{nucleus}, see Eq. (2.42), with the magnetic field

$$\mathbf{B}_e = B_0 \frac{\mathbf{J}}{\hbar}, \tag{2.47}$$

created by the electrons at the location of the nucleus. Here $\mathbf{J} = \mathbf{L} + \mathbf{S}$ is the total angular momentum of the electrons as a sum of their total spin **S** and orbital momentum **L** (assuming *LS*) coupling). Therefore the energy difference between different orientations of **J** and **I** is given by [Dem10]

$$\begin{aligned} \Delta E_{\text{HF}} &= -\boldsymbol{\mu}_{\text{nucleus}} \cdot \mathbf{B}_e \\ &= -\mu_{\text{nucleus}} \cdot B_0 \cdot \cos(\angle(\mathbf{J}, \mathbf{I})). \end{aligned} \tag{2.48}$$

The total angular momentum **F** is defined as $\mathbf{F} = \mathbf{J} + \mathbf{I}$ and its quantum number F ranges between

$$|I - J| \leq F \leq |J + I| \, . \tag{2.49}$$

Due to $\mathbf{J} \cdot \mathbf{I} = 1/2(\mathbf{F}^2 - \mathbf{J}^2 - \mathbf{I}^2)$ the cosine in (2.48) can be replaced by

$$\begin{aligned} \cos(\angle(\mathbf{J}, \mathbf{I})) &= \frac{\mathbf{J} \cdot \mathbf{I}}{|\mathbf{J}| \cdot |\mathbf{I}|} \\ &= \frac{1}{2} \frac{F(F+1) - J(J+1) - I(I+1)}{\sqrt{J(J+1) \cdot I(I+1)}}. \end{aligned} \tag{2.50}$$

$$\tag{2.51}$$

With this, the hyperfine energy (2.48) can be written as

$$\Delta E_{\text{HF}} = \frac{A}{2}[F(F+1) - J(J+1) - I(I+1)] = \frac{A}{2} C, \tag{2.52}$$

with the hyperfine structure parameter

$$A = \frac{g_I \cdot \mu_{\text{nucleus}} \cdot B_0}{J} \tag{2.53}$$

and the Casimir-factor $C = F(F+1) - J(J+1) - I(I+1)$.

This simple model assumes a point-like magnetic dipole moment and therefore the different electronic levels have a constant A-factor ratio, which is only determined by B_0 and J. In reality this is not the case, since the magnetic moment is distributed inside the nuclear volume, which is called the Bohr-Weisskopf effect. Changes either in the electronic distribution or in the magnetic distribution between isotopes can slightly alter their ratio, which is called a hyperfine-structure anomaly.

A nucleus with an electric quadrupole moment also has an influence on the hyperfine energy levels if $J > 1/2$. In this case, the electron shell can give rise to an electric field gradient $V_{zz} = \langle \partial^2 V_z / \partial x^2 \rangle$ at the nucleus and leads to an energy shift of the non-spherical density distribution according to

$$\Delta E_{\text{EQ}} = B \cdot \frac{\frac{3}{4}C(C+1) - I(I+1)J(J+1)}{2I(2I-1)J(2J-1)}, \tag{2.54}$$

with the hyperfine structure parameter

$$B = eQV_{zz}\ , \tag{2.55}$$

for the individual hyperfine levels with quantum number F. The total hyperfine splitting energy is then calculated by

$$\begin{aligned} \Delta E_{\text{HFS}} &= \Delta E_{\text{HF}} + \Delta E_{\text{EQ}} \\ &= \frac{A}{2}C + B \cdot \frac{\frac{3}{4}C(C+1) - I(I+1)J(J+1)}{2I(2I-1)J(2J-1)}\ . \end{aligned} \tag{2.56}$$

Relevant hyperfine levels and allowed transitions for the different nickel isotopes are shown in Fig. 2.4. Nuclear spins up to $I = 5/2$ and the rather large total angular momentum of the upper and lower state of $J_{\text{upper}} = 2$, $J_{\text{lower}} = 3$ allow up to 14 transitions, which are determined by the selection rules for hyperfine transitions $\Delta F = 0, \pm 1$ (with $F = 0$ to $F' = 0$ not being allowed) as well as of course the selection rules for the fine structure. Relative intensities of the single $S_{F \to F'}$ transitions within a $J \to J'$-transition can be determined using the Racah coefficients which are related to the Wigner $6j$-symbols [Dra06] denoted by {} in

$$S_{F \to F'} = (2F+1)\left(2F'+1\right) \begin{Bmatrix} F & F' & 1 \\ J' & J & 1 \end{Bmatrix}^2 S_{J \to J'}. \tag{2.57}$$

Here $S_{J \to J'}$ is the total intensity of the $J \to J'$-transition.

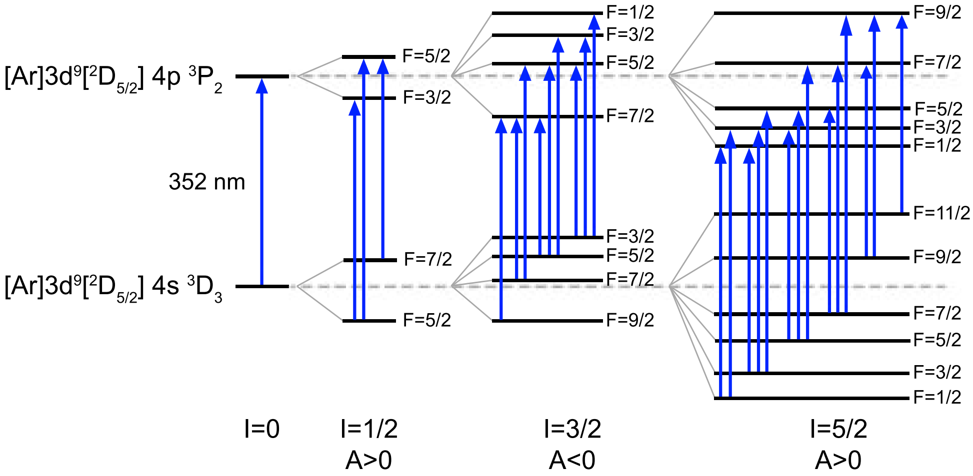

Figure 2.4.: Schematic drawing of the relevant nickel hyperfine energy levels with the allowed hyperfine transitions.

2.2.2 Isotope shift and charge radius

Transition frequencies between two energy levels of an electron in an atom are observed to change along the isotopic chain. The change $\delta\nu^{A,A'}$ of ν among two isotopes with mass numbers A and A' is called the isotope shift .

$$\delta\nu^{A,A'} = \nu^{A'} - \nu^{A}\,. \tag{2.58}$$

Changing the number of neutrons affects the mass and the charge distribution of the nucleus and the isotope shift can therefore be written as the sum of a mass shift $\delta\nu^{A,A'}_{\mathrm{MS}}$ and the field shift $\delta\nu^{A,A'}_{\mathrm{FS}}$

$$\delta\nu^{A,A'} = \delta\nu^{A,A'}_{\mathrm{MS}} + \delta\nu^{A,A'}_{\mathrm{FS}}\,. \tag{2.59}$$

2.2.2.1 Mass shift

Changing the mass of the nucleus alters the reduced mass of the electron in the electron-nucleus system. The resulting shift of the transition frequency is called the normal mass shift (NMS) and it is proportional to the reduced mass $\mu = m_e/(1+m_e/m_A)$ of the system, with the electron mass m_e and the mass of the nucleus m_A. Therefore the relative NMS among two isotopes with mass numbers A and A' is

$$\frac{\delta\nu^{A,A'}_{\mathrm{NMS}}}{\nu^{A}} = \frac{\mu'-\mu}{\mu'} \to \delta\nu^{A,A'}_{\mathrm{NMS}} = \nu^{A}\cdot\frac{\frac{m_e}{m_A}-\frac{m_e}{m_{A'}}}{1+\frac{m_e}{m_A}} \approx N\cdot\frac{m_{A'}-m_A}{m_A\cdot m_{A'}}\,, \tag{2.60}$$

with the normal mass shift constant $N = m_e\nu^{A}$ and the approximation $m_e \ll m_A, m_{A'}$.
In atoms with more than one electron their motion is correlated, due to the electrostatic inter-

action among them, which is therefore also affected by a mass change of the nucleus. This is the so called specific mass shift (SMS) and it has the same mass dependence as the NMS

$$\delta\nu_{\mathrm{SMS}}^{A,A'} = S \cdot \frac{m_{A'} - m_A}{m_A \cdot m_{A'}}. \tag{2.61}$$

The specific mass shift constant S is notoriously difficult to calculate since all electron correlations have to be taken into account. An ab-initio approach has to date only been achieved for systems with up to five electrons [Maa19].
The total mass shift is given by

$$\delta\nu_{\mathrm{MS}}^{A,A'} = \delta\nu_{\mathrm{NMS}}^{A,A'} + \delta\nu_{\mathrm{SMS}}^{A,A'} = (N+S) \cdot \frac{m_{A'} - m_A}{m_A \cdot m_{A'}} = K \cdot M. \tag{2.62}$$

With the total mass shift constant $K = (N+S)$ and $M = (m_{A'} - m_A)/(m_A \cdot m_{A'})$.

2.2.2.2 Field shift

The field shift results from the finite size of the nucleus (FNS). In a point-like nucleus the electrons would be attracted by coulomb potential that approaches $-\infty$ at the center. In reality the nucleus has a certain dimension and therefore the potential deviates from the $1/r$ behavior and has a finite value at the center of the nucleus. Therefore the binding energy for electrons with a nonvanishing probability density in the nucleus ($|\Psi(0)|^2 \neq 0$) is disturbed by [Ott89]

$$E_{\mathrm{FNS}} = \frac{Ze^2}{6\epsilon_0} \langle r_c^2 \rangle |\Psi(0)|^2, \tag{2.63}$$

with the mean-square charge radius $\langle r_c^2 \rangle$. If the electron is excited from an initial state (i) to a final state (f) the probability density $|\Psi(0)|^2$ changes accordingly:

$$(\Delta|\Psi(0)|^2)_{i\to f} = |\Psi_f(0)|^2 - |\Psi_i(0)|^2. \tag{2.64}$$

This then affects also the transition frequency by

$$\delta\nu_{\mathrm{FNS},i\to f} = \frac{Ze^2}{6h\epsilon_0} \langle r_c^2 \rangle (\Delta|\Psi(0)|^2)_{i\to f}. \tag{2.65}$$

Comparing now two isotopes with charge radii $\langle r_c^2 \rangle^A$ and $\langle r_c^2 \rangle^{A'}$ causes the field shift of

$$\delta\nu_{\mathrm{FS}}^{A,A'} = \frac{Ze^2}{6h\epsilon_0} \Delta|\Psi(0)|^2 (\langle r_c^2 \rangle^{A'} - \langle r_c^2 \rangle^{A}) \tag{2.66}$$

$$= \frac{Ze^2}{6h\epsilon_0} \Delta|\Psi(0)|^2 \delta\langle r_c^2 \rangle^{A,A'} = F\,\delta\langle r_c^2 \rangle^{A,A'}, \tag{2.67}$$

with the field-shift constant F. For better readability the transition indication $i \rightarrow f$ is not noted anymore.
In summary, Eq. (2.59), (2.62) and (2.66) yield a total isotopic shift of

$$\delta\nu^{A,A'} = \delta\nu^{A,A'}_{MS} + \delta\nu^{A,A'}_{FS} = M \cdot K + F \cdot \delta\langle r_c^2\rangle^{A,A'}. \tag{2.68}$$

2.2.2.3 Modified isotope shift

To extract the change in mean-square charge radii from the measured isotope shifts the field-shift and mass-shift constants are required. In light nuclei it is possible to obtain those theoretically with high-precision, but this is limited currently to systems with up to 5 electrons [Puc15]. Therefore it is established to use the so called *King-Plot* procedure [Kin84]. However, this is only feasible, when at least for three of the measured isotopes absolute root mean-square charge radii are known from other experimental methods, usually x-ray spectroscopy on muonic atoms and eleastic scattering. Those absolute root mean-square charge radii can then be used to calculate the change in mean-square charge radii $\delta\langle r_c^2\rangle^{A,A'}_{\text{lit}}$ to a common reference isotope with mass A. Modifying Eq. (2.68) leads to the modified isotope shift

$$\delta\nu^{A,A'}_{\text{mod}} = \underbrace{M^{-1}\delta\nu^{A,A'}}_{y} = F \cdot \underbrace{M^{-1} \cdot \delta\langle r_c^2\rangle^{A,A'}_{\text{lit}}}_{x} + K, \tag{2.69}$$

with $M^{-1} = (m_A \cdot m_{A'})/(m_{A'} - m_A)$. If the modified isotope shift is plotted as a function of the modified change in mean-square charge radii x all data points should lie on a straight line due the linear behavior of Eq. (2.69) $y = F \cdot x + K$. A linear fit to the experimental values reveals the slope which is the field shift constant F and the offset which is the mass shift constant K.
With the knowledge of F and K the change in mean-square charge radii from the measured isotope shifts can be extracted for all other isotopes by modifying Eq. (2.68) to

$$\delta\langle r_c^2\rangle^{A,A'} = \frac{\delta\nu^{A,A'} - M \cdot K}{F}. \tag{2.70}$$

2.3 Collinear laser spectroscopy

In high-resolution laser spectroscopy the interaction of a laser with the electrons in the shell of an atom or ion is used to observe the transition frequency between two energy levels by the resonant interaction with the laser beam. This can be realized by tuning the laser frequency and measuring the corresponding response of the atom/ion, for example by counting the photon scattering rate from spontaneous emission and identifying the transition frequency as the resonance center at the highest count rate. Due to the uncertainty principle

$$\Delta E \cdot \Delta t \geq \hbar, \tag{2.71}$$

the discreteness of these energy levels is softened around the central frequency ν_0 [Dem11]. With the lifetime τ_i of the level i and the energy to frequency relation $E = h \cdot \nu$, the energy can be at best determined to $\Delta E_i = \hbar/\tau_i$ and the frequency uncertainty is

$$\delta\nu = \frac{\Delta E}{\hbar} = \frac{1}{2\pi\tau_i}. \tag{2.72}$$

This is the natural linewidth and the intensity profile $I(\omega)$ detected in laser spectroscopy of atoms at rest is best described by the Lorentzian profile [Dem11]

$$I(\omega) = I_0 \frac{\gamma/2\pi}{(\omega - \omega_0)^2 + (\gamma/2)^2}, \tag{2.73}$$

with $\omega = 2\pi\nu$, the integrated intensity I_0 and the full width half maximum (FWHM) $\gamma = 1/\tau$ corresponds to the transition rate τ. Under typical experimental conditions the natural linewidth is usually overshadowed by the Doppler broadening resulting from the velocity distribution of the atoms along the laser direction caused by the thermal motion, which can be expressed under the assumption of a Maxwell-Boltzmann distribution as a Gaussian line profile

$$I(\omega) = I(\omega_0) e^{-(c(\omega-\omega_0)/(\omega_0 \upsilon_W))^2} \tag{2.74}$$

with the most probable velocity $\upsilon_W = \sqrt{2kT/m}$ along the laser and the FWHM of

$$\delta\nu_D = \frac{\nu_0}{c}\sqrt{\frac{8k_B T \ln 2}{m}}\,. \tag{2.75}$$

Hot surface ion sources typically operate at ~1000 to ~2500 K and therefore the Doppler broadening becomes 2-3 orders of magnitudes larger than a typical natural linewidth and is in the GHz region. This is a strong limitation for the resolution of laser spectroscopy and many techniques have been developed to overcome this broadening. Examples are non-linear spectroscopy techniques like saturation spectroscopy, (first order) Doppler-free techniques like 2-photon spectroscopy or reduction of the Doppler width by cooling the ions or atoms. In the investigation of short lived radioactive isotopes the duration of any cooling process always competes with the lifetime of the isotopes and therefore only short cooling processes are an option. Collinear laser spectroscopy is performed in flight on a fast moving ion beam and therefore the ions are prepared for spectroscopy by accelerating them to a beam energy of 10-60 keV before they are overlapped with the laser in a collinear geometry. Since the initial energy spread of the ions $\delta E = m \cdot \upsilon \cdot \delta\upsilon$ from the ion source stays constant during the acceleration, the velocity spread of the ions in direction of acceleration $\delta\upsilon = \delta E/(m \cdot \upsilon)$ is reduced with the increase of velocity to $\upsilon_{\mathrm{acc}} = \sqrt{2eU/m}$ to [Kau76]

$$\frac{\delta\upsilon_U}{\delta\upsilon_0} = \frac{k_B T/\sqrt{2eUm}}{\sqrt{2k_B T/m}} = \frac{1}{2}\sqrt{\frac{k_B T}{eU}}. \tag{2.76}$$

At beam energies above approximately 10 kV the Doppler broadening resulting from this energy spread is of the order of the natural line width, allowing high-precision laser spectroscopy on a very short time scale and can be applied to isotopes with lifetimes in the millisecond range. The total line profile of the transition will be given by the Lorentzian shape from the natural line width and a gaussian shape from the Doppler broadening and therefore it can be represented by the convolution of both, which is the Voigt profile [Dem11]

$$I(\omega) = \frac{\gamma I_0 N_i c}{2\pi^{3/2}\omega_0 v_w} \int_{-\infty}^{+\infty} \frac{\exp - \frac{c^2(\omega_0 - \omega')^2}{\omega_0^2 \cdot v_w^2}}{(\omega - \omega')^2 + \left(\frac{\gamma}{2}\right)^2} \mathrm{d}\left(\omega_0 - \omega'\right). \tag{2.77}$$

The FWHM of the Voigt profile is described by [Dem11]

$$\Delta\omega_V = 0,535\Delta\omega_L + \sqrt{0,2166\Delta\omega_L^2 + \Delta\omega_G^2}, \tag{2.78}$$

where $\Delta\omega_L$ is the Lorentzian FWHM and $\Delta\omega_G$ is the Gaussian FWHM.
Probing the ions in flight in a (anti-)collinear geometry causes a Doppler shift in frequency in the rest frame of the ions compared to the laser frequencies in the laboratory frame by

$$\nu_{a/c} = \nu_L \cdot \gamma(1 \pm \beta), \tag{2.79}$$

$$\text{with } \beta = \frac{v}{c} \text{and } \gamma = \frac{1}{\sqrt{1-\beta^2}}.$$

Here the "+" represents the counter propagating geometry (anti-collinear), where the ions experience a blue-shifted laser frequency while the "–" represents the laser co-propagating geometry (collinear), where the ions experience a red-shifted laser frequency. Single charged ions accelerated by an acceleration voltage U gain a velocity β of

$$\beta = \sqrt{1 - \left(\frac{mc^2}{eU + mc^2}\right)^2}. \tag{2.80}$$

From (2.79) it is obvious, that the laser frequency in the ion frame can be changed by varying the ion velocity β. Hence it is common in collinear laser spectroscopy to keep the laser at a fixed frequency in the laboratory ν_L and scan the resonance frequency by accelerating the ions with a voltage that is applied close to the detection chamber. This is called *Doppler-tuning*. Therefore the total accelerating voltage U consists of two parts, the start potential U_{acc}, with the main purpose of reducing the Doppler broadening and a small scanning voltage U_{scan} to alter the speed of the ions for Doppler-tuning, which is usually applied near the detection region while the laser can interact with the atoms/ions.

3 TrIga Laser Data Acquisition - TILDA

In this work the TrIga Laser Data Acquisition (TILDA) system was developed based on the experience gained from a small-scale prototype developed in a previous diploma thesis [Kau13]. TILDA is designed for a variety of CLS experiments and its main feature is the time-resolving photon detection which allows to count the incoming events in correlation to a common time stamp. This is very useful when working with pulsed ion beams, where it is crucial to count the events from the Photomultiplier-Tubes (PMTs) only during the time the ions pass through the detection region, as it is shown in Fig. 3.1. The scheme presents the general setup for this kind of experiment: A continuous ion beam is accumulated and cooled in a Radio Frequency Cooler and Buncher (RFQCB) device. Then a short bunch bunch is ejected by pulling down the trapping potential at the RFQCB exit. The ion bunch travels to the optical detection region. Using an electrostatic deflector, it is superimposed with the laser beam and co-propagating with the beam into the optical detection region. Photons scattered by the ions inside the detection region are detected with the PMTs and each event is recorded in time to the extraction pulse of the RFQCB. This allows to select only events that happened within this time window and neglect all other events as they are evoked by either laser stray light or the dark count rate from the PMT and do not contribute to the signal. The scanning procedure is then realized by changing the voltage, which is applied to the optical detection region in between the bunches (*Doppler-tuning* see ch. 2.3). Therefore a Digital-to-Analog Converter (DAC) produces an output of ±10 V with a slew rate of some μs/V and at a precision of 18-bits, which is then amplified by an linear bipolar amplifier (Kepco), to ±500 V in order to expand the scanning range. Isotope shifts are often larger than this dynamic scanning range, hence a static offset of up to ±10 kV can be added and adjusted for each isotope.

TILDA's core functionality is separated into two modules. One is responsible for the acquisition itself, setting the scanning-voltage and reading the photon signals. The other module is in charge of controlling the remaining time relevant parts in the experiment by sending 5 V-Transistor-Transistor Logic (TTL) pulses to them. TILDA's hardware and software will be explained in detail in the following chapters.

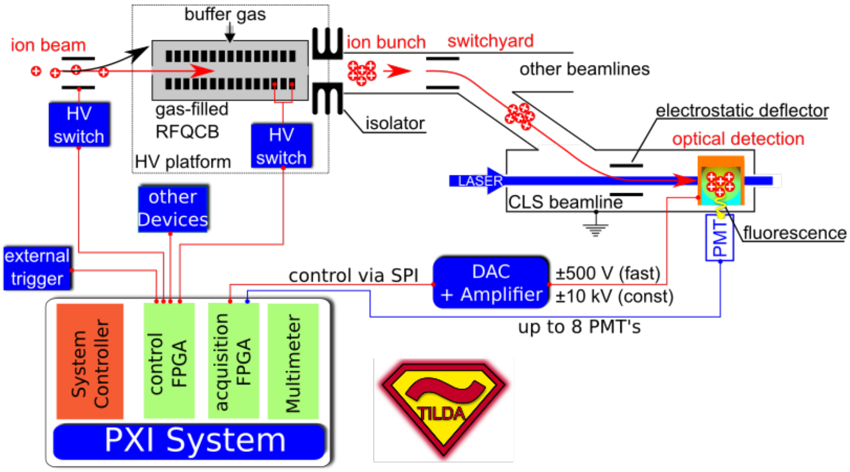

Figure 3.1.: Measurement principle of a CLS setup with a pulsed beam structure.

3.1 Hardware

Commercial hardware solutions were used in TILDA wherever possible to minimize the hardware development, allowing efficient development and maintenance of the data acquisition system. Core of TILDA is a PC in a PCI eXtensions for Instrumentations (PXI)-chassis which can be filled with individual PXI modules according to the experimental conditions enabling a high degree of flexibility for the users.
The individual parts of TILDA's hardware are described in the following chapters.

3.1.1 PXI chassis and controller

PXI is a framework initiated by the company National Instruments and today the PXI-alliance is joined by a wide range of companies. Based on the well established PCI-Bus a variety of PXI-modules is available. Basis of TILDA is a PXI-chassis with 9 slots (NI PXIe-1078) and an integrated controller (NI PXIe-8840), which is operated as a standard PC while real time operation is realized in the modules. A second instance of TILDA at GSI Helmholtzzentrum für Schwerionenforschung (GSI) was also successfully installed with only a *Thunderbolt* interface card as a controller inside the PXI-crate connected to a Thunderbolt PCI-card inside a host PC acting as a controller for TILDA. Communication between the controller and the modules or the modules among each other can be realized via the backplane of the chassis. Modules can be synchronized via a phase-locked loop to a common 10MHz reference which is available on the backplane.

3.1.2 Field programmable gate array - FPGA

TILDA's time-resolved data acquisition requires computations in real time which is realized by a Field Programmable Gate Array (FPGA). Core of any FPGA is an array of interchangeable logic blocks with connections linking the blocks that can be programmatically altered allowing the user to change this hardware to the desired needs. The FPGAs are programmed using a hardware description language (HDL) which is compiled to a bitfile and loaded to the FPGA. The basic layout of TILDA includes two Virtex-5 FPGAs which are based on a PXI module from National Instruments (NI, PXI-7852R). This has the advantage, that the user does not need to program the FPGA in a HDL, but can use the graphical high level programming language LabVIEW, which will be explained in detail in chapter 3.2.5. Thereby the user can quickly adapt the hardware to the needs of the experiment.
On the hardware side this module includes a lot of useful features, like a 40 MHz clock on board to ensure the real timing, further it has 96 digital in-/outputs (DI/DO), 8 Analog Inputs (AIs), 8 Analog Outputs (AOs) and a Direct Memory Access Controller (DMAC) to exchange data stored in the FPGA's memory with the host PC. With the DMAC large chunks of data can be transferred loss-less, quick and asynchronous from the FPGA to the PC to ensure not to disturb the real time operations on the FPGA. This will be explained in detail in chapter 3.2.2.

3.1.3 TTL-Linedriver

The FPGAs are connected to a TTL-Linedriver module designed at the GSI and shown in Fig. 3.2 which transfers the 3.3 V digital outputs from the FPGA to 5 V with a current of up to 100 mA matching TTL driving a 50 Ω input resistance. Each of the individual TTL-Linedriver modules consists of one backplane circuit board which transfers the National Instruments connector to a standard circuit board connector. This is connected to a frontplate circuit board housing 8 channels and distributing another 32 Channels which are divided into four smaller frontplate circuit boards with 8 channels each, resulting in a total of 40 channels for each TTL-Linedriver module. Each channel is equipped with Lemo connectors on the front plate allowing a quick change of connections and can be configured as output or input by a jumper on each circuit board. LED lights on the front plate indicate if a channel is active. Every channel has an 80 ns latency, but since this is equal for all channels it does not influence relative timings. Currently TILDA uses two TTL-Linedriver modules, one for each FPGA, one for the pulse pattern generator and one for the data acquisition. The pulse-pattern-module uses 8 of the channels as a trigger, the remaining 32 channels are configured as an output and can be used to control time critical devices in the experiment. The data-acquisition-module has 8 trigger inputs, 8 inputs for the TTL-signals from the PMTs, 16 outputs for controlling devices and debugging and 8 channels are used for the control of the DAC which is described in detail in chapter 3.1.4. Assignment of the individual channels can be found in the documentation in the lab log.

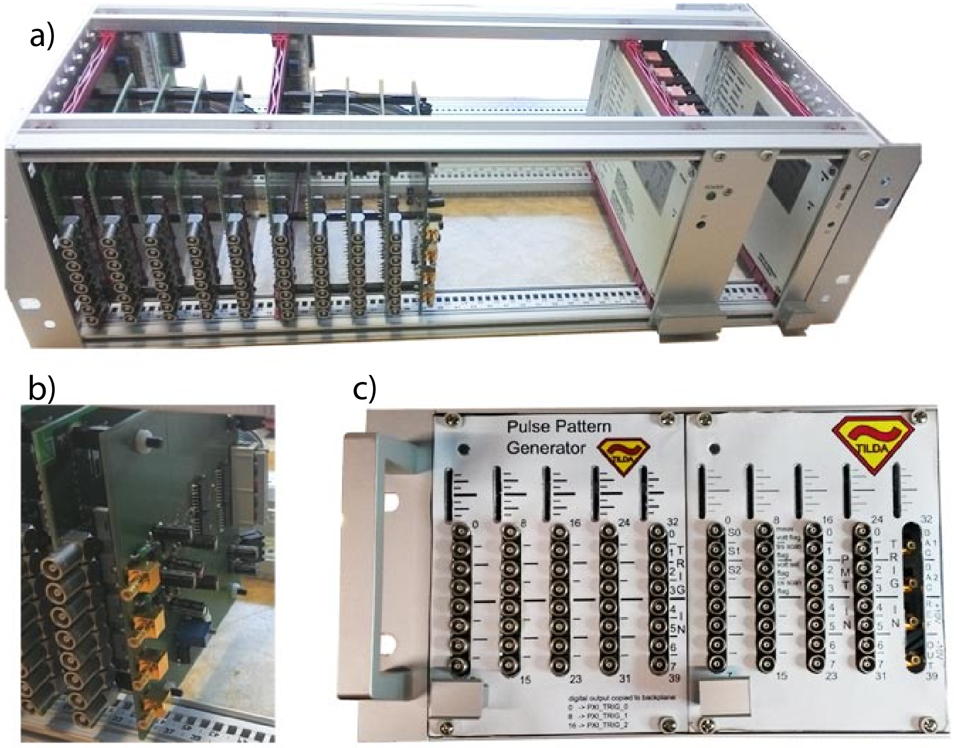

Figure 3.2.: a) Photo of the TTL-Linedriver chassis without cover. b) close-up of the DAC circuit board with its golden SMB connectors in the front, stacked on top of the other TTL-Linedriver circuit boards. c) front view of the TTL-Linedriver with the frontplate installed.

3.1.4 Digital to analog converter

In most CLS experiments the laser frequency in the ions rest frame is variied by changing the acceleration voltage at the detection region (*Doppler-tuning*, see ch. 2.3). Therefore the frequency in the ion rest frame is directly related to the applied voltage and accurate knowledge of it is the key for high-precision experiments. It requires high specifications for the DAC being used in the experiment as the starting point of the voltage chain. The main criterium is linearity: The integrated non-linearity must not exceed 50 μV in order to achieve a voltage setting with a precision of $5 \cdot 10^{-6}$ on a 20 V scale. Additionally the voltage needs to be set within 100 μs in order to enable a fast scanning procedure.

We have tested two DACs. Results of the linearity tests are shown in Fig. 3.3. The output voltage is plotted as a function of the DAC register bit. The lower plots show the residuals to the linear fit. The native 16-bit analog outputs of the PXI-7852R modules (left) exhibit an unwanted non-linearity of about -0.9 mV to 0.5 mV over the full ±10 V range. This is still within its specifications given as an Integrated Non Linearity (INL) of at maximum four Least Significant Bits (LSBs), corresponding to a deviation of $4 \cdot 0.305\,\text{mV} = 1.22\,\text{mV}$ from linearity, but it is outside of the requirements of the demands for CLS experiments. In order to meet our requirements at a low cost, a custom made circuit board (CB) with a high precision 18-bit DAC (Analog Devices, AD5781) was developed. The first design of this DAC was based on an evaluation board situated in a custom built housing including power supplies and connectors. Control of the DAC chip is realized via the Serial Peripheral Interface (SPI) bus which is generated by the FPGA. The SPI bus uses four digital outputs from the FPGA, along with three DAC-control lines this makes a total of 7 digital outputs which are optically decoupled and then connected to the DAC. The optical decoupling has the advantage, that the grounding of the DAC can be decoupled from the computer and is rather provided on the output side of the DAC. This setup was very satisfying and the linearity was more than an order of magnitude better than the analog output of the FPGA, see Fig. 3.3 b. The non-linearity of the output ranges between -6 μV to 17 μV over the full range and lies well within a quarter of the LSB for this 18-bit DAC ($0.25 \cdot 0.076\,\text{mV} = 19\,\mu\text{V}$) and well below the required linearity for CLS experiments.

As the evaluation setup was successful the board was redesigned in collaboration with the electronics workshop of the nuclear chemistry institute in Mainz in order to fit inside the TTL-Linedriver chassis and replace one of the frontplate circuit boards. This required an additional power supply within the TTL-Linedriver chassis in order to realize the optical decoupling of the DAC from the FPGA and for the additionally required voltages on the DAC circuit board. The needed digital outputs for the SPI bus and the DAC-control lines are provided by the same cable that controlled the TTL-Linedriver circuit board before. This cable supports 8 digital outputs which is one more than needed by the DAC, therefore another AD-5781 DAC chip was integrated into the DAC circuit board by using this additional digital output as a control switch for the second DAC granting the user to generate another high precision voltage and making efficient use of the 8 channels. Control of the two DACs can only happen sequentially since both use the same SPI bus channels, but only different control switches. Setting the DAC bits requires 15 μs and reading them back costs another 15 μs, so each voltage step can be applied within 30 μs. A picture of this board can be found in Fig. 3.2 b. DAC Outputs are chosen to be SMB-connectors in order not to confuse them with the Lemo-connectors of TTL outputs, see Fig. 3.2 c. By now, five DAC-boards have been produced and calibrated. All calibration results show similar behavior and have quite constant offsets and slopes (details can be found in the TRIGA-LASER lab log). Three of the produced DAC-boards are in permanent use at the ALIVE/KOALA, COLLAPS and TRIGA-LASER experiments and until now they did not show any malfunction or unexpected behavior. The circuit board designs and the parts list of the boards can also be found in the lab log, enabling future users to quickly rebuild such a board.

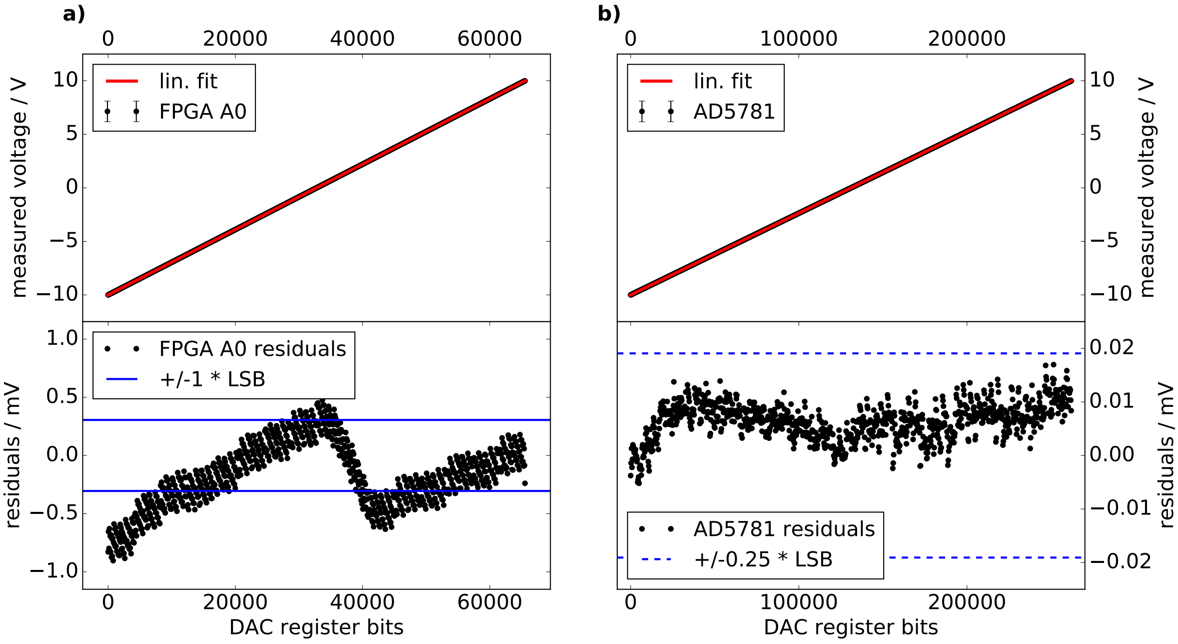

Figure 3.3.: Comparison of a typical DAC output voltage measurement between the different DACs over the full ±10 V range with 1001 steps each. In the upper plots the measured voltage is plotted against the set DAC register bit and a straight line is fitted to the data points. In the lower plots the residuals between the data points and the linear fit are shown without error bars, note the different voltage scales. Both DAC voltages are measured with the same digital multimeter (Agilent A34401A) and have similar uncertainties of approximately 150 μV. a) 16-bit analog output of the NI-7852R FPGA module b) 18-bit AD5781-DAC.

3.1.5 High-voltage switch box

In scanning operation, the DAC provides a range of ±10 V which can be amplified to ±500 V or even ±1000 V before applying it as Doppler-tuning voltage to the post acceleration region. Higher amplifications have shown to be challenging since they also amplify any noise in the fundamental signal and therefore the scanning range is expanded by a high-voltage power supply of ±10 kV that provides a constant voltage output during the scan. The high-voltage power supplies in use at the experiments usually need some minutes to stabilize their output voltage [Krä10]. Hence, they cannot be integrated in the fast scanning process. To add the offset onto the scanning voltage the ground of the high-voltage supply is floated by the scanning voltage. To reduce the waiting time between different offset voltages for different isotopes, multiple high-voltage power supplies can be used and pre-set to a desired voltage well in advance of the scan. Now switching the outputs connected to the acceleration region is fast and allows quick changes of stable voltage offsets required to move the Doppler-tuning range to the region of the individual isotopes. For this purpose a High-voltage Switch Box (HSB) was built at the electronics workshop of the nuclear chemistry institute in Mainz, that is able to switch between three power supplies. Switching between the outputs is controlled by three 5V-inputs (S0-S2), which are controlled from TILDA's data acquisition FPGA. The HSB is also able to feed the amplified DAC voltages directly through and it has a *monitor* output, which is internally connected to the *electrode* output allowing a voltage measurement in parallel to the scan, see Fig. 3.4.

The blue prints of the circuit board layout and technical information on the implemented relays can be found in the lab log.

Figure 3.4.: Photo of the high-voltage switchbox developed for TILDA. a) backside with control inputs S0-S2, interlocks and control LEDs. b) side view of the box without cover. c) Front view of the box with the SHV connectors.

3.2 Software

The development of the data acquisition software was a key element of this work. One of the requirements was a well-documented and readable code to allow future users and developers to continuously upgrade and expand TILDA's capabilities. For this reason, high-level programming languages were chosen from the beginning. The main part of TILDA is written in python, which provides high readability and supplies a good and short programming style. Already during the selection of hardware this paradigm was kept in mind, so that the choice for the FPGAs was made in favor of a National Instruments product, in order to be able to program them in LabVIEW and not in a HDL. This builds the basis for a readable code and is complemented by a solid, thought-out architecture guiding new users and developers through the code of TILDA.
TILDA's software will be explained in detail in the following chapters.

3.2.1 Layout

TILDA's software is structured in a classical layer architecture as depicted in Fig. 3.5. A layer architecture abstracts the functionality of each layer to the ones above encapsulating the functionality by crossing higher and higher in the layers whereby the functionality in the lower layers becomes replaceable. Therefore a layer structure usually expands in the number of used modules from top to bottom. Maintaining the control flow from top to bottom keeps the developer from programming any unwanted loops. Functionality and modules are easy to be identified and implemented in such a layout since the scheme serves as a map.
In order to describe TILDA's layout it is best describing it from the bottom to the top layer, opposite to the direction of the control flow. The lowest layer is the hardware layer which is actually not shown, but only represented by the used interfaces, which range from LabVIEW controls over DMACQueues to file formats as xml or hdf5 and will be described in detail in chapter 3.2.2. In the driver layer the actual programming of TILDA starts. It provides the required functions

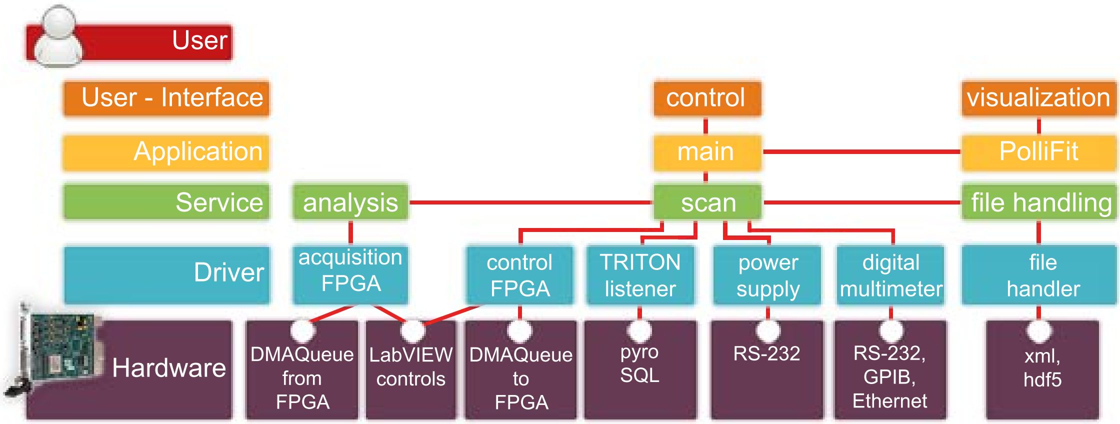

Figure 3.5.: Schematic view of the used layer architecture with the name of the layers on the left and the individual modules filling the layers to their right. Interaction between the modules is depicted with the red lines. The hardware layer is represented by the corresponding interfaces as white circles. The control flow is designed to be directed from top to bottom layer.

to access the individual hardware modules from python. The interface functions can be used by higher classes without knowledge of the actual hardware which can then be easily replaced on a change of hardware as long as the functionality of the device stays similar. The driver layer is filled with six modules, each having a designated task. Two modules are controlling the FPGAs one for the Data Acquisition FPGA (DAF) and one for the control FPGA (COF). Since both use the same type of hardware they are very similar in the interface (see section 3.2.5), but they differ a lot in their functionality: One operates as the main data acquisition hardware and the other one handles the fast parts of the experiment by its output pulse pattern. Slow controls are handled by the TRIga pyThon cONtrol (TRITON) system, developed and discussed in [Gor17]. A connection to TRITON is realized by the TRITON-listener module which is responsible for the connection to devices integrated into and controlled by the TRITON framework. It allows to read a value from any of those devices at any time of each measurement in TILDA, but control of these devices is left with TRITON. It is used for devices with constant settings during the scan. Outsourcing those devices to TRITON leads to an enhanced flexibility since a lot of devices are already controlled in this way and can be operated independent from TILDA. Devices that need to be changed during a scan like power supplies and digital multimeters are controlled directly by TILDA.

The file-handler-module is responsible for writing the data to the desired folder on the hard drive. The layer on top of the driver layer is the service layer which is responsible for controlling the whole scan, analyzing the data and handling the storage of the data. The scan-module is the core of the service layer and it combines the control of all low-level modules required for the scanning procedure. The application layer above accommodates the main-module which is the core module of the whole architecture. All commands from the user are processed here and in a regular interval it polls updates, information, data and scan progress from the lower layers. The state of the main-module and all other information from the lower layers are presented to the user in a graphical user interface, which is situated in the User-Interface layer on top, see chapter 3.2.4. The PolliFit-module in the application layer provides the utilities for data analysis and presentation.

3.2.2 Interfaces and data flow

Interfaces used in TILDA have a freely available python implementation, so no individual development in the interfaces was necessary. The RS-232, GPIB and Ethernet interfaces are covered by the *pyVisa* package which is a python implementation of the Virtual Instrument Software Architecture (VISA). The link to TRITON is realized by connection to the devices via the *pyro*4 package and the addresses of the devices are retrieved from the TRITON database using the *mysql-connector* package. Communication with the FPGAs is realized by loading and accessing a dynamic link library (DLL) from within python. This DLL was created from a C programming file offered from National Instruments and is universal for all FPGA communications. It enables to handle the programming similar to the use with LabVIEW, so LabVIEW Controls/Indicators on the FPGA can directly be accessed from the host and is used for numbers and booleans, but when it comes to larger sets of data, the Direct Memory Access Controller (DMAC) is used. This can transfer large blocks of 32-bit-elements between the memory of the FPGA-board and the memory of the host computer without losses and independent from other processes on each of them making it an asynchronous data transfer. This transfer can be realized in both directions. For the control FPGA it is mainly used to transfer the list of pulse pattern commands to the FPGA and on the Data Acquisition FPGA the transfer of the acquired data and scan information to the host PC is realized with it. Each 32-bit-element that is generated for the Data Acquisition FPGA data stream consists of a 8-bit-header, a 1-bit-header-index and a 23-bit-payload, as shown in Fig. 3.6. The 8-bit-header and the 1-bit-header-index reveals the module of the FPGA which created this 32-bit-element, the currently used modules are listed in Fig. 3.6. The 1-bit-header being zero identifies that an element is coming from the time-resolved acquisition, which means that one or more PMTs produced a count at a given time, so the PMTs which had a count get a 1 in the header, with bit-24 being PMT0 and bit-31 being PMT7 and the timestamp of the event, in 10 ns units is written to the 23-bit-paylod. If the 1-bit-header is 1, the 8-bit-header is interpreted as a key to the generating module and the payload is analyzed by the corresponding interpreter on the host computer. More on this can be found in chapter 3.2.3. TILDA's data, scan information and error codes can be transferred with this encoding in a very efficient way via a single DMAC-Channel. Writing of a 32-bit-element can happen within 10 ns meaning one clock cycle of the FGPA's 100 MHz main clock. Details of the error- and info-codes can be found in the lab log.

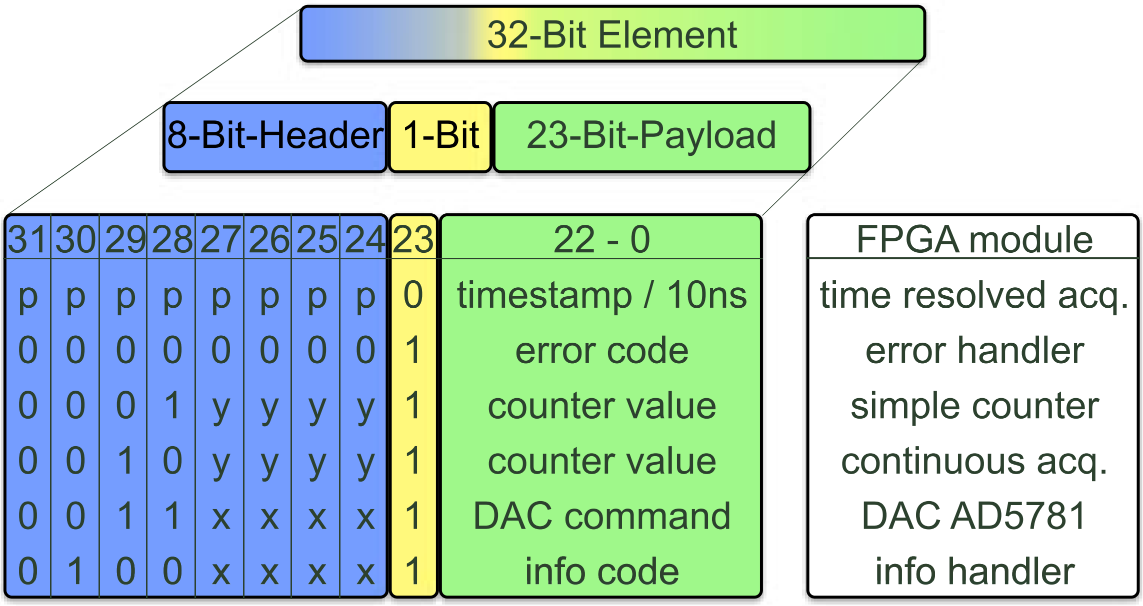

31	30	29	28	27	26	25	24	23	22 - 0	FPGA module
p	p	p	p	p	p	p	p	0	timestamp / 10ns	time resolved acq.
0	0	0	0	0	0	0	0	1	error code	error handler
0	0	0	1	y	y	y	y	1	counter value	simple counter
0	0	1	0	y	y	y	y	1	counter value	continuous acq.
0	0	1	1	x	x	x	x	1	DAC command	DAC AD5781
0	1	0	0	x	x	x	x	1	info code	info handler

p = 0/1 if PMT0-7 was active at timestamp (multiple PMT possible)
yyyy = 0-1111 for counter value of PMT0-15 (only one PMT possible)
x = 0/1 does not matter

Figure 3.6.: Encoding of the 32-bit-elements in the datastream of TILDA, each consisting of three parts, 8-bit-header, 1-bit-header-index and a 23-bit-payload. Currently used FPGA modules are listed with their desired headers, details see text.

3.2.3 Online analysis of the raw data

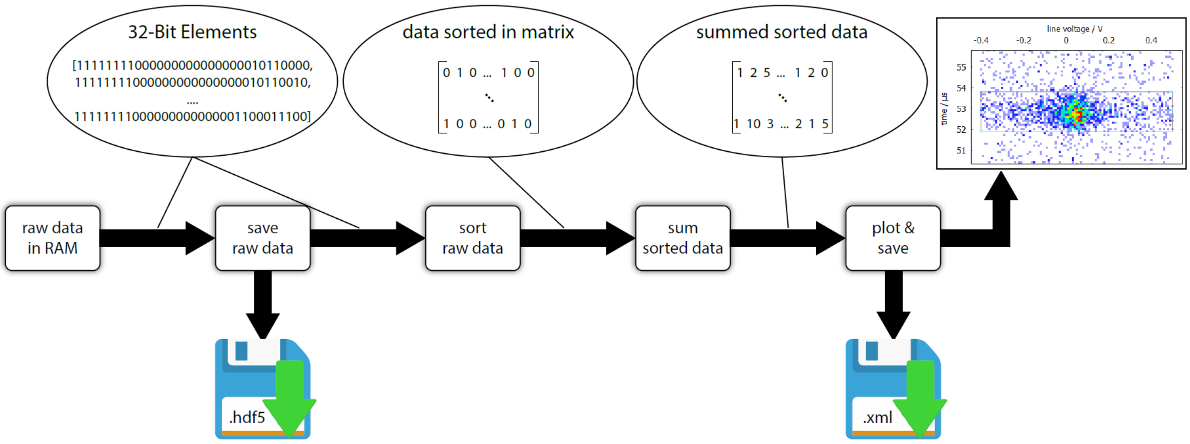

Figure 3.7.: Pipeline analysis stream from the time-resolved raw data to the full time-resolved picture, details see text.

As explained in chapter 3.2.2, the raw data generated on the FPGA consists of elements encoded in 32-bits and is transferred in huge chunks from the memory storage on the Ni-7852R board to the memory of the host controller via the PXI/PCI-bus through the direct memory access controller. This chapter will now explain TILDA's pipeline system and how the raw data stream is analyzed online into a time-resolved matrix, which can be plotted and stored on the hard drive.

Fig. 3.7 shows a schematic of the full analysis *pipeline* used for a time-resolved measurement, starting with the raw data already loaded into the memory of the host controller. The pipeline consists of several functional nodes which process the data and then pass it on to the next node. Nodes can be purely functional and only process the data as it is passed through. They can also have a storage mechanism allowing them to sum up incoming events to previously acquired ones. Also they can have a saving mechanism, which is called in the end of each track or in the case of the raw data storage node after a given time during the scan progress. In the depicted case in Fig. 3.7, the *save-raw-data* node is in charge of saving the raw data elements at the end of the scan or every 5 minutes, therefore it stores all incoming data in a listed form in memory first, before it stores them on the disk using a *hdf5* file. In parallel to storing the incoming raw data it also passes the incoming raw data to the following *sort-raw-data* node without further editing. Here the incoming raw data is sorted by their time stamp, PMT number and step number into matrices with a 10 ns resolution. These matrices are part of a TILDA/PolliFit internal datatype called *specdata* and this specdata is passed to the following *sum sorted data* node, which holds the already acquired data and adds the incoming events to them. The summed-up data is then sent from the *plot & save* node via a *qt signal* to a graphical user interface which displays the data and is explained in detail in chapter 3.2.4. In the end of the track the data is stored to an xml-file from the very same node.

While the shown pipeline is pretty much straight forward the structure would also allow a branching of the analysis stream in order to work with copies of data in different ways and to aim for different analysis patterns at the same time. Nodes are generally written in a way, that they can be reused in different analysis streams, for example loading of raw data from a previously created hdf5-file can be easily done by using most of the pipeline following the *save-raw-data* node and if the data should e.g. be filtered, a designated node can be added into the analysis flow. This keeps the analysis of the raw data clear and flexible at the same time.

3.2.4 Graphical user interface

TILDA's graphical user interface is built with the *PyQt5* package matched by the *pyqtgraph* package for live data plotting. TILDA's main window has the purpose to give the user a quick overview of what is currently happening and from here the sub windows can be opened. It is shown in Fig. 3.8 in the version 1.22. In the main window one can find and change the current working directory and the sqlite database path which is stored within the current working directory. The present state of the main TILDA loop is displayed in the next row, indicating the current task handled by TILDA. Below this, the status of the FPGA and of the sequencer can be found which are mainly foreseen for debugging reasons and are less important in standard operation. The digital multimeter status shows the user at a glance the digital multimeters currently controlled by TILDA along with their status and last reading. In most CLS experiments set values of the laser frequency and the acceleration voltage are static values for a complete measurement campaign and can be entered here by hand. Those set values will be written to the file in case these are not measured by a designated device before or after the scans. The last line in the main window lists TRITON devices to which TILDA is currently subscribed. In the upper toolbar the user can open sub windows for example to reload a file or to access one of the several tools that are available in TILDA which will be explained with their GUIs in chapter 3.3. Also the analysis module *PolliFit* can be opened from here which allows a full online analysis of the measured data and will be explained in detail in chapter 3.3.6.

Live data plotting is handled by the *pyqtgraph* package and a typical spectrum is shown in Fig. 3.9. The time-resolved plot a) presents the number of counts observed from a PMT color coded as a function of the Doppler-tuning voltage (x-axis) and the time of observation since the release trigger from the cooler and buncher (y-axis). The color coding shows at a glance where the resonance is located (1) and to the left and right of it (2) one can also see an enhanced count rate resulting from the ion/atom beam. This is caused by spontaneous emission from the atom/ion leaving an excited state which was populated either in a non-resonant way, by collisions with the residual gas in the chamber or in the charge exchange cell located before the optical detection region. This will be discussed in chapter 4.2.3. Thereby beam related background is easily observed and can reveal problems like inappropriate vacuum conditions, which would increase the non-resonant count rate. The time structure of the bunches is plotted to the right in Fig. 3.9b. It is the projection of all observed counts onto the time axis and will reveal problems like an overfilling of the buncher as discussed in detail in chapter 5.1.2. The pulse profile is particularly helpful in setting the time window in which a PMT event is considered for the resonance signal. Finally, the lower trace (Fig. 3.9c) shows the projection of the events within the timing window onto the Doppler-tuning axis from which the shape and position of the resonance is observed.

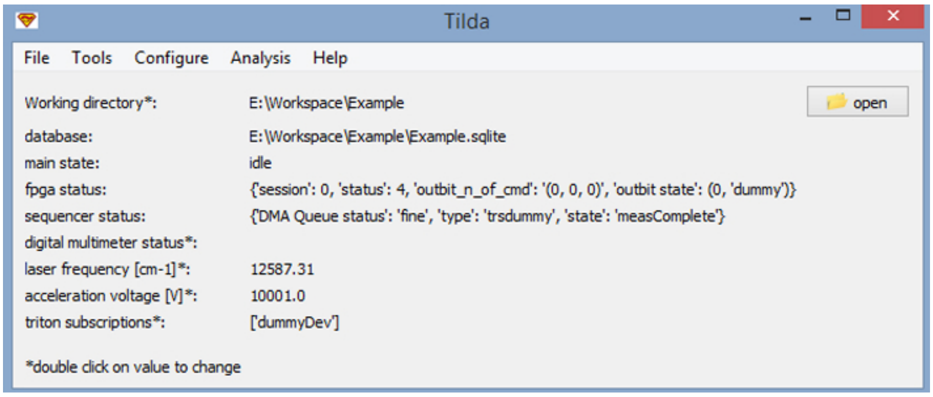

Working directory*: E:\Workspace\Example
database: E:\Workspace\Example\Example.sqlite
main state: idle
fpga status: {'session': 0, 'status': 4, 'outbit_n_of_cmd': '(0, 0, 0)', 'outbit state': (0, 'dummy')}
sequencer status: {'DMA Queue status': 'fine', 'type': 'trsdummy', 'state': 'measComplete'}
digital multimeter status*:
laser frequency [cm-1]*: 12587.31
acceleration voltage [V]*: 10001.0
triton subscriptions*: ['dummyDev']

*double click on value to change

Figure 3.8.: TILDA's Main window, showing an overview of the status of TILDA and the involved devices. Sub windows are opened from here.

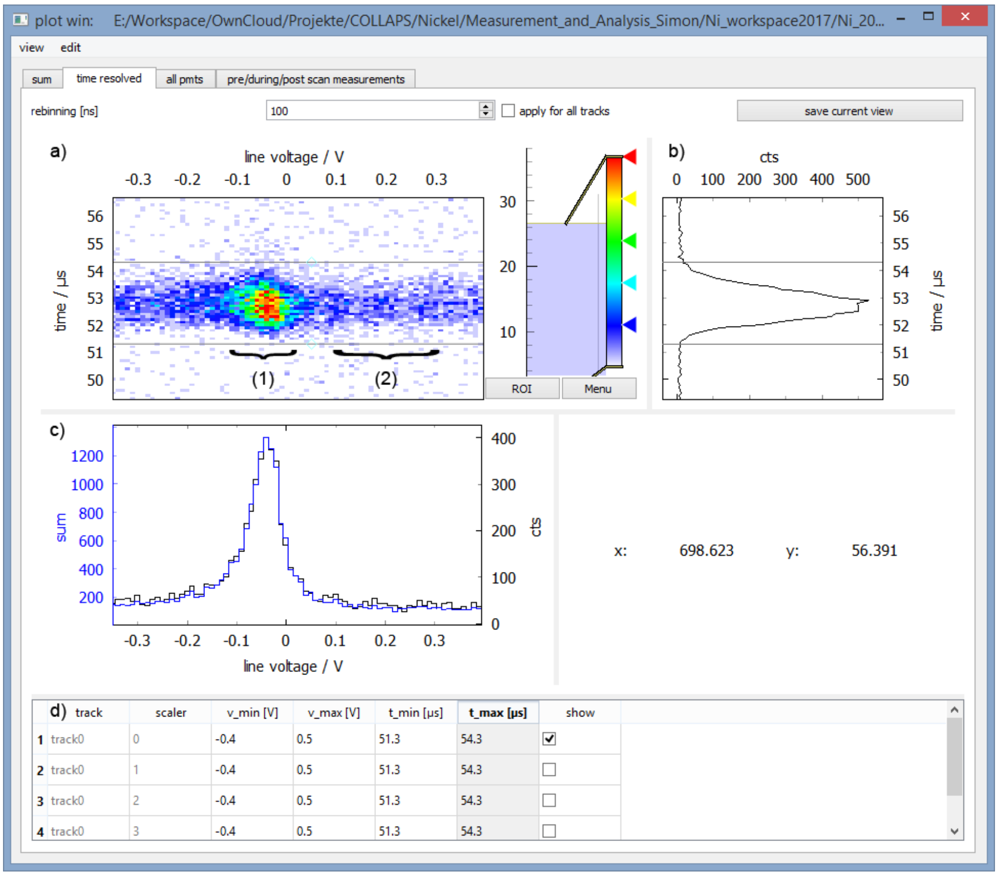

plot win: E:/Workspace/OwnCloud/Projekte/COLLAPS/Nickel/Measurement_and_Analysis_Simon/Ni_workspace2017/Ni_20...

rebinning [ns] 100

x: 698.623 y: 56.391

d)

	track	scaler	v_min [V]	v_max [V]	t_min [µs]	t_max [µs]	show
1	track0	0	-0.4	0.5	51.3	54.3	☑
2	track0	1	-0.4	0.5	51.3	54.3	☐
3	track0	2	-0.4	0.5	51.3	54.3	☐
4	track0	3	-0.4	0.5	51.3	54.3	☐

Figure 3.9.: Live data plot of TILDA. a) Typical time-resolved spectra of ^{60}Ni with the color-coded count rate within a 100 ns × 10 mV segment. The x-axis represents the DAC-voltage for Doppler-tuning and the y-axis is the time-of-flight (TOF) in μs. The grey lines represent the software gates. b) Projection of the registered events onto the time axis. The horizontal-axis is the number of integrated counts, the vertical-axis is the TOF. c) Projection of the registered events within the time window onto the voltage axis. The x-axis is the DAC-output, y-axis is the integrated number of events within the time-gate. d) Table with the software gate parameters and the currently shown PMT.

3.2.5 FPGA programming

TILDA's FPGAs are hosted in a National Instruments (NI) board and are programmed using LabVIEW. The LabVIEW code is translated by the NI-compiler to a Hardware Description Language (HDL) and then compiled to a bitfile which can be loaded to the FPGA. This bitfile can now be either controlled directly from within LabVIEW or by accessing analog functions within a dynamic link library from either a C-script or, as it was chosen here, from within a python script. The required references to the LabVIEW-indicators/-controls, as they are translated in the produced HDL-file can be obtained by creating a C-File with a so-called *C-API generator* provided by National Instruments.

Programming an FPGA holds some specialties that need to be kept in mind. All executions run in real time and LabVIEW-*while-loops* next to each other are executed parallel at the same time, as long as they are not depending on each other. LabVIEW supports the developer by weakening the real timings, because in a normal *while loop* it might split up the calculation the developer intended for one iteration of the loop by adding more steps in between in the background and therefore a *while loop* might take more than one clock cycle to execute. Developers nevertheless have the option to use single-clock-timed-loops (SCTL) that will always execute the included code within one clock cycle and LabVIEW will not compile if this cannot be realized due to too complex operations demanded by the developer for one clock cycle in the SCTL. More detailed guidelines for the programming of FPGAs in LabVIEW can be found in a manual created by National Instruments [Ins14].

Programming of the pulse-pattern FPGA was adapted from a pulse-pattern-generator code designed for an FPGA developed at the GSI, wich is described in detail in [Zie12]. Main changes were the adaption of the base frequency of the Pulse Pattern Generator (PPG) to 100 MHz in order to match the frequency on the Data Acquisition FPGA and copying the digital outputs 0, 8, 16 to the PXI-Triggerlines 0, 1, 2 on the backplane of the chassis in order to enable easy communication among the pulse-pattern FPGA and the Data Acquisition FPGA.

In the programming of the DAF, parallel execution on the FPGA was widely used. Functionalities are grouped into modules and communication between these modules is realized by first-in-first-outs (FIFO) and global variables. Controls from the host are continuously read out by a designated *while loop* and then transferred to the individual modules via global variables. The core module is responsible for coordinating the whole scanning procedure and it controls most of the other modules in the process. One module is foreseen to control which voltage should be applied from the high-voltage switch box (ch. 3.1.5), another module is responsible to trigger the digital multimeters and processing their TTL feedback signals for a complete measurement if this is available. The AD5781 module is responsible for setting the required DAC-bits at the AD5781-DAC via the SPI protocol which is generated within this module. The Outbit-module sets the TTL-Outbits according to the user requirements along as the scan proceeds and listens to the global variables of track number, scan number and step number. The most important module is of course the acquisition module which can be either time-resolved or continuous, depending on which measurement is used. This module reads the signals coming from the PMTs and either counts them for each PMT over a designated time in continuous mode or assigns them with the current time stamp in the time-resolved mode before writing them to the DMAC-channel.

3.2.6 Data storage format

TILDA's data storage format is the Extensible Markup Language (XML) which was chosen, because it is a human readable text based format. The good readability and the different layers of the XML structure become visible in the sample TILDA-XML-File shown in Fig. 3.10. Each File has a header which includes general information for the whole file such as the start time of the measurement or the isotope name. The header is followed by the *tracks*-layer which holds all measured tracks. A so called *track* is a section of the whole spectrum, usually around a resonance signal, therefore a spectrum with only one resonance line usually consists only of one track, while spectra with hyperfine splittings usually consist of as many tracks as there are widely separated resonances. For each track the DAC-voltage is applied in a range around a resonance signal or a group of signals and the whole file then holds the complete spectrum as a collection of these tracks and no measurement time is wasted on scanning the background between the peaks. Each track in the file consists of three layers: header, data and projections. The *track*-header holds the scan parameters used for this track and an excerpt of the parameters can be seen in Fig. 3.10c. The *track*-data holds all acquired data for this track accompanied by an explanation string of the data, in Fig. 3.10d this is shown for a time-resolved measurement. Note that the time-resolved data is always stored in the highest resolution of 10 ns, independent on the users choice of rebinning the time axis in the online display. In *track-projections* the projection of the time-resolved data on the voltage axis is saved with the software gates applied as they were set in the online display.

Besides the fully analyzed data also the raw data is saved during the scanning process as it comes from the FPGA's data stream, see chapter 3.2.2. Raw data is saved either when 10000 Elements where received from the FPGA or after 5 minutes since the last save, so during online operation a maximum of 5 minutes of acquisition can be lost if a malfunction occurs. Raw data is simply stored as a list and the file format is hdf5, which is not human readable, but very fast in accessing and low in storage place. Saving the raw data also has the advantage, that in post measurement analysis, the raw data can be analyzed again with a different analysis pattern, for example only considering every first bunch of each step.

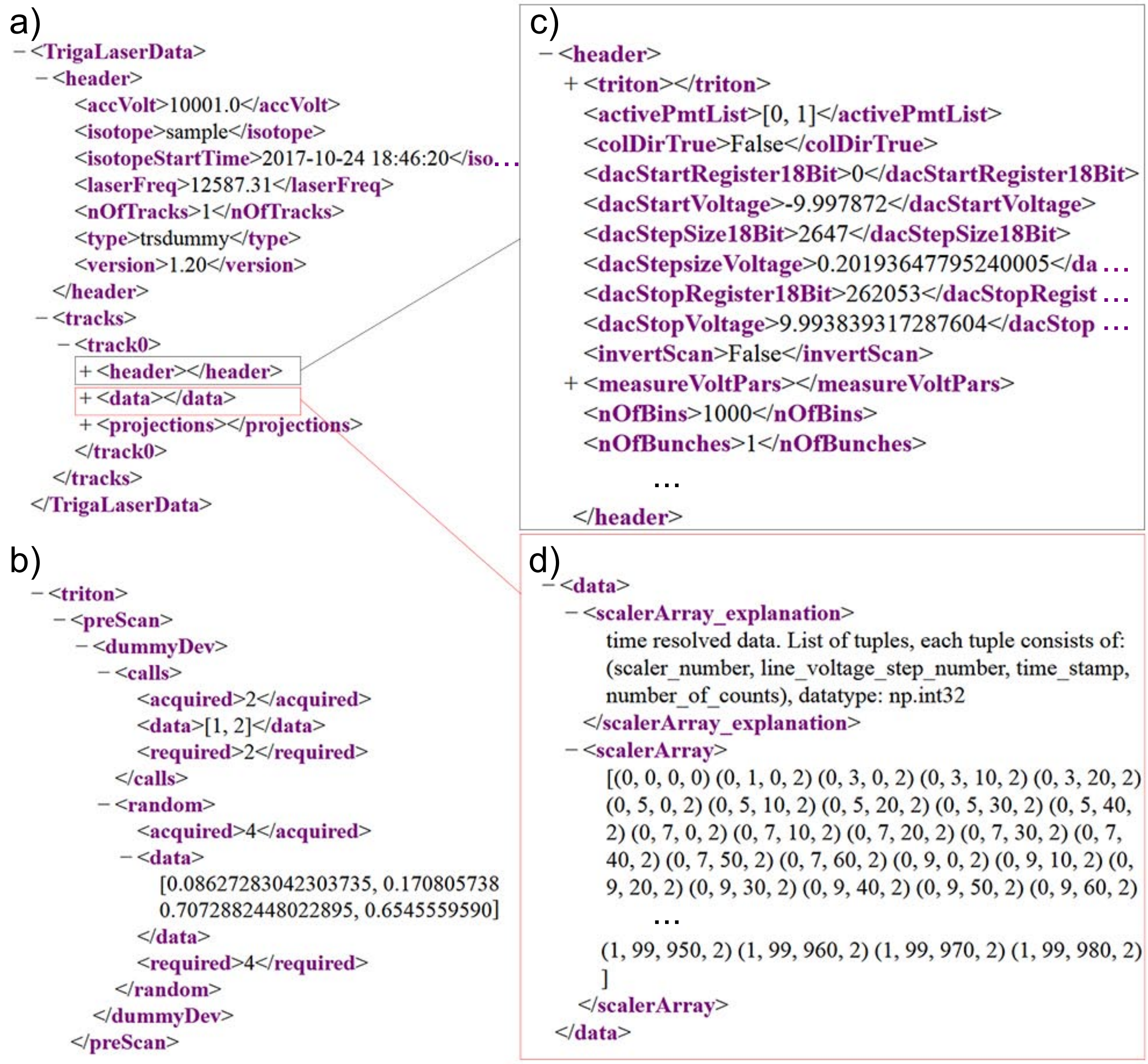

```
– <TrigaLaserData>
  – <header>
      <accVolt>10001.0</accVolt>
      <isotope>sample</isotope>
      <isotopeStartTime>2017-10-24 18:46:20</iso...
      <laserFreq>12587.31</laserFreq>
      <nOfTracks>1</nOfTracks>
      <type>trsdummy</type>
      <version>1.20</version>
    </header>
  – <tracks>
    – <track0>
      + <header></header>
      + <data></data>
      + <projections></projections>
      </track0>
    </tracks>
  </TrigaLaserData>
```

```
– <triton>
  – <preScan>
    – <dummyDev>
      – <calls>
          <acquired>2</acquired>
          <data>[1, 2]</data>
          <required>2</required>
        </calls>
      – <random>
          <acquired>4</acquired>
        – <data>
            [0.08627283042303735, 0.170805738
            0.7072882448022895, 0.6545559590]
          </data>
          <required>4</required>
        </random>
      </dummyDev>
    </preScan>
```

```
– <header>
  + <triton></triton>
    <activePmtList>[0, 1]</activePmtList>
    <colDirTrue>False</colDirTrue>
    <dacStartRegister18Bit>0</dacStartRegister18Bit>
    <dacStartVoltage>-9.997872</dacStartVoltage>
    <dacStepSize18Bit>2647</dacStepSize18Bit>
    <dacStepsizeVoltage>0.20193647795240005</da ...
    <dacStopRegister18Bit>262053</dacStopRegist ...
    <dacStopVoltage>9.993839317287604</dacStop ...
    <invertScan>False</invertScan>
  + <measureVoltPars></measureVoltPars>
    <nOfBins>1000</nOfBins>
    <nOfBunches>1</nOfBunches>
          ...
  </header>
```

```
– <data>
  – <scalerArray_explanation>
      time resolved data. List of tuples, each tuple consists of:
      (scaler_number, line_voltage_step_number, time_stamp,
      number_of_counts), datatype: np.int32
    </scalerArray_explanation>
  – <scalerArray>
      [(0, 0, 0, 0) (0, 1, 0, 2) (0, 3, 0, 2) (0, 3, 10, 2) (0, 3, 20, 2)
      (0, 5, 0, 2) (0, 5, 10, 2) (0, 5, 20, 2) (0, 5, 30, 2) (0, 5, 40,
      2) (0, 7, 0, 2) (0, 7, 10, 2) (0, 7, 20, 2) (0, 7, 30, 2) (0, 7,
      40, 2) (0, 7, 50, 2) (0, 7, 60, 2) (0, 9, 0, 2) (0, 9, 10, 2) (0,
      9, 20, 2) (0, 9, 30, 2) (0, 9, 40, 2) (0, 9, 50, 2) (0, 9, 60, 2)
          ...
     (1, 99, 950, 2) (1, 99, 960, 2) (1, 99, 970, 2) (1, 99, 980, 2)
      ]
    </scalerArray>
  </data>
```

Figure 3.10.: TILDA sample xml file, a) the main xml structure with the file header, followed by the tracks and their headers. b) example of a TRITON preScan measurement, shown expanded in xml. c) extract of an expanded track header. d) excerpt of an example time-resolved data set.

3.3 Tools

The toolbox of TILDA is adjusted to the needs of CLS experiments, but can be easily extended by other tools. The existing tools at the time of writing for TILDA version 1.22 will be explained shortly in the following sections.

3.3.1 Simple counter

The simple counter module is foreseen to measure and display the continuous count rates from the PMTs. The PMT events are counted for 200 ms and averaged over the last second on the host PC and the count rate is always shown in counts per second. In Fig. 3.11 the GUI of the simple counter is shown, with the channel numbers on the left followed by the current counts per second and a plot of the last seconds versus time. In the lower part, one can also control the active switch of the high-voltage switch-box, see chapter 3.1.5 and the active voltage output of the DAC. This combined allows the user to optimize the laser path through the beam line by reducing the count rate caused by its stray light. Furthermore once a resonance has been found in normal scanning procedure the user can optimize the ion beam and laser overlap by setting the DAC voltage to the resonance, observe the count rate on the screen and either change the laser path or the ion beam slightly until a maximum is found. In a next step the user can change the voltage again to a non resonant condition and by switching between both conditions estimate the signal to background ratio and keep optimizing in this way.

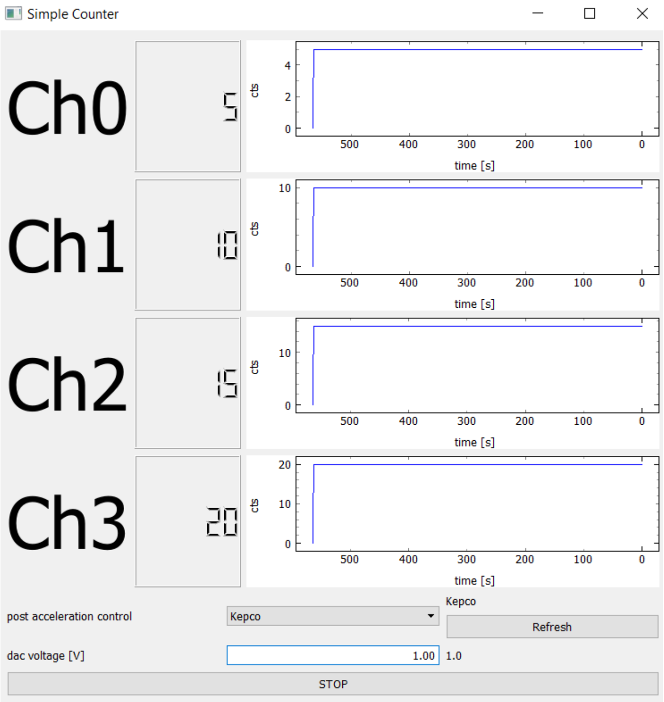

post acceleration control: Kepco

Kepco

dac voltage [V]: 1.00 1.0

Figure 3.11.: Simple counter GUI in a dummy operation with four active Channels.

3.3.2 Digital multimeter control

The digital multimeter (DMM) control tool combines all DMMs that are controlled by TILDA. The user has the standard options each DMM provides and some more TILDA-unique selections like the *Assignment* of the DMM. The assignment states if the DMM will be measuring the main acceleration voltage of the ions (*accVolt*) or the post acceleration voltage for the doppler-tuning (*offset*) and clarifying this eases the data analysis. Each DMM has an automatically created GUI to provide the individual parameters of each DMM. Before each scan the DMMs are set up according to the parameters defined in the scan settings.

3.3.3 TRITON listener

TRITON is a python based control system used in many CLS experiments for the slow controls like power supplies for the ion optics or a wavemeter for reading the laser wavelength [Gor17]. PCs in TRITON use the pyro4-package and broadcast the information and controls of the devices connected to them via Ethernet socket connection among each other. Some of these parameters like the wavelength are relevant for the analysis of the data and should therefore also be available in TILDA, hence the *TRITON-listener* tool was developed. It polls the pyro4-addresses of the TRITON-PCs from a common SQL database and connects to the relevant data channels of the devices, selected by the user. The data can be acquired at any time during the measurement of each track and can be stored to the xml-file into the triton layer in the header of each track, see Fig. 3.10b. Future plans foresee a bidirectional communication between TILDA and the TRITON devices in order to integrate them also in TILDA's scanning procedure.

3.3.4 Power supply control

This is a tool to control the high-voltage power supplies which are connected to the post acceleration region. Heinzinger power supplies are used at TRIGA-Laser and ALIVE/KOALA, which can be controlled via an RS-232 or Ethernet interface. TILDA ensures to set the voltages latest before the measurement of each track, but the user can also set the required voltages in advance, to have time for them to settle and stabilize before the measurement of the actual track. Currently it is possible to set three power supplies but it can be easily expanded for more and for other brands.

3.3.5 Pulse pattern generator - PPG

TILDA's PPG is developed as universal tool for controlling time relevant devices by distributing TTL-pulses during scanning, like for example the release of the RFQCB. A pulse pattern generator based on LabVIEW-FPGAs was already developed [Zie12] at GSI and the code could be adapted for TILDA, as discussed in section 3.2.5. The PPG can hold up to 1000 commands and they can be transferred from the host PC to the FPGA via a DMAC-channel while the PPG is running. Commands can be either *wait*, in order to hold the pattern until a trigger is received on the desired input, *time* to set the desired channels high for a given time or *stop* for setting the desired channels high at stop of the pattern. 64 output channels and 16 trigger inputs could be used and half of each of them are used within one TTL-Linedriver module in TILDA. In TILDA,

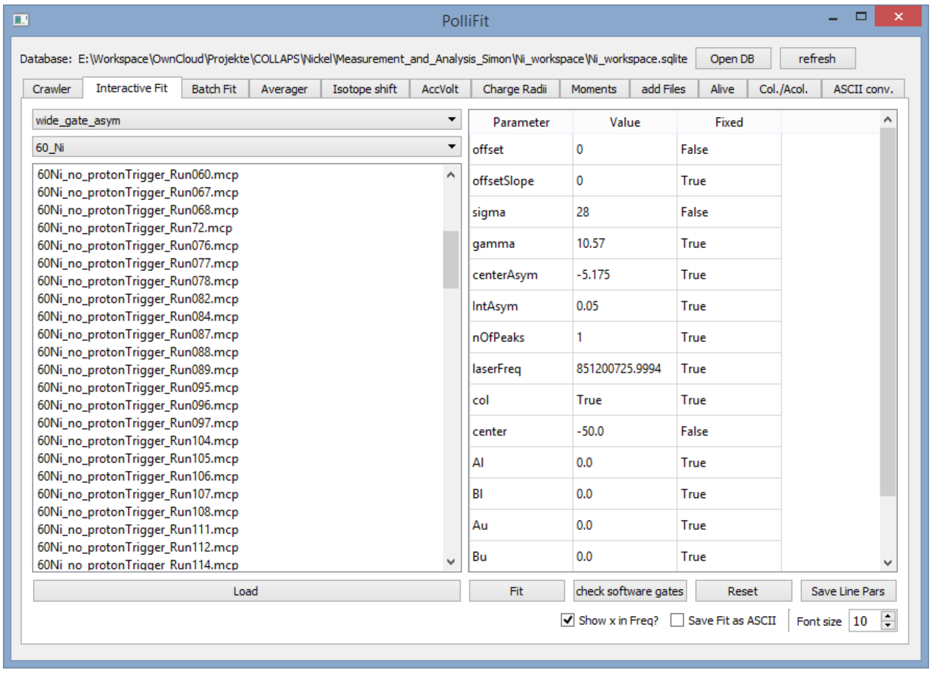

Database: E:\Workspace\OwnCloud\Projekte\COLLAPS\Nickel\Measurement_and_Analysis_Simon\Ni_workspace\Ni_workspace.sqlite

wide_gate_asym

60_Ni

60Ni_no_protonTrigger_Run060.mcp
60Ni_no_protonTrigger_Run067.mcp
60Ni_no_protonTrigger_Run068.mcp
60Ni_no_protonTrigger_Run72.mcp
60Ni_no_protonTrigger_Run076.mcp
60Ni_no_protonTrigger_Run077.mcp
60Ni_no_protonTrigger_Run078.mcp
60Ni_no_protonTrigger_Run082.mcp
60Ni_no_protonTrigger_Run084.mcp
60Ni_no_protonTrigger_Run087.mcp
60Ni_no_protonTrigger_Run088.mcp
60Ni_no_protonTrigger_Run089.mcp
60Ni_no_protonTrigger_Run095.mcp
60Ni_no_protonTrigger_Run096.mcp
60Ni_no_protonTrigger_Run097.mcp
60Ni_no_protonTrigger_Run104.mcp
60Ni_no_protonTrigger_Run105.mcp
60Ni_no_protonTrigger_Run106.mcp
60Ni_no_protonTrigger_Run107.mcp
60Ni_no_protonTrigger_Run108.mcp
60Ni_no_protonTrigger_Run111.mcp
60Ni_no_protonTrigger_Run112.mcp
60Ni_no_protonTrigger_Run114.mcp

Parameter	Value	Fixed
offset	0	False
offsetSlope	0	True
sigma	28	False
gamma	10.57	True
centerAsym	-5.175	True
IntAsym	0.05	True
nOfPeaks	1	True
laserFreq	851200725.9994	True
col	True	True
center	-50.0	False
Al	0.0	True
Bl	0.0	True
Au	0.0	True
Bu	0.0	True

☑ Show x in Freq? ☐ Save Fit as ASCII Font size 10

Figure 3.12.: Main window of PolliFit, the analysis framework for TILDA, with the Interactive Fit tab highlighted.

the base frequency of the PPG was adapted to 100 MHz matching the frequency of the DAF and for better communication between DAF and pulse-pattern FPGA, the ouputs of channels 0, 8 and 16 are copied to the PXI-backplane, sparing external wiring between the two modules.
The syntax of the commands for the PPG were kept the same as in [Zie12], so for example setting channel 0 high for 2 μs the command would be *$time::2.0::1::0* with the order *$cmd::[time / μs]::[act. channel 0-31 /* 2^{Ch}*]::[act. channel 32-63 /* 2^{Ch}*]*. A whole pulse pattern can be entered via a list of those commands in a text file. More comfortable, this list of commands can also be automatically generated from the choices in one of the graphical user interfaces. Either the *simple* user interface which is specialized on a CLS setup with an RFQCB, a beam gate in front and dependent on a proton trigger as it is used at the COLLAPS experiment. Alternatively the *periodic-pattern* GUI provides a less CLS-specific GUI, where the user can select which channel should give a pulse how often.

3.3.6 PolliFit

Analysis of the collected data is performed with the Python cOLLInear FITter (PolliFit) framework which was developed for analyzing any kind of data from a CLS-experiment and its fit routine is based on the python package *sciPy*. PolliFit as a project on its own is imported into TILDA by a git *subtree* in order to synchronize both development branches on regular intervals. The variety of data types in different CLS-experiments is handled by different data importing modules within PolliFit, all leading to a similar data object representing an acquired spectrum which is fitted in the end. All data is fitted in frequency units in order to account for the nonlinear relativistic Doppler shift. Performed analysis results are stored in a sqlite-database from which they can be combined and extracted easily. The sqlite-database also holds the key information of all acquired files, which can be expanded by information not available in the single files such as the scaling factor for the x-axis, which is usually measured in a *Kepco-Scan*, where the Doppler-tuning-voltage is ramped over the full range and the output is measured with a digital multimeter. In another table of the sqlite-database all relevant isotopes are stored with their CLS-relevant information such as the mass, spin, etc.. Also the used transition and the different analysis settings are stored in the sqlite-database. TILDA yet adds another table to the sqlite database in order to store the scan parameters for the isotopes.

PolliFits GUI is perfectly adapted for a detailed online analysis during an experimental campaign and gives the user the opportunity to directly see the average of any fit result and it also can directly calculate and display the isotope shift to the reference isotope for monitoring purposes. The main window of PolliFits GUI is shown in Fig. 3.12 with the Interactive Fit tab selected, which can be used to determine the starting parameters for a fit. Several other tools like a batch fitting tool have been developed and are organized in the other tabs of the GUI.

3.4 Summary and outlook

Within this work TILDA was fully developed and its functionality was proven at several facilities. All problems that occurred during the development process were addressed and resolved. TILDA's time resolution and its other features, like the included pulse pattern have proven to be a valuable improvement to the existing data acquisition system, which was built for continuous CLS. Bunched beam measurements were realized with an improvised external solution, see chapter 4.2.5. TILDA is currently in use at three collinear laser spectroscopy experiments, the KOALA experiment (KOllineare Apperatur für Laserspektroskopie und Angewandte Wissenschaften) in Darmstadt, the COLLAPS experiment (COLLinear APplied Spectroscopy) at CERN-ISOLDE and the TRIGA-Laser experiment, currently situated at Argonne, which will be transported to the FAIR facility in Darmstadt within the next years. Furthermore TILDA was installed in 2018 at CRYRING [Les16], a storage ring connected to the experimental storage ring (ESR) at GSI. Here a CLS-experiment on bunched beams in the storage ring is planned in the near future and in first tests with the already installed optical detection region, TILDA could provide information on the bunch length and storage times from the beam related light. The collinear laser spectroscopy at a storage ring must be realized without Doppler-tuning of the ions, hence TILDA is currently being manipulated in order to be able to scan the laser frequency. Thanks to TILDA's layout those changes can easily be integrated in the scanning process and will make TILDA more versatile.

4 Spectroscopy of nickel at COLLAPS

The following sections represent the scientific part of this work and will focus on the collinear laser spectroscopy measurements on nickel performed in 2016 and 2017 at the COLLinearly APplied Spectroscopy (COLLAPS) experiment at CERN-ISOLDE (Conseil Européen pour la Recherche Nucléaire - Isotope Separator OnLine DEvice). The first beam time was performed with the old COLLAPS Data Acquisition (DAQ) while TILDA ran only in a parasitic mode. The second beam time was the first one in which TILDA was operated as the main DAQ system. Relevant properties of nickel isotopes are introduced in chapter 4.1 complemented by the transition that was probed in this work. This is followed by a detailed description of the experiment the DAQ setups, counteractions against isobaric contamination from ^{70}Ga and a summary of the main differences between the 2016 and 2017 beam times.

4.1 Nickel - general properties and spectroscopic transition

Ni 56	Ni 57	Ni 58	Ni 59	Ni 60	Ni 61	Ni 62	Ni 63	Ni 64	Ni 65	Ni 66	Ni 67	Ni 68	Ni 69	Ni 70	Ni 71	Ni 72	Ni 73
6.075 d	36.0 h	68.0769	$7.5 \cdot 10^4$a	26.2231	1.1399	3.6345	100 a	0.9256	2.52 h	54.6 h	21 s	29 s	11.4 s	6.0 s	2.56 s	1.57 s	0.84 s

Figure 4.1.: Excerpt from the chart of nuclides with the nickel isotopes ($Z = 28$) from $N = 28$ to $N = 45$ which have been targeted in this work. Stable isotopes are black, blue background stands for β^- decay and red represents β^+ decay or electron capture.

Nickel nuclei contain 28 protons and are therefore proton-magic since the $1f_{7/2}$ proton shell is completed and the energy gap to the $2p_{3/2}$ proton shell is comparably large as can be seen in Fig. 2.1. Nickel is the first proton-magic element, that has no doubly magic stable isotope. Both doubly magic nuclei ^{56,78}Ni with the magic neutron numbers $N = 28$, 50 are radioactive. Just recently the Penning-trap experiment ISOLTRAP could confirm, by mass measurements and extraction of the binding energy of ^{79}Cu [Wel17], the magic character of ^{78}Ni. Mass measurements of ^{78}Ni itself are unfortunately still not feasible due to the difficult production of nickel isotopes and until now only its half-life [Xu14] and some γ transitions [Tan19] could be studied directly. At ISOLDE special counteractions are taken to enhance the yield of Ni and these will be described in detail in chapter 4.2.1. Thereby ISOLDE is able to provide one of the highest yields of neutron-rich nickel in the world compared to other ISOL facilities. Based on ISOLDE's yield database the isotopes $^{56-73}$Ni, as they are shown in Fig. 4.1, should be available for bunched beam collinear laser spectroscopy where roughly some hundreds of ions per second are required. While not being able to reach the doubly magic isotope ^{78}Ni, the isotope ^{68}Ni, for which all odd-parity states in the $pf\,g_{9/2}$ shell are occupied, is well in reach for this experiment. It is expected that the information gained from the change in mean-square charge radii will give more insight on this sub-shell closure between the pf and $g_{9/2}$ neutron sub shells at $N = 40$ that seems to cause the semi magic properties of ^{68}Ni. This effect has been seen in the neighboring isotopes copper [Bis16], zinc [Xie18] and gallium [Che10] with an increase of this effect towards the magic proton number of nickel. This will be elaborated more along with the discussion of the results in nickel in chapter 5.2.4.

Nickel offers a huge variety of accessible transitions for laser spectroscopy in the atom, but does not allow laser spectroscopy within the ion due to the very high excitation energy out of the ground state. Therefore, the nickel ions were neutralized in a charge exchange cell (see, chapter 4.2.3) after production and transportation to the COLLAPS experiment. The neutralization process is non-resonant and therefore various states of the nickel atoms are populated including the meta stable $3d^9 4s\,^3\mathrm{D}_3$ [Ryd15]. From this state, the $4p\,^3\mathrm{P}_2$ can be excited resonantly with a laser at a wavelength of about 352.45 nm in the rest frame of the ion as it is shown in Fig. 4.2. This transition was chosen, for four reasons:

- efficiency: about 88% of the atom return to the lower level and can be multiple excited to increase the fluorescence signal
- wavelength: the laser wavelength can be produced with a frequency-doubled titanium:sapphire laser.
- sensitivity in $\delta\langle r^2\rangle$: an s-electron is involved in the transition leading to a large $\Delta|\chi(0)|^2$
- hfs resolution: the J values provide a firm assignment and sensitivity to magnetic dipole and electric quadrupole moments.

Masses and spins of the investigated isotopes in this work are summarized in Tab. 4.1.

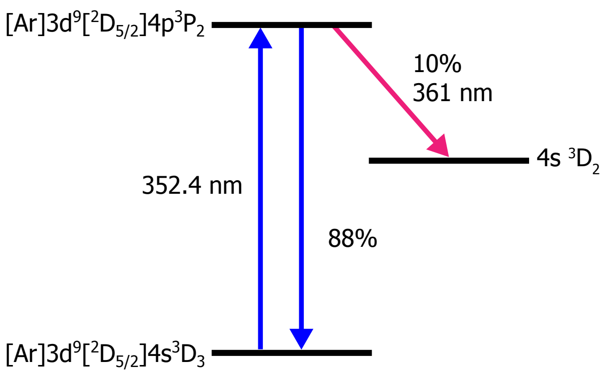

Figure 4.2.: Level schematic of the probed transition in nickel.

A	I^π	ref.	m / μu
58			57 935 341.8(4)
59	$3/2^-$	[Yu02]	58 934 345.6(4)
60			59 930 785.3(4)
61	$3/2^-$	[Sto14]	60 931 054.9(4)
62			61 928 344.9(5)
63	$1/2^-$	[Mül89]	62 929 669.1(5)
64			63 927 966.3(5)
65	$5/2^-$	[Sto14]	64 930 084.7(5)
66			65 929 139.3(15)
67	$1/2^-$	[Sto14]	66 931 569(3)
68			67 931 869(3)
70			69 936 431.3(23)

Table 4.1.: Spins in the ground state and masses of the relevant nickel isotopes [Wan17]

4.2 Setup

4.2.1 Isotope separator online device - ISOLDE

ISOLDE [Cat17] is a Radioactive Ion Beam (RIB) facility situated nearby Geneva at the Meyrin-site of CERN and integrated in CERNs accelerator infrastructure. A 3D-Model of the inside of the ISOLDE hall is shown in Fig. 4.3 with a short description in the figure caption. At ISOLDE numerous isotopes of elements from helium up to radium ($Z = 88$) are accessible even if the lifetime is in the millisecond range. These isotopes are produced by nuclear reactions (spallation, fission and fragmentation) generated by a 1.4 GeV proton beam hitting the target. Several online separation mechanisms are combined in order to generate a pure radioactive ion beam

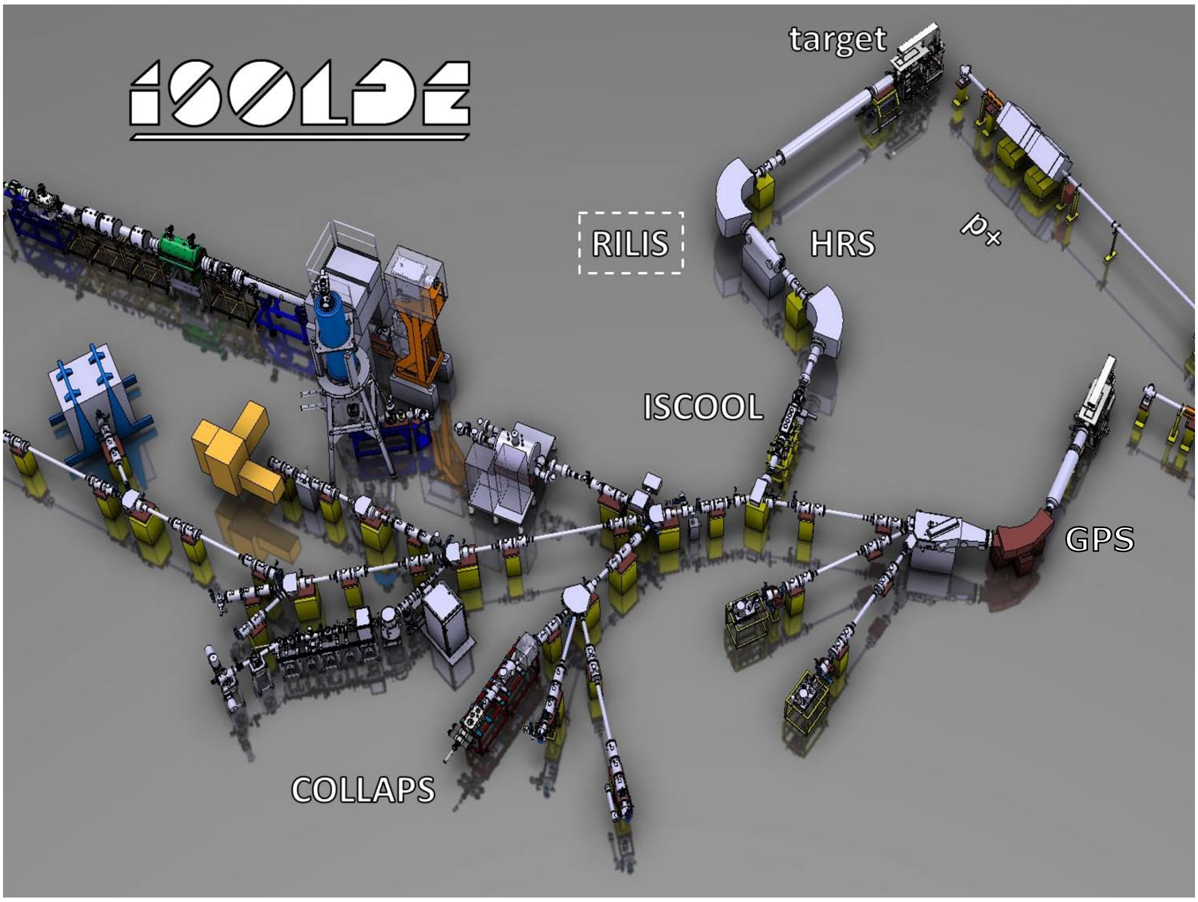

Figure 4.3.: Layout of ISOLDE with protons coming from the right hitting either the General Purpose Separator (GPS) or High-Resolution Separator (HRS) target, producing radioactive isotopes by spallation, fission and fragmentation. Each frontend is named after their consecutive mass separator which removes unwanted isotopes from the beam and allows only ions of a specific mass-to-charge ratio to pass and to be distributed via a common beam line to the experiment which is currently taking the beam. Isobars from the production are partially suppressed from the element-selective resonance ionization laser ion source (RILIS). In this work HRS was used and ions were cooled and accumulated in ISCOOL before they were guided to the COLLAPS beam line.

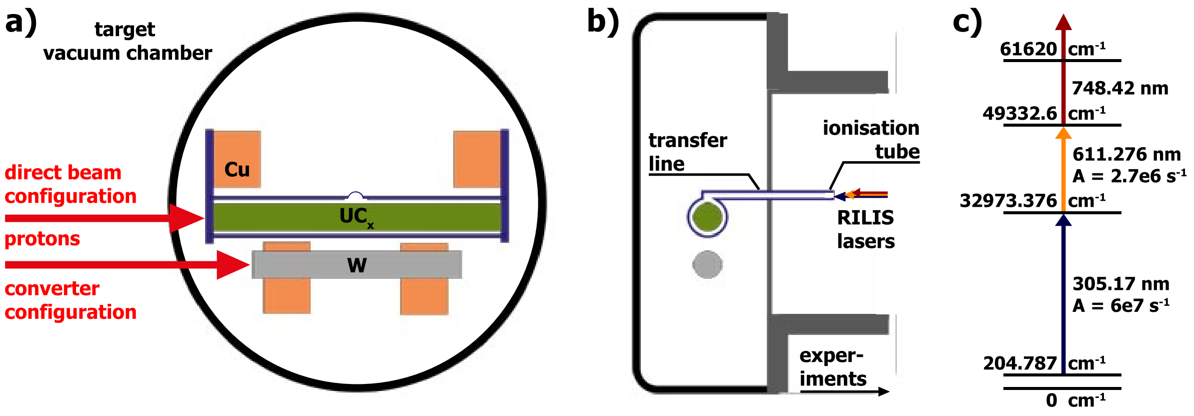

Figure 4.4.: Front view a) and side view b) schematic drawing of a typical ISOLDE target with the main target rod containing UC$_x$ and the proton-to-neutron converter rod below. Ionization lasers from the RILIS setup can be send directly into the ionization tube. c) RILIS three step ionization scheme for nickel used in this work.

of ideally only one isotope with a yield as high as possible. An overview of the production and separation mechanisms relevant for this work are briefly summarized.

ISOLDE uses 1.4 GeV protons which are delivered from the Proton Synchrotron Booster (PSB) with averaged beam currents of up to 2 μA and a repetition period of 1.2 s. In general a continuous proton beam would be often preferable for ISOLDE, because the proton pulses stress the target by depositing a huge amount of energy on a very short time scale. On the other hand, the pulsed mode has an advantage for some experiments since the production becomes time dependent and isotopes are released from the target on different time scales depending on their individual properties. In fact, this was very useful for the case of ^{70}Ni as discussed below.

Targets at ISOLDE are a research field on their own and only a brief summary of aspects relevant for this work will be given. The general layout of the target is shown in Fig. 4.4. A thick target rod is filled with material suited for the production of the desired isotope either by spallation, fission or fragmentation caused by the impinging protons. For the production of nickel isotopes, uranium carbide (UC$_x$) was used. Reaction products evaporate from the target material and effuse eventually through the transfer line into the ionization area. In order to enhance the diffusion out of the target material and through the transfer line both are additionally heated resistively by applying high currents. In 2016 the target was heated with up to 590 A, corresponding to a temperature of 2100 °C while in 2017 up to 675 A were applied to reach a temperature of roughly 2190 °C, which is about the limit for safe operation. By the nature of the production principle, a large variety of elements and isotopes are produced. Isobars of the desired isotopes can be present and their number can exceed those of the isotope of interest by orders of magnitude. Even though the laser spectroscopic process is very selective, the isobars can cause beam-induced background and swamp the RFQCB. In our case an isobaric contamination of gallium ($Z = 31$) was expected to be the dominant beam contamination for the nickel isotopes around ^{70}Ni. In order to suppress the Ga production the target was equipped with a proton-to-neutron converter, a thick tungsten rod mounted below the main target container, as shown in Fig. 4.4. In this case the proton beam is directed onto the tungsten rod and neutrons produced by spallation are emitted in all spatial directions with some MeV energies. The dominant process in the target material is then neutron-induced fission and particularly the

ratio of neutron-rich isotopes to neutron-deficient isobars is strongly enhanced compared to a direct bombardment of the target [Cat03]. Unfortunately, the production yield of nickel was too low when using the converter setup. Hence, the beam was directed onto the target in order to have a more efficient production. In 2016 an experimental target was used: The inside of the ionization tube was replaced by a graphite tube instead of the usually used tungsten tube. In order to reduce the release time of nickel from the surface. However, such an effect was not noted and in the second beam time a standard target was used again. For ionization of the nickel atoms inside the tube resonant laser ionization (RILIS) [Fed08] was used, applying the three step ionization scheme shown in Fig. 4.4 c. Therefore the beams of three pulsed lasers were superimposed and coupled into the beam line via a view port in the HRS magnet directly into the ionization area of the target as shown in Fig. 4.4 b. Ions are then extracted from the target that is located on a high-voltage platform, towards the beam line on ground potential. In 2016 the target was operated at 30 kV and in 2017 40 kV were used.
At ISOLDE there are two target stations available, which differ mostly by their successive beam separation stages. One is connected to the GPS and the other one to the HRS. Due to the low yields of nickel we used the HRS target station since this is connected to the radio frequency cooler and buncher ISCOOL.

4.2.2 Isolde cooler - ISCOOL

The Radio Frequency Cooler and Buncher (RFQCB) better known as the ISolde COOLer (ISCOOL) [Fra08] is directly situated after the HRS and has the purpose to reduce the beam emittance. Further it can optionally trap the ions for a short period of time in order to produce a pulsed ion beam. The bunching mode is used for collinear laser spectroscopy since it significantly reduces background from scattered laser light as discussed in the next section.
A schematic drawing of its structure and operational principle is shown in Fig. 4.5. The ions entering the RFQCB are decelerated by a positive potential applied to the whole ISCOOL platform, which is slightly lower than the high-voltage at the ion source. Therefore the beam energy is reduced to typically 30 eV. All following voltages are applied on top of this high-voltage, thereby the *ground* potential is actually at about $-30/-40$ kV relative to ISCOOL.
ISCOOL is filled with He gas as a buffer gas at a pressure of typically 10^{-2} mbar. The injected ions collide with the He atoms and dissipate energy until they are in thermal equilibrium with the gas. In order to keep the ions axially confined during this process, four segmented rods are installed along the inside of ISCOOL and a radio frequency U_{RF} is applied as shown on the right in Fig. 4.5, creating an alternating quadrupole field repelling the ions towards the axis of the quadrupole.
The quadrupole rods within ISCOOL are segmented along the longitudinal-axis and each segment can be supplied with a dc voltage in addition to the radio frequency. In this way a dc potential as shown in the lower part of Fig. 4.5 can be realized. On the first segment a potential difference is applied, which is typically about 25 V below the required potential to stop the beam completely. The following segments are supplied with a fraction of this injection voltage with the lowest potential at the second to last segment as it is shown in Fig. 4.5. Thereby the ions are cooled into this potential minimum. The last segment can be altered between a trapping potential (around 50 V) and an ejection potential (ground). Inside this potential dwell the ions are reflected back and forth after injection and are accumulated in the potential minimum and get to a thermal equilibrium with the helium gas. After some accumulation time the ions can

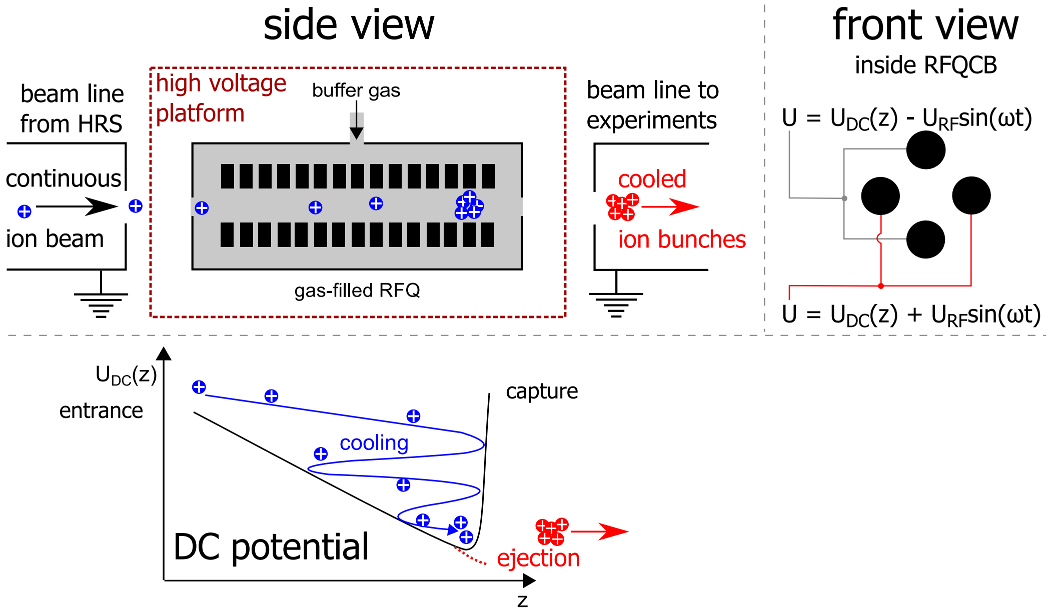

Figure 4.5.: Schematic view of ISCOOL's working principle for accumulating and cooling the ions. Ions are decelerated by a high-voltage applied to the whole ISCOOL platform before they can release most of their remaining energy by buffer gas collisions until they are in thermal equilibrium with the buffer gas. Transverse trapping is realized by an alternating quadrupole field created from a radio frequency voltage applied to the four segmented quadruole rods along the z-axis (right). A DC potential in axial direction created by applying DC voltages to the segments of the quadrupole rods allows to create a potential well to trap the ions in the z-direction. Thereby up to 10^6 ions can be accumulated before releasing them as an ion bunch by ramping down the last electrode.

be extracted as a cloud of ions from ISCOOL, the potential at the last segment is pulled down, hence the ions are accelerated by the ground potential of the main beam line.
About 10^6 ions can be accumulated in ISCOOL, before space charge effects significantly influence the beam and bunch properties. At larger ion numbers the ion cloud spreads inside ISCOOL due to space charge of the cloud and ions are forced to stay at higher potentials and the energy spread as well as the extraction time will increase. Both deteriorate the conditions for CLS drastically, but systematic studies on this are yet to be performed during the shutdown year of ISOLDE in 2020.

4.2.3 Collinear laser spectroscopy at COLLAPS

The COLLAPS experiment has been permanently situated at ISOLDE since its first installation in 1979 [Neu81a; Mül83]. During the 40 years of operation a large number of isotopes and elements were investigated making COLLAPS the most productive of all collinear laser spectroscopy stations world wide. The COLLAPS setup has been developed throughout the years in order to increase sensitivity and accuracy of the whole experiment. This development has been reviewed several times, the latest one published in 2017 [Neu17]. An schematic drawing of the relevant modules for CLS installed at the COLLAPS beam line is shown in Fig. 4.6. The

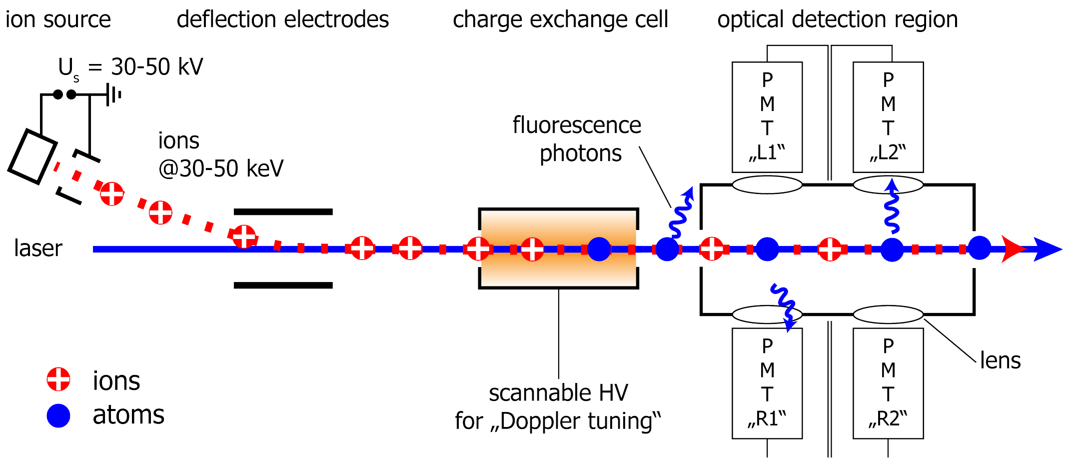

Figure 4.6.: Schematic drawing of a CLS setup. Ions are accelerated to energies of 30-50 keV, before they are superimposed with the laser beam. Within a CEC ions can be neutralized by passing through a dense alkali vapor. Atoms excited by the laser beam, will emit fluorescence photons from spontaneous emission, which can be detected by a PMT. This count rate in relation to the laser frequency reveals the transmission frequency.

ion beam is superimposed with the laser beam in collinear geometry by using several pairs of steering electrodes in horizontal and vertical direction. The first horizontal deflector deflects the ion beam by about 10° to superimpose it with the laser beam. The laser is introduced into the beam line through a view port mounted at Brewster angle to minimize reflections. At the opposite end of the beam line the laser beam leaves through a second view port. This allows to monitor the power and positioning of the laser during measurements and minimizes stray light inside the beam line. The overlap of laser and ion beam is optimized by introducing narrow apertures in the beam line through which the laser beam and the ion beam are guided for maximum transmission. The apertures are removed after the optimization process to reduce stray light from reflection and refraction of the outer part of the laser beam. Inside the CEC they pass through a dense alkali vapor produced by heating the CEC until the charge exchange efficiency of about 50% is reached. Operating conditions for 2016 and 2017 can be found in Tab. 4.2. Atoms leaving the CEC might be excited by the laser to a higher energy level if the charge exchange populated the lower level of the transition and the laser frequency in their rest frame matches the resonance condition. The excited atoms will spontaneously decay and emit photons while passing the Optical Detection Region (ODR) which can be collected by one of the four PMTs.

The ion velocity can be varied to match the Doppler condition by a high-voltage of up to ±10.5 kV which is applied to the Charge Exchange Cell (CEC). This voltage can be ramped quickly and is used for the scanning process. This allows to keep the frequency of the laser fixed throughout the whole beam time. This technique is usually used in CLS and is called *Doppler-tuning*, as explained in chapter 2.3.

The main background in CLS with fluorescence detection arises from laser stray light. The creation of short ion bunches with ISCOOL allows to efficiently suppress this background. It was one of the major developments for higher sensitivity in CLS [Nie02]. This technique is used at COLLAPS since 2008 and was also applied in this work: The ion beam delivered by ISOLDE was accumulated within ISCOOL for typically about 50 milliseconds and then a cloud of up to 10^6

ions was extracted towards the COLLAPS beam line. Fluorescence detection can be limited to the few μs while the ion bunch is inside the detection region. Thereby the constant background from the laser stray light, is drastically reduced by the ratio of bunch length and accumulation time

$$\text{backgr. suppression} = \frac{\text{temporal bunch length}}{\text{accumulation time}} = \frac{\sim 5\,\mu\text{s}}{\sim 50\,\text{ms}} \approx 10^{-4}\,. \tag{4.1}$$

This reduction of almost 4 orders of magnitude allowed at COLLAPS for example the measurement of ^{52}Ca with ion beams as low as a few 100 ions/s. The limitation in these cases is often the beam induced background from contaminations within the beam. Therefore special counter actions have to be performed as it was the case for ^{70}Ni and is described in chapter 4.2.6.

4.2.4 Laser system

The rest frame frequency of the transition requires a wavelength of about 352.45 nm which for collinear excitation and ion energies of 30 keV (2016) and 40 keV (2017) corresponds to laboratory wavelength of 352.199 nm and 352.143 nm, respectively. A tunable titanium-sapphire ring laser (Sirah, Matisse TS) pumped by 10 W of a frequency-doubled, diode-pumped Verdi V18 (Nd:YVO4, Coherent) solid state laser at 532 nm generated about 1.3 W at ~704 nm. The fundamental light from the titanium-sapphire laser was coupled into a frequency doubling cavity (Spectra-Physics, Wavetrain) built in a delta geometry with a non linear crystal in the focal plane creating the second harmonic with an efficiency of about 15% resulting in a typical output power of around 200 mW at 352 nm. This light is guided from the laser lab to the COLLAPS experiment inside the ISOLDE hall via a periscope and a guiding tube system across a distance of about 15 m towards the laser coupling station just in front of the COLLAPS beam line. The central part of the coupling station is a spatial mode-cleaner that is used to remove unwanted beam distortions by higher TEM modes. This is realized by a narrow pinhole with a diameter of $\sim 50\,\mu$m positioned in the focal plane of a lens. A second lens behind the pinhole collimates the beam again with a diameter of around 5 mm.

The titanium-sapphire laser frequency is short-term stabilized by locking to the error signal of an external cavity. Long-term drifts are corrected by measuring the wavelength with a high precision wavemeter (High Finesse, WSU-10) and adapting the length of the reference cavity to keep the wavelength constant. However the wavemeter itself is also prone to long-term drifts due to temperature and pressure changes and needs to be calibrated in regular intervals with a reference providing a well-known frequency. This lead to issues that are discussed in chapter 5.2.1.1.

4.2.5 Data acquisition system - DAQ

In 2016 the well established DAQ system Master Control Program (MCP) was still in use as the main DAQ, while the newly developed TrIga Laser Data Acquisition system TILDA was operated in parasitic mode only. In 2017 TILDA was operated as the main DAQ for the first time. The DAQ setups in both beam times are compared in Fig. 4.7 and 4.8 and the differences will be briefly summarized:

The least change occurred to the generation of the Doppler-tuning-voltage as it is shown on the left-hand side of both figures. It requires three stages, a fast 18-Bit high-precision Digital-to-

Analog Converter (DAC), which is controlled by the DAQ with a range of ±10 V, followed by a linear bipolar amplifier (Kepco) which amplifies this voltage by a factor of about 50 generating a scanning range of up to ±500 V. This scan voltage supplies a high-voltage platform hosting three high-voltage power supplies (FLUKE) which are set to a constant voltage in the range of ±10 kV. This constant offset accounts for the isotope shift between the different nickel isotopes. Usually FLUKE-1 is permanently set to a high-voltage which corresponds to the required acceleration voltage for the reference isotope and FLUKE-2/3 are set to the required acceleration voltage of the next isotope in the measurement schedule. The advantage of this scheme is that the FLUKES have sufficient time to settle on the voltage which is kept fix while one isotope is measured even though scans of the reference isotope have to be performed several times during this interval.
The voltages and especially the Kepco amplification factor are measured by high-precision digital multimeters which are connected to a high-precision voltage divider. For details see Tab. 4.2. Since the total acceleration voltage determines the laser frequency in the rest frame of the ion, it is crucial to measure also the high-voltage which is applied to ISCOOL with high-precision to obtain the kinetic energy of the ions. The ISCOOL voltage is kept constant during the whole beam time, and is only measured at the beginning and at the end of each isotope measurement by another high-precision digital multimeter connected to a precise high-voltage divider (see

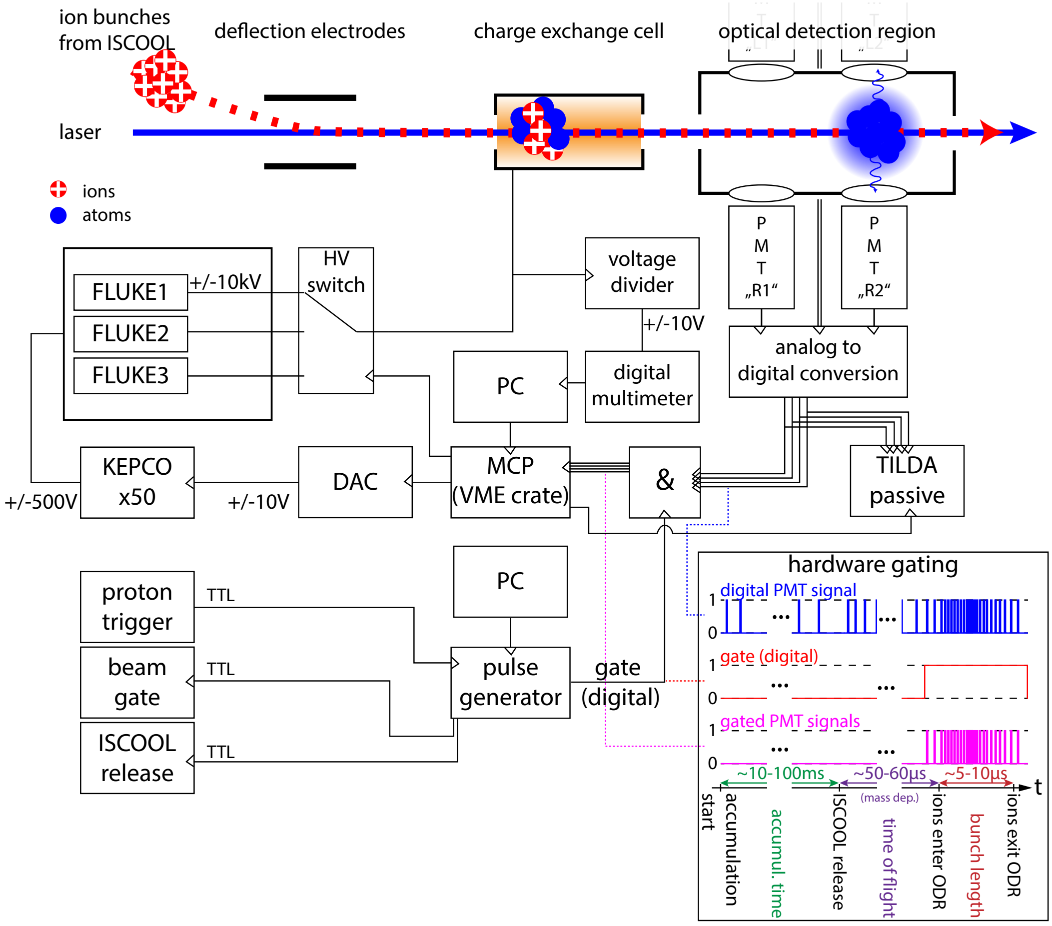

Figure 4.7.: Schematic drawing of the DAQ system used in 2016 with the Master Control Program (MCP) as the main DAQ. The inset on the lower right depicts the applied hardware gating technique of the digital PMT signals over a non-scaled time axis, details can be found in the text.

Tab. 4.2).

Fluorescence detection is performed at the ODR that follows the CEC which is equipped with four Photomultiplier-Tubes (PMTs). Analog signals from the PMTs are amplified, discriminated and the corresponding digital signals (TTL) are fed into the DAQ system. The treatment of these signals is one of the major difference between the two systems.

Fig. 4.7 shows the DAQ system as it was installed in 2016 when still operating with MCP. MCP was originally designed for CLS with continuous beams and in the era of bunched beam CLS, there was suddenly a need to equip it with some sort of time coincidence. This was realized externally using Nuclear Instrumentation Module (NIM) logic and coincidence units that are hard-wired as shown in the lower part of Fig. 4.7. A Pulse Pattern Generator (PPG) (Quantum Composers, 9520) was the central element of the time-gated detection. Based on the proton trigger, received from ISOLDE controls as a TTL-signal, the PPG creates the timing gates for the beam gate, an electrode blocking all ions from the target to avoid unwanted filling of ISCOOL, the accumulation and cooling time in ISCOOL, and the coincidence gate for fluorescence detection. The latter is determined by the ions time of flight after release from ISCOOL to the optical detection region. and the temporal length of the ion bunch. The detection gate (red pulse in inset) is then used in a coincidence (AND) module to transmit only those PMT-events occurring during bunch passage through the detection region to the counter (purple pulses in inset). This allowed us to still use the slow counters embedded in the MCP system with the fast bunch

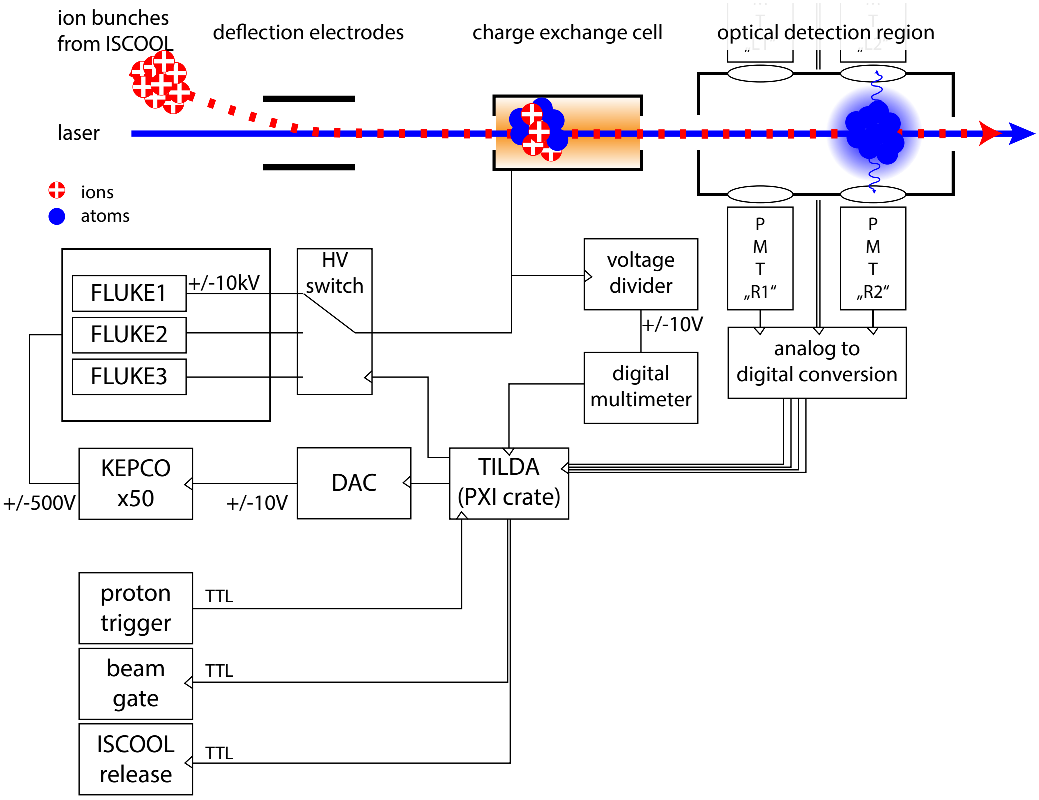

Figure 4.8.: Schematic drawing of the DAQ system used in 2017 with TILDA as the main DAQ, details can be found in the text. The external most important difference is the removed external digital gate. Instead, all photons within a reasonable period after releasing the bunch are recorded and timing information is included to apply software gates of reasonable time and length in post-analysis.

timing. The counters are activated for several milliseconds according to their specifications, but actually only acquire signals for a few microseconds. Arming and disarming of the counters in MCP happened while ISCOOL was accumulating ions and therefore no measurement time was lost due to the low resolution of the MCP counters. Setting the detection gate is most crucial in this scheme since it has to be adapted for each isotope and wrong settings can cause significant and irreversible signal loss. Expanding the detection gate too much, to ensure that the whole bunch is being detected, will on the other hand deteriorate the signal-to-noise-ratio.

During the first years of ISCOOL operation, multi-channel scalers were used to obtain information on the bunch structure and required timing. In the first nickel beam time, monitoring the temporal structure of the bunches and the gate adjustment was already realized by the new data acquisition system, but operated in a slave mode, called TILDA-passive, to provide the time-resolved capabilities of TILDA. In this way the gates could be set properly and the temporal structure of the bunches was monitored in order to detect anomalies. To do so, the user was required to check and initiate three PCs before each measurement: first the pulse pattern needed to be set, then TILDA-passive had to be activated and finally MCP could start the measurement. Unfortunately in some files, users missed to start TILDA-passive and therefore not all files recorded in MCP have a corresponding TILDA-passive file. Also MCP does not provide an auto save function and since the user had to change between these three PCs sometimes a file in MCP was not saved and some measurements had to be repeated unnecessarily. Needless to say that in some cases the timing of the gate pulses or the size of the ion bunch loaded into ISCOOL was too large and measurement time was wasted.

In 2017 TILDA became the main DAQ system at COLLAPS. Since TILDA inherits all functionalities, the setup and control of the experiment simplified considerably. This is also reflected in Fig. 4.8: The TILDA PXI crate is now the central element controlling and receiving data from all critical units. As explained in chapter 3, TILDA assigns a time stamp to each PMT signal and the coincidence gating is completely realized in software. It can be changed during online and offline analysis. Hence gates can be optimized off-line to achieve the best signal-to-noise-ratio. The temporal structure of the bunch is always recorded and can be inspected any time. This helps to identify malfunctions or non-ideal settings of ISCOOL quickly.

4.2.6 Beam contamination and anti-proton-triggering

In order to measure the release time of nickel from the target, the ion beam was guided to a Secondary Electron Multiplier (SEM) at the COLLAPS beam line. The SEM is a particle detector, which consists of a metal plate from which impinging ions release a few electrons. These are guided towards an electron multiplier to create a detectable pulse and the observed count rate is directly proportional to the incoming ion current. Fig. 4.9a shows the results for ^{66}Ni during the first second after the proton trigger. One can see a flat line, so there is no short-time correlation to the proton impact. This matches the expectation as the chemical reactivity of nickel leads to a very slow and therefore an almost constant release from the target. Turning the resonant laser ionization from RILIS off, the count rate reduces to the dark countrate of the SEM at about 360 counts per second and it can be concluded that the ion beam consists almost exclusively of ^{66}Ni. Similar behavior was observed for all radioactive isotopes from ^{58}Ni to ^{68}Ni. Please note that stable isotopes did not require a proton pulse, but were evaporated from a designated oven. However in ^{70}Ni the release from the target became time dependent on the proton impact as one can see in Fig. 4.9b, where the SEM count rate was measured for about 40 s and included several proton pulses and for just one proton pulse in Fig. 4.9c. Here the release curve shows the typical behavior of a volatile element which is released from the target within seconds after proton impact. Also this element is not ionized by RILIS but from the hot surface in the target, because switching RILIS on / off seems to have no significant effect. In Fig. 4.9 c the yield even drops for "RILIS ON" which is only explainable because the overall yield of the target dropped over time during this acquisition and the measurement sequence was "70Ni - RILIS OFF", then "70Ni - RILIS ON 1" and finally "70Ni - RILIS ON 2". The isobaric contamination was identified as the stable ^{70}Ga isotope and the ISOLTRAP group estimated in a quick measurement campaign in a multireflection time-of-flight mass spectrometer, that per proton pulse roughly $2 \cdot 10^6$ ions of ^{70}Ga remain in the beam after HRS but only about 250 ions of ^{70}Ni. The main problem with this contamination is that gallium will also pass through the CEC chamber and will be collisionally excited or neutralized into higher lying states by the alkali vapor. Consequently, the ions or atoms leaving the CEC will emit luminescent photons while passing through the ODR. The sheer mass of gallium ions in the beam caused a huge count rate on the PMTs, impeding the spectroscopic measurement of ^{70}Ni. Another drawback of such a large contamination is that ISCOOL can only hold about 10^6 ions per accumulation. Thus, the accumulation time needs to be reduced in order to match these huge ion yields and this again leads to an increase in background since the observation time per accumulation time increases. In combination with the small yield of ^{70}Ni, the spectroscopy became unfeasible.

Luckily the time-dependent release of gallium as one can see it in Fig. 4.9b and c could be used to improve the signal-to-noise-ratio: Once the gallium is flushed from the target there is still

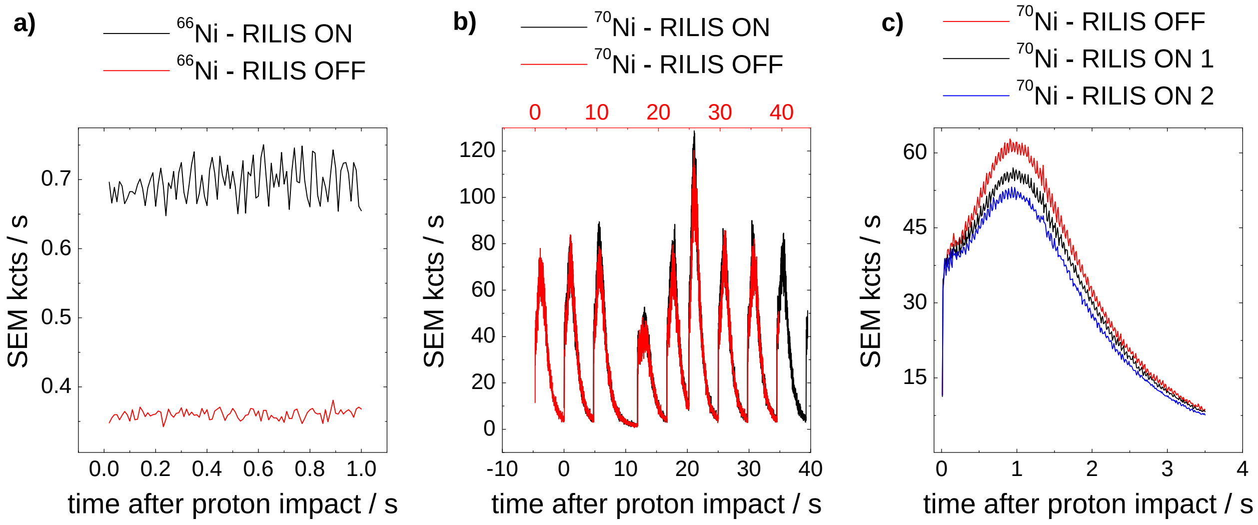

Figure 4.9.: Release curves from the target measured as a count rate of a Secondary Electron Multiplier (SEM) at the COLLAPS beam line over time after proton impact on the target. Release curve of a) ^{66}Ni during 1 s, b) ^{70}Ni during about 40 s. Note that in b) the averaged proton current per pulse was not constant, hence an increased count rate of ions from pulse 3(4) -> 5(6) was measured during "RILIS ON" ("RILIS OFF"). In order to compare both in one graph, "RILIS OFF" was shifted by one proton pulse or about 5.3 s (top-axis, red). c) ^{70}Ni for only one proton pulse, but averaged over 50 of them for each curve. Each time the ratio of resonant laser ionization ON/OFF was acquired in order to get an idea of the ratio of nickel ions to isobaric beam contamination in the beam.

a large fraction of the produced ^{70}Ni remaining, since it has a lifetime of 6.0 s. Therefore, the beam gate was closed for the first two seconds following the proton impact before opening it for 1.2 s during which ISCOOL accumulates all remaining nickel ions into one bunch which is then released to COLLAPS. During the 3.2 s after the first proton has hit the target, it had to be ensured that no further proton pulse hits the target because this would cause another production cycle of unwanted gallium and therefore the operators of the proton booster where instructed accordingly. Using this "anti-proton-triggering" a measurement of ^{70}Ni became just possible.

4.2.7 Summary setup 2016 versus setup 2017

Differences and similarities between the beam times in 2016 and 2017 have been mentioned before at the correspondent location in the experimental setup. In Tab. 4.2 these differences are summarized in order to highlight the uniqueness of each beam time and for further reference in the following chapters.

Table 4.2.: Differences between the experimental setup in 2016 and 2017.

parameter	2016	2017
target	graphite inlay	normal ISOLDE type
ion kinetic energy	$\sim$ 30 keV	$\sim$ 40 keV
ISCOOL HV divider + dig. multimeter	Ohm-Labs, KV30A, rel. prec. $1.5 \cdot 10^{-4}$ Agilent 34461A	PTB, PT50, rel. prec. $5 \cdot 10^{-5}$ Agilent 34461A
CEC HV divider + dig. multimeter	Julie Research, KV10-393 rel. prec. $1.5 \cdot 10^{-4}$ PREMA, Agilent 34461A	Julie Research, KV10-393 rel. prec. $1.5 \cdot 10^{-4}$ NI-4071, Agilent 34461A
CEC filling material	sodium	potassium
CEC heating	1.41 A, 42 V, 320°C	files #1-#81: 1 A, 28.5 V, 178°C files >#81: 0.88 A, 25.1 V, 161°C
charge exchange efficiency	45%	files #1-#81: 86% files >#81: 53%
wavemeter calibration	temp. stabilized HeNe, calibration intervals too long	diode laser locked to Rb, regular calibration intervals
data acquisition	MCP	TILDA

5 Nickel - analysis and interpretation

With the experimental techniques described in chapter 4 we were able to study the nickel isotopes $^{58-68,70}$Ni in the 2016 beam time. In 2017 we managed to measure the same isotopes again except ^{59,63}Ni, since we invested three shifts on trying to measure ^{56}Ni, which according to the measured production yields seemed to be in reach. One of the main advantages in the 2017 beam time was the application of TILDA, which gave improved control of all timings and much more information on the resonance signal since each photon event is stored instead of just recording count rates. Furthermore, an improved laser stabilization in 2017 lead to an increased accuracy.
First the foundation of the analytic methods will be introduced in the next section followed by a presentation of the results in chapter 5.2.4.

5.1 Analysis - fitting of resonances

5.1.1 Analysis with PolliFit

The analysis of the data was performed using the python-based PolliFit framework which was developed within the *Lasersphere* group and uses the python package *scipy* for fitting (see chapter 3.3.6). It is specifically designed for the needs of collinear laser spectroscopy though it is sufficiently universal to process any data format used in CLS, because it imports data from any file format to its own data type called *specdata*. The *specdata* contains all information of the scan and the acquired response from the system to the applied settings. Usually at COLLAPS the x-axis in the file is the voltage applied from the DAC and the y-axis is the number of counts of the PMTs. In the *specdata* this is then converted first to an x-axis in total volts by multiplying the DAC voltage with the multiplication factor of the bipolar amplifier Kepco BOP 500. The amplification factors were determined by repeated measurements of the amplified output using a high-voltage divider read out with a digital multimeter while ramping the DAC from -10 V to +10 V. This factor was very constant during the whole beam time and is listed in Tab. 5.1. The difference between the 2016 and the 2017 amplification factor is related to the difference in the output configuration of the used DACs. The DAC of MCP used in 2016 generates its voltage difference as a difference to the ground potential of the rack it is housed in, while TILDA's DAC used in 2017 is decoupled from the ground potential. Here the voltage is produced as a potential difference between the inner and outer conductor of the output coaxial cable. Both are connected to the input of the Kepco, but not necessarily to its chassis.

The total ion beam energy is calculated as the sum of the high-voltage at ISCOOL U_{acc}, the offset voltage at the detection region(Fluke 410B at COLLAPS) U_{offset} and the Kepco voltage $U_{\mathrm{K}} = \alpha_{\mathrm{K}} \cdot U_{\mathrm{DAC}}$.

$$eU_{\mathrm{ion}} = e\left(U_{\mathrm{acc}} + U_{\mathrm{offset}} + \alpha_{\mathrm{K}} \cdot U_{\mathrm{DAC}}\right) \qquad (5.1)$$

Table 5.1.: Weighted mean of the Kepco BOP 500 amplification factors α_K determined in 2016 and 2017. The uncertainty is determined according to Eq. (5.7).

	2016	2017
amplification factor	50.415(1)	50.3131(5)

The beam energy is then converted into velocity

$$\beta = \frac{v}{c} = \sqrt{1 - \left(\frac{mc^2}{(eU_{\text{ion}} + mc^2)}\right)^2} \tag{5.2}$$

using the mass of the respective ion taken from the latest atomic mass evaluation [Wan17]. This is finally combined with the laser frequency in the laboratory frame to generate the frequency axis for fitting

$$\nu_c = \gamma \nu_L (1 - \beta) \, . \tag{5.3}$$

Parameters that cannot be found in the single measurement files, like the Kepco multiplication factor or the voltage divider ratio are supplied in the sqlite-database that is required for each PolliFit analysis (see chapter 3.3.6). The sqlite-database is also very handy as it lists all files, analysis settings and fitting results and is therefore the central element for each analysis performed with PolliFit.

5.1.1.1 Fitting of the spectra

All spectra were fitted with the least square minimization function provided by sciPy using single and multiple Voigt-functions as discussed below. Fig. 5.1 shows a typical spectrum of ^{60}Ni from the 2016 beam time: The experimental data exhibits a clear asymmetry with a tail at lower energies at it is usual for CLS after a charge exchange cell. This is explained by elastic and inelastic collisions inside the charge exchange cell that always cause a loss in energy. A

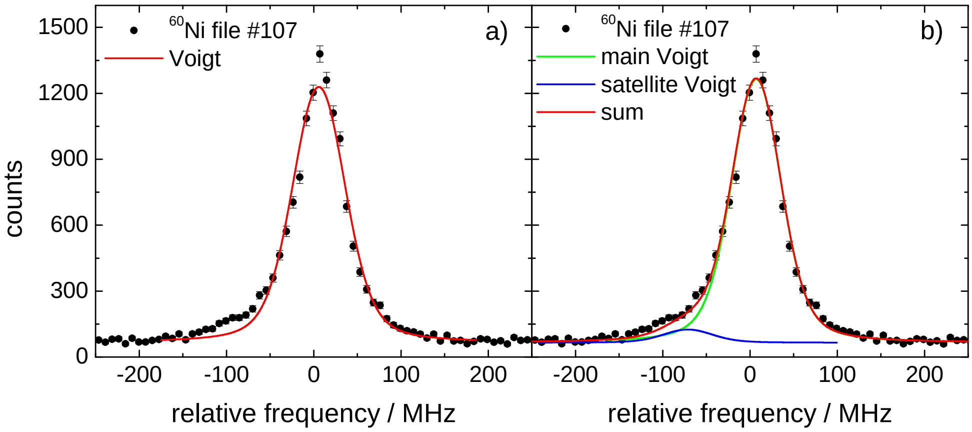

Figure 5.1.: Typical spectra of the 2016 beam time of the reference isotope ^{60}Ni fitted with a Voigt-profile (left) and a multiple Voigt-profile (right).

single Voigt can of course not accommodate for this asymmetry as is shown in Fig. 5.1a, leading to a shift of the center frequency. To improve the χ^2 of the fitting by having a better description of the line profile and to extract a more reliable center frequency of the main peak, additional Voigt profiles can be used, as shown in Fig. 5.1b. Here, a satellite-Voigt reproduces the shoulder and slightly shifts the resonance center to higher frequencies. Since the offset is associated with an energy loss, it is fitted in energy and not in frequency in order to compare this energy loss in all isotopes, independent of their individual differential Doppler-shifts. The offset between the satellite-Voigt and the main-Voigt was found by fitting all spectra of the reference isotope with this offset as one of the optimization parameters, yielding a mean value for the offset of -5.175(5) eV. This offset was now fixed for all spectra, but still the intensity of the satellite-Voigt was left free for optimization. With this line shape the fitting was performed for all isotopes by finding suitable starting parameters for all files using the *interactive fit* tool in PolliFit, followed by a *batchfit* for all files, which stores the fit results in the database for further processing and produces a plot of the fitted data for cross check.

The approach for the 2017 data was very similar, but since the data was acquired with TILDA, the temporal gates are additional parameters that need to be defined once for each isotope. This requires the isotopes time of flight from ISCOOL to the optical detection region and a suitable temporal width including all events originating from atoms of the bunch. After cross checking all spectra for their temporal length the gates could all be set to 3 μs, which is less than a third of the 10 μs wide hard-wired gates for the coincidence detection used in 2016 and further reduces the background. Once the gates were set, fitting was performed with the projections of the count rate onto the voltage axis, analog to the 2016 data set.

Two spectra are shown in Fig. 5.2, which are distinctively different: The reason for this is a high temperature of the charge exchange cell in the first part of the 2017 beam time (up to file #81). Here, the temperature and therefore the pressure in the CEC was chosen too high causing a strong asymmetric line-profile as shown in Fig. 5.2a. In this case a total of five satellite-Voigts was chosen to account for the strong asymmetry. Adding more had no observable effect on the main center position anymore. All satellite-Voigts have the same widths as the main peak and their distances are equal. The amplitudes of the satellite-Voigts were reduced by half of their neighboring satellite, leaving only one parameter for their amplitude. The optimal offset in en-

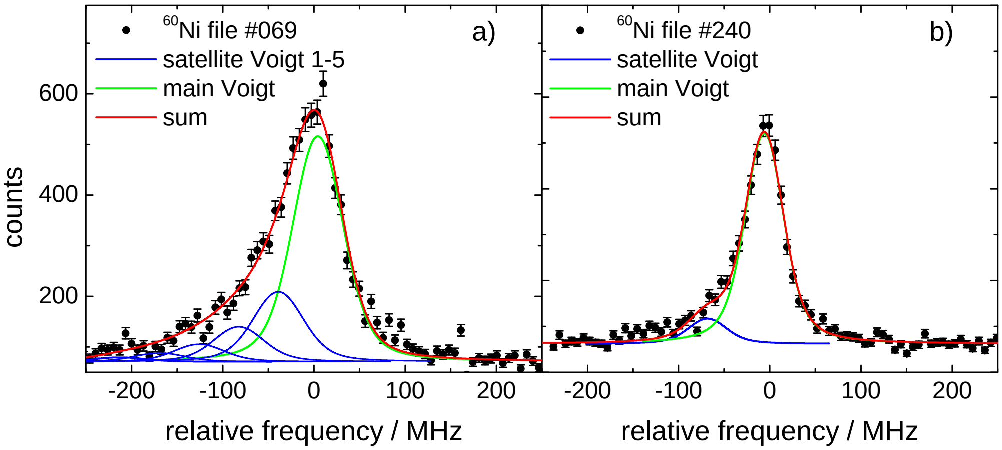

Figure 5.2.: Line shapes used in 2017, files 1-81 had to be fitted using five satellite peaks due to the high CEC temperature (left), files 82-314 were acquired with a lower CEC temperature and required only one satellite peak to account for the asymmetry (right).

ergy between the peaks was found to be -3.32(5) eV by fitting all reference isotopes from files number 1-81 and was then fixed to that value, while the second fit parameter was left free to adjust the amplitude of the peaks.

After file #81 the cell temperature was lowered and therefore the asymmetry reduced to a slight shoulder, similar to 2016. This can be seen clearly in Fig. 5.2b, which shows a typical spectrum of the reference isotope ^{60}Ni. Here, peaks were again fitted with a single satellite-Voigt which was fixed at a distance of -4.76(5) eV to the main peak.

Even-mass isotopes of Ni exhibit a single peak, while odd-mass isotopes exhibit a multitude of hyperfine transitions. For each of these lines, the same line-shape functions as for the even-mass isotopes was used. Fitting of the hyperfine manifold was performed by varying the hyperfine $A_{l,u}$, $B_{l,u}$ parameters of the lower and the upper state of the transition and the center of gravity ν_{cg} of the hyperfine splitting and the line intensities until the spetrum is well reproduced and the χ^2 minimization was successful. The relative peak intensities are calculated from the theoretical Racah coefficients, but left as a free parameter during fitting since the ratio might be affected by optical pumping and quantum interference. Only in spectra with low statistics the relative intensities were kept constant as discussed in the relevant cases below. The systematic uncertainty of the A- and B-factor is dominated by the uncertainty in the voltage measurement and can therefore be calculated analog to Eq. (5.8). Since all hyperfine structure components are within the voltage range of the Kepco, the relative uncertainty is given by the uncertainty of its amplification factor. Therefore the systematic uncertainty is smaller than the uncertainty from the fit.

5.1.1.2 Isotope shifts

The isotope shift for each resonance was found as a difference of the isotope's center frequency to the center frequency of the reference isotope ideally at the time of acquisition. Since only one isotope can be measured at a time the measurements were performed in a pattern where each isotope measurement was accompanied by a measurement of the reference isotope before and after the isotope of interest. Thus any long term drift of the laser frequency or the acceleration high-voltage of the ions can be detected and compensated for. Fig. 5.3 shows an example for ^{58}Ni from the 2017 beam time in which the reference ^{60}Ni was measured twice, before (files #224, #225) and after (files #231, #232) the two recordings of ^{58}Ni (files #229, #230) which happened during the time represented by the blue boxes. The files #226 - #228 of ^{58}Ni are not shown since here the acquisition failed due to a wrongly set offset voltage U_{offset} at the Fluke. Missing any detailed information on the temporal behavior of the drift, a straight line is fitted to the reference center positions since it is assumed that this drift is dominantly caused by a temperature related variation of the wavemeter on which the titanium-sapphire laser is stabilized. In order to approximately account for this shift the reference frequency is calculated by the linear fit and the mid time of the file for the isotope of interest (red squares). The isotope shift is then calculated as the difference to this and the center position from the isotope of interest (blue dots).

The statistical uncertainty for each fit is taken from the PolliFit fitting routine and is then combined by error propagation with the uncertainty of the linear fit to the references and the uncertainty by the length of the file itself. This will be called σ_i in the following. All individual

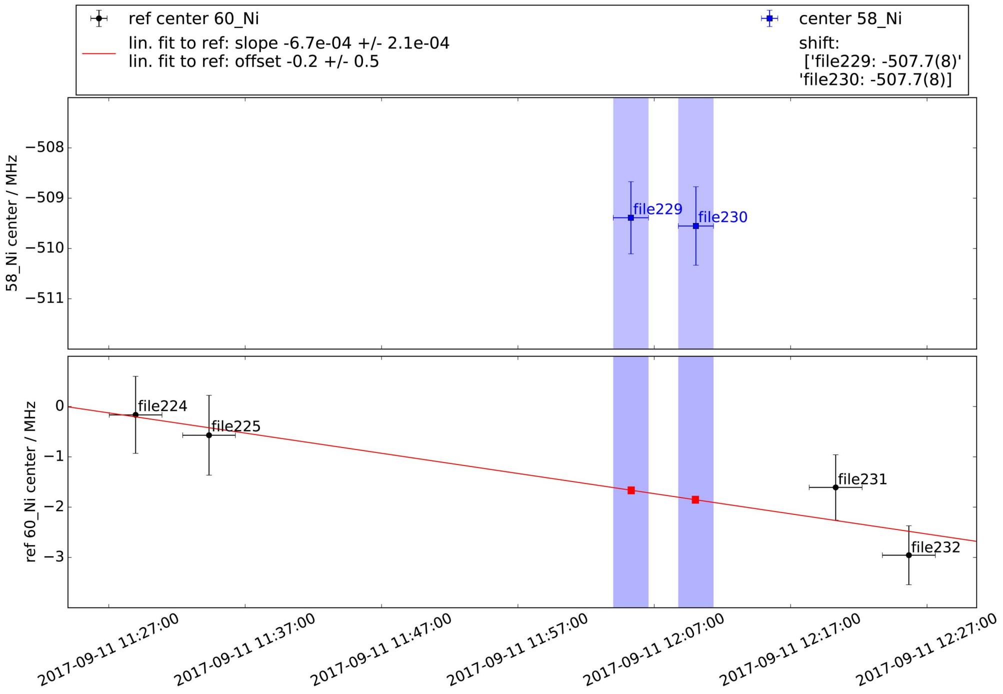

Figure 5.3.: Example for the determination of the isotope shift, here for ^{58}Ni (blue, top) surrounded by two reference measurements before and after (black, bottom) measured in the 2017 beam time. The x-axis is the mid date of the files and the x-error bars show the period of data taking for this file. Their center of gravity from the fit are depicted on the y-axis. The evolution of the reference center frequency over time is estimated by a linear fit to the reference center positions (red). The red squares indicate the reference frequency at the time of the acquired ^{58}Ni files.

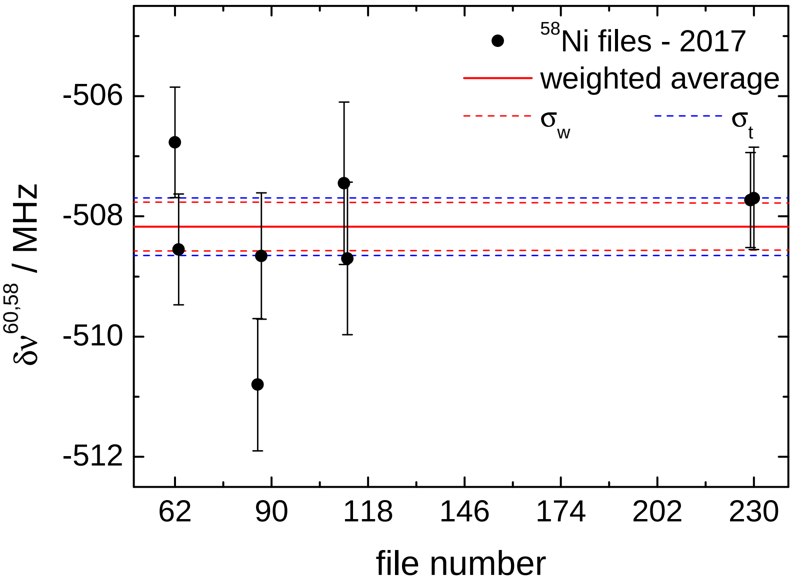

Figure 5.4.: Example for the determination of the final isotope shift of a single isotope. Here the results for ^{58}Ni in 2017 are shown. The dashed lines represent the uncertainty of the weighted average with σ_w as in Eq. (5.5) and σ_t as in Eq. (5.7). For details see text.

isotope shifts x_i will be combined to a common isotope shift by a weighted average $\bar{X}$

$$\bar{X} = \frac{\sum_{i=1}^{n} x_i w_i}{\sum_{i=1}^{n} w_i} \ . \tag{5.4}$$

with the weights w_i connected to the single isotope shift uncertainties σ_i by $w_i = 1/\sigma_i^2$. The error of this weighted average is then estimated as

$$\sigma_\mathrm{w} = \frac{1}{\sqrt{\sum_{i=1}^{n} w_i}} \ . \tag{5.5}$$

In order to better estimate the scattering of the isotope shifts, the weighted average $\bar{X}$ was used as the offset of a *linear fit to the data* with no slope and the reduced χ^2 was calculated by

$$\chi^2_\mathrm{red} = \frac{1}{(n-1)} \cdot \sum_{i=1}^{n} (x_i - \bar{X})^2 \cdot w_i \ . \tag{5.6}$$

The final statistical uncertainty is then chosen as

$$\sigma_\mathrm{t} = \max(\sigma_\mathrm{w}, \sigma_w \cdot \sqrt{\chi^2_\mathrm{red}}) \ . \tag{5.7}$$

A graphical example is plotted in Fig. 5.4 for all isotope shifts of ^{58}Ni during the 2017 beam time.

So far only the statistical uncertainties from the fit were discussed, but in determining the Doppler-shifted frequency using Eq. (5.3) the largest uncertainty arises from the ion/atom velocity. The velocity depends on the mass of the ions, the high-voltages applied for acceleration according to Eq. (5.1). The systematic uncertainty for the isotope shift $\Delta\delta\nu^{A,A'}_\mathrm{syst}$ can now be calculated as

$$\Delta\delta\nu^{A,A'}_\mathrm{syst} = \nu_L \cdot \sqrt{\frac{qU_\mathrm{acc}}{2mc^2}} \cdot (\Delta U + \Delta M) \ , \tag{5.8}$$

with the uncertainties for the mass ΔM and the voltage ΔU

$$\Delta M = \frac{\Delta m_A}{m_A} + \frac{\Delta m_{A'}}{m_{A'}} \tag{5.9}$$

$$\Delta U = \frac{1}{2}\left(\frac{U_\mathrm{offset}}{U_\mathrm{acc}} + \frac{m_{A'} - m_A}{m_A}\right) \cdot \Delta U_\mathrm{acc} + \frac{U_\mathrm{offset} \cdot \Delta U_\mathrm{offset}}{U_\mathrm{acc}} \ . \tag{5.10}$$

In this work the masses are extracted with their uncertainties $\Delta m_{A,A'}$ from the AME2016 table for masses [Wan17]. The uncertainties in the high-voltages ΔU_offset and ΔU_acc result from the uncertainties of the voltage dividers which had a relative uncertainty of $1.5 \cdot 10^{-4}$ in 2016, while the measurement for the high-voltage of ISCOOL improved to a relative uncertainty of $5 \cdot 10^{-5}$ in 2017 thanks to the new voltage divider from PTB.

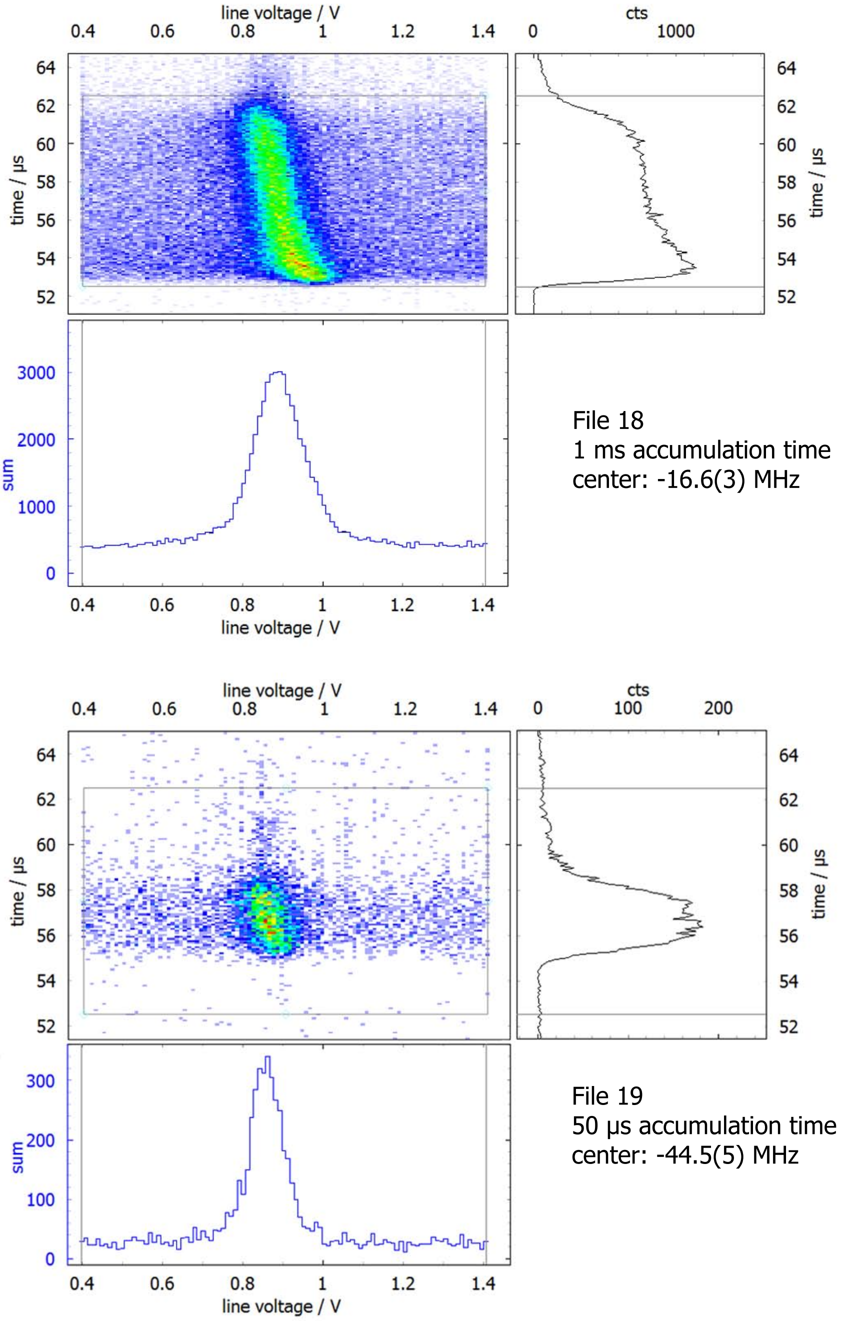

Figure 5.5.: TILDA-passive spectra of files 18 (top) and 19 (bottom) acquired in 2016. The software gates were set to 10 μs from 52.5-62.5 μs for both and in file #18 the first ions enter the detection region at about 52.5 μs, while in file #19 the first ions enter it after about 55 μs. The center of the fit on the frequency projection for both spectra shows a shift of about 28 MHz between both files although #19 was acquired immediately after #18. This indicates a correlation between the filling of ISCOOL and the center frequency.

The time-resolved DAQ offered by TILDA provides for the first time the means to systematically study cooling conditions and their influence on the line shape and center position in detail. Since the early days of ISCOOL operation, it is well known that these are affected by space-charge effects if the number of ions inside ISCOOL exceeds a certain number. Therefore it was concluded, that reference and short-lived isotope should be measured under similar conditions and with loading times that do not exhibit additional line broadening, which were the only means of recognizing unfavorable conditions using the old MCP DAQ system. This becomes especially cumbersome if the different isotopes are accompanied with largely different and even time-dependent isobaric contaminations and crucial adjustments of accumulation times have to be performed throughout the beam time as it was especially the case for the nickel isotopes. The strength of the new TILDA DAQ is demonstrated in this chapter which provides detailed information on the energy and velocity distribution inside the ion bunch. This can be used to optimize cooling conditions online, which was fully implemented in the beam time 2017 when TILDA was the main DAQ system. In the 2016 beam time with TILDA running in parasitic mode only, the acquired data could be used to identify conditions that deteriorates the accuracy of CLS in the off-line analysis. It turned out that in 2016 conditions at ISCOOL were quite unreliable and in order to make the best use of the gathered data, a quantifiable selection criterion was developed to use or dismiss the data.

As a comparison, a particularly bad example with a spectrum under reasonable conditions Fig. 5.5 depicts the measurements of ^{60}Ni from file #18 and #19, which were among the

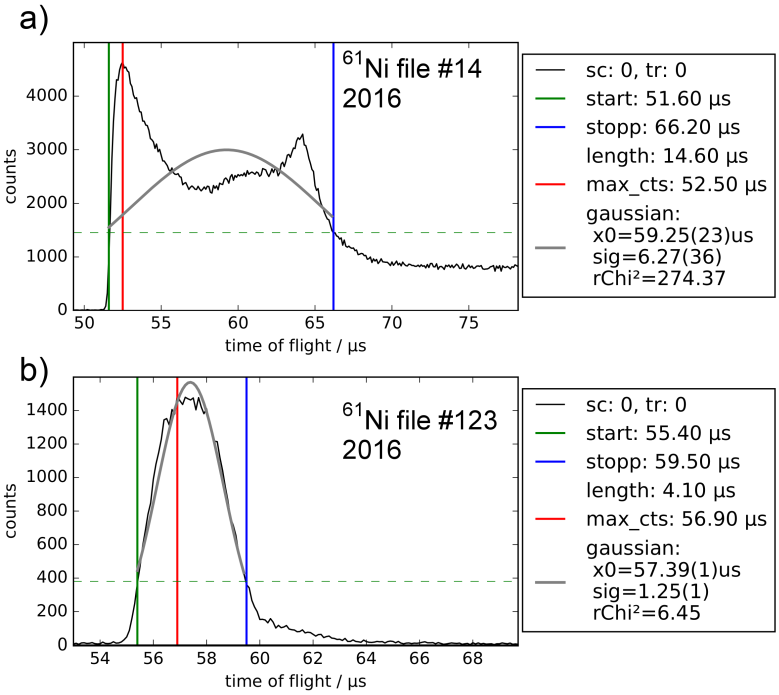

Figure 5.6.: Time structure of file #14 and file #123 for PMT *L1*. a) Shows a unfortunate example of filling too many ions into ISCOOL, while b) depicts an almost Gaussian time structure of the bunch. The horizontal dashed green line shows the threshold as 25% of the maximum counts above background. The grey line is a Gaussian fit to the full data set, shown only for the time above threshold which is used to calculate the reduced χ^2.

first bunched beam measurements early in the 2016 beam time. The accumulation time was not yet ideally adapted to the yield of nickel ions and was reduced from 1 ms in file #18 to 50 μs in file #19. A too large number of ions accumulated in ISCOOL is reflected by the temporal structure of the bunch, which is far from being Gaussian and resembles to some degree ISCOOL's DC-potential as explained in chapter 4.2.2. Ions arriving early at the detection region are faster than those arriving later, which is indicated by the shift of the resonance center from higher to lower line voltages, since the slow ions need less deceleration in order to match the resonance condition. The temporal bunch structure in file #19 with 20× reduced beam gate converges towards a Gaussian shape and the resonance position stays almost fixed within the bunch duration, but still a little skew is observed. It is obvious that the 2D-time-resolved spectra and the bunch projection (vertical direction) provide crucial information that is missing if only the projection onto the line voltage is observed as was the case with the old DAQ system. The broadening of the spectra and the accompanied shift is easily overlooked during a beam time while a look at the 2D representation immediately reveals the problem. When analyzing these two files the fit function yields a difference of the center position of about 28 MHz with the center of file #18 at -16.7(3) MHz and of file #19 at -44.5(5) MHz. Since the measurement was performed in a collinear geometry, this indicates that the mean ion velocity in file #19 was higher than in file #18. Therefore it is crucial to identify the files with a too large load in ISCOOL and exclude those in the analysis.

In order to find a quantitative decision criterion for the exclusion of a file based on the temporal bunch structure, the following procedure was established: To determine the width of the bunch, the data was binned to 100 ns steps and the width of the bunch length was determined as the time distance between the points of 25% peak height (after background subtraction). The value of 25% has been chosen to be well above the noise level to locate the points reliably even in cases with a relatively low signal-to-noise level. The peak between the two points is then fitted with a Gaussian shape, which has been found to describe the shape at low fillings reasonably well. The width determination in the first step and the reduced χ^2 of the fit is then used as a

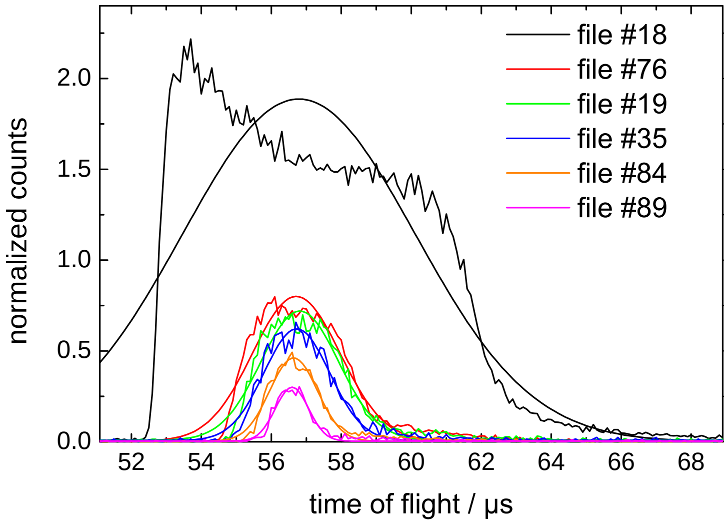

Figure 5.7.: Time projections of several ^{60}Ni files from the 2016 beam time sorted by their bunch length from top to bottom.

file	bunch length / μs	TOF / μs	red. χ^2
#18	9.4(1)	56.79(8)	62.98
#76	4.0(1)	56.71(2)	6.09
#19	3.6(1)	56.81(1)	2.97
#35	3.1(1)	56.73(1)	1.53
#84	2.3(1)	56.64(1)	4.23
#89	1.5(1)	56.59(1)	1.08

Table 5.2.: Bunch lengths determined as shown in Fig. 5.6, time of flights and reduced χ^2 from Gaussian fit.

quantification for the quality of the temporal shape. In the following, photomultiplier *L1* is used for the shape analysis. Two examples are shown in Fig. 5.6 for different fillings of ISCOOL. In a) a beam gate of 100 ms and in b) of 10 ms was chosen[1]. While the temporal structure in b) is nearly described by a Gaussian, in a) clear deviations are observed. The widths are a): 10.2 μs and b): 4.1 μs with the reduced χ^2 of a): 274 and b): 6.5 respectively. The following discussion will concentrate on the data from the 2016 beam time.

During the beam time the reference isotope ^{60}Ni was measured frequently, and exhibits a large variety of accumulated ions in ISCOOL due to varying yields and accumulation times. Some samples are presented in Fig. 5.7. The files are arranged from top to bottom with decreasing bunch length and one can see the evolution from file #18 already discussed above, with a bunch length of 9.4(1) μs and a clear non Gaussian shape to file #89 being very close to Gaussian and having a bunch length of only 1.5(1) μs and $\chi^2_{\text{red.}} = 1.08$. The corresponding results for the other files are listed in Tab. 5.2. Files #76 and #19 show a flat top profile with a steep left flank and a bunch length of about 4 μs. What influence does this have on the mean ion velocity and therefore the center frequency of the file? An indication for an increase in the mean ion velocity as it was seen in comparison between the files #18 and #19 can also be seen in the time of flight which seems to decrease somewhat along with the bunch length. But since the time of flight originates from the Gaussian fit to the data, it is unreasonable that for cases like file #18 a Gaussian fit is still appropriate and it would be more appropriate to measure the shift of the mean ion velocity directly with CLS by extracting the central frequency. But this would require stable reference positions during the complete beam time, which was not the case in 2016 and will be addressed in chapter 5.2.1.1. Files that have been acquired in close sequence, with various fillings of ISCOOL are only available for ^{61}Ni. These sequences of consecutive files will be called *block* in the following. Fig. 5.8 shows files #10, #12, #14, which were acquired within one hour in block 1 and files #120, #121, #123 within block 2 also within a similar

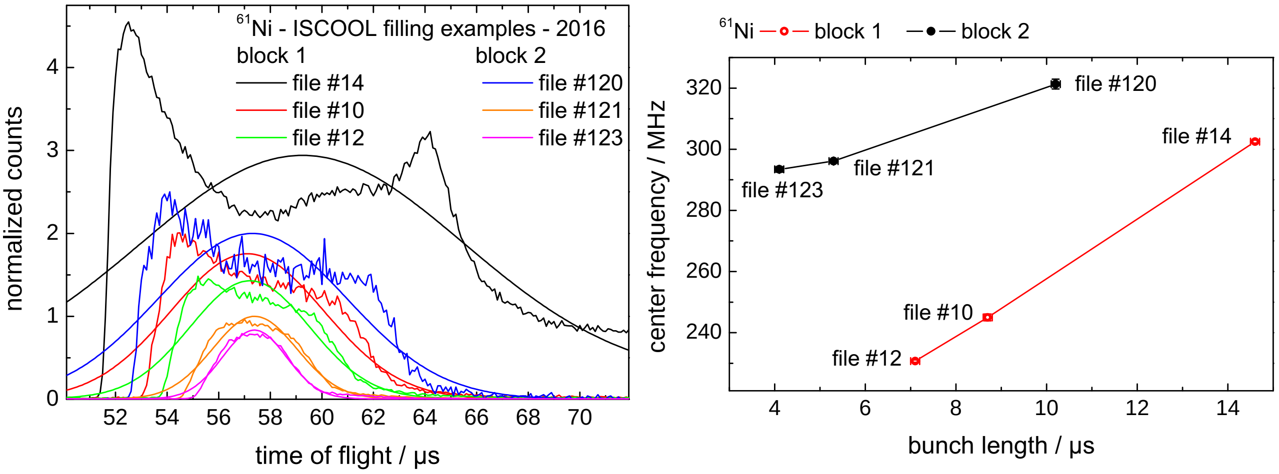

Figure 5.8.: Left: the temporal structure of the two ^{61}Ni measurement blocks each with decreasing number of ions per bunch from top to bottom. Right: bunch length versus the fitted center frequency obtained by fitting the line shapes of the respective files as described in chapter 5.1.1.1. The points of each block are connected by a line in order to guide the eye.

---

[1] Please note that the beam gate is not an absolute measure of filling, since the ion current from ISOLDE can also vary drastically.

Table 5.3.: Settings and fitting results for selected ^{61}Ni files.

file	beam gate open / ms	bunch length / μs	TOF / μs	red. χ^2	center / MHz
#14	100 ms	14.6(1)	59.25(23)	274.4	302.5(5)
#10	20 ms	8.7(1)	57.11(6)	35.4	245.0(11)
#12	10 ms	7.1(1)	57.21(4)	45.6	230.7(4)
#120	100 ms	10.2(1)	57.31(9)	8.9	321.3(16)
#121	20 ms	5.3(1)	57.40(2)	28.4	296.1(6)
#123	10 ms	4.1(1)	57.39(1)	6.5	293.4(9)

time span. The beam-gate-open period determines in combination with the production rate the number of accumulated ions per bunch in ISCOOL. Even though similar beam gates of 100 ms, 20 ms and 10 ms were used in both blocks, bunch widths and frequency shifts are different and can be extracted from Tab. 5.3. The data indicates a higher ^{61}Ni yield in block 1 than in block 2. The shape of the time-projections shown in Fig. 5.8 never comes close to being Gaussian in block 1, only in block 2 files #121 and #123 are closer to the expected shape and exhibit bunch lengths in the 5 μs range. However a $\chi^2_{\text{red.}} = 6.5$ still indicates quite some deviation from the Gaussian shape. The evolution of the center frequency in the files for each block is depicted in the right part of Fig. 5.8 and the values are included in Tab. 5.3. The offset of about 60 MHz between the two blocks results from different lock-positions of the laser frequency, which can unfortunately not exactly be quantified since an absolute laser frequency determination was not available during the beam time (see chapter 5.2.1.1). Within each block the center frequency should be constant since the files are recorded within a short period with a stabilized laser

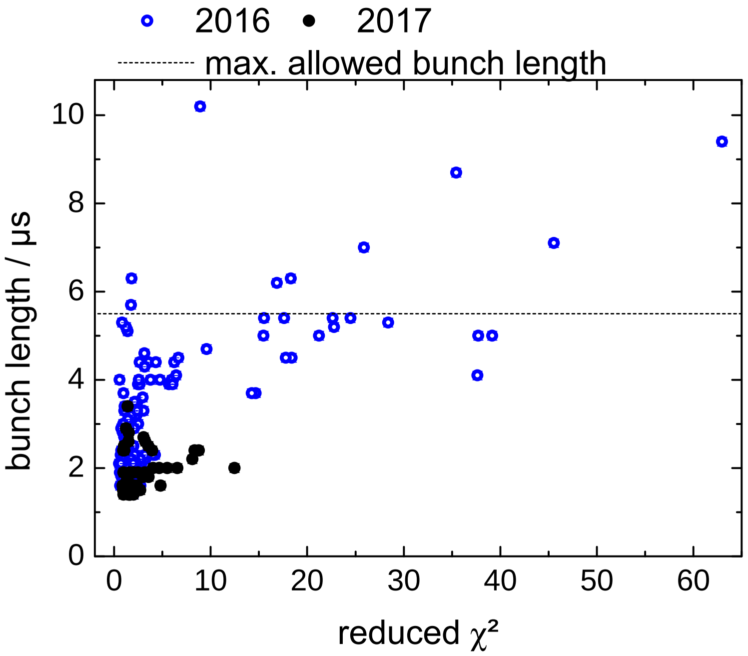

Figure 5.9.: Reduced χ^2 from a Gaussian fit to the temporal projection versus the bunch length for all files acquired in 2016 and 2017. File #14 in 2016 (see Fig. 5.8) is not depicted with a reduced χ^2 of 274.4 and a bunch length of 16.6 μs.

frequency. Nevertheless a decrease of the center frequency along with the bunch length is observed, indicating an increase in mean ion velocity of the bunch. A drastic reduction of about 70 MHz is observed in the first block for a reduction of the beam gate by an order of magnitude. Even at the lowest loading times, the bunch length has not reached the typical 5 μs length for small loads. This result is not surprising taking into account the temporal bunch profiles in the left part of Fig. 5.8, indicating the strong distortion from Gaussian shapes also represented by the huge χ^2_{red} values. In the second block, a more moderate change is observed and the temporal structure comes much closer to a Gaussian line profile for the shortest gate. Accordingly, the shift in frequency is considerably smaller with an overall shift of about 28 MHz. Once the bunch length has reached a value of 5.3 μs the shift is not critical anymore. A bunch length of less then 6 μs seems to represent cases, where the space charge influence in the cooler is not neglectable, but does not affect the center frequency so strongly that it renders the extraction of nuclear charge radii infeasible.

Finally, bunch length and χ^2_{red} are plotted for all files in both beam times in Fig. 5.9. It is striking that in 2017 all data points cluster at short bunch length and small χ^2_{red} whereas the 2016 data have a much wider distribution and large excursions in both directions, exhibiting also a clear correlation between bunch length and χ^2_{red}. Due to the aforementioned investigation, the data used for 2016 was restricted to files which have a bunch length of less than 5.5 μs as indicated by the horizontal line in Fig. 5.9. It can be expected, that the 2017 data is more reliable than the 2016 data, which will be further discussed in the following chapters.

5.2 Results

As described in chapter 4.2.7 the experimental setup differed in some crucial points between the two beam times in 2016 and 2017 and therefore each data set was analyzed separately before the results are compared and finally merged to a final set of results. The outcome of the final set of results will be discussed in chapter 6.

5.2.1 Results of the 2016 beam time

5.2.1.1 Center Frequency of the Reference Isotope 2016

The position of the center frequency of the reference isotope ^{60}Ni during the beam time is depicted in Fig. 5.10. A drift of almost 60 MHz is observed within the first two days starting with an approximately linear trend from about −45 MHz to 10 MHz. Soon after this trend reversed and at file #138 the drift of the reference center position was noticed in the online analysis and the reason for this behavior was searched for: A quick analysis of the high-voltage measurements from ISCOOL revealed, that this could not be the source of the drift. Instead, it was noticed that the regular calibration of the wavemeter onto a stabilized helium neon laser was turned off, which left the wavemeter prone to changes in temperature or pressure. Since the titanium-sapphire laser was stabilized on this wavelength meter these changes lead to the observed shift. Afterwards, the wavemeter was calibrated roughly once per hour, always between two reference isotope measurements. This clearly reduced the drift as indicated in the improved stability later on.

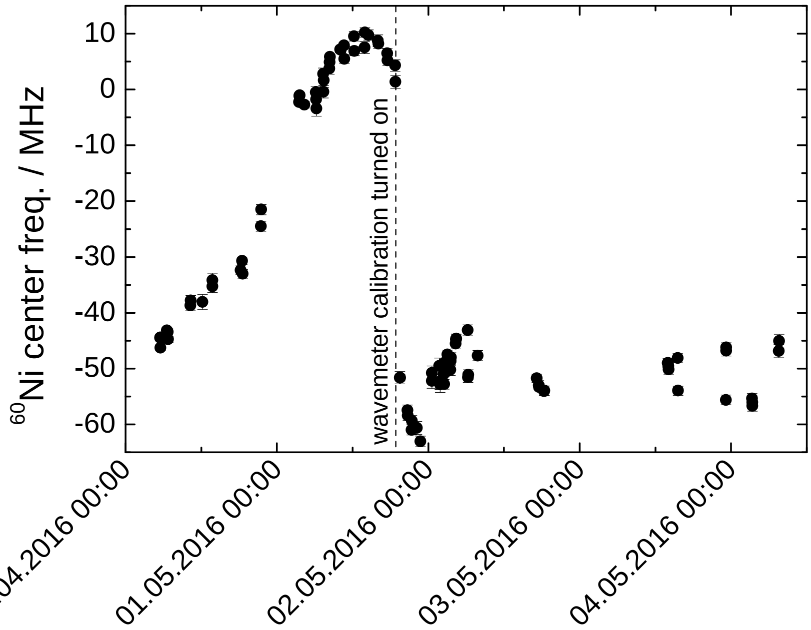

Figure 5.10.: Fit results of the reference isotope's center frequency in the 2016 beam time. file #138 marks the last file before the wavemeter was calibrated regularly on a stabilized helium neon laser.

5.2.1.2 Isotope shifts and charge radii 2016

The isotope shifts were determined as explained in chapter 5.1.1.2 and results are listed in Tab. 5.4. The linear interpolation of the reference center position, as explained in chapter 5.1.1.2, should eliminate the drift of the wavemeter to a large degree. The isotope shifts were then used to extract the change in root mean square charge radii through the King-plot procedure. This requires independently determined charge radii and those were taken for the stable isotopes from [Fri04] and are included in Tab. 5.4. They were determined from the muonic Barret radii using the V_2 factor, which is extracted from elastic electron scattering and relates the Barret radii $R_{k\alpha}$ to the mean-square charge radius according to

$$\langle r_c^2 \rangle = \frac{R_{k\alpha}}{V_2} \,. \tag{5.11}$$

Fig. 5.2.1.2 shows the King-plot as it was performed using PolliFit. Here, the linear regression procedure according to [Yor04] is used, which accounts for both, x- and y-errors. The slope provides the field shift factor F and the y-intercept the mass shift factor K

$$F = -732(85)\,\mathrm{MHz/fm^2}, \tag{5.12}$$

$$K_0 = 1243(31)\,\mathrm{GHz\,u}\,. \tag{5.13}$$

This can be compared to a different transition of the same fine-structure manifold, namely the $4s\,^3\mathrm{D}_2 \rightarrow 4p\,^3\mathrm{P}_2$ 361 nm transition, which was analyzed in [Fri04] and resulted in $F(361\,\mathrm{nm}) = -721(82)\,\mathrm{GHz/fm^2}$ and $K(361\,\mathrm{nm}) = 1215(36)\,\mathrm{GHz\,u}$. This is in good agreement with our case, where we just start from the $^3\mathrm{D}_3$ instead of the $^3\mathrm{D}_2$ level.

The correlation of -0.995 between F (*slope*) and K_0 (*intercept*) is large. It can be reduced by

Table 5.4.: Isotope shifts and charge radii obtained in the 2016 beam time.

A	$\delta\nu_{\mathrm{IS}}^{60,A}$ / MHz	$\delta\langle r_c^2\rangle^{60,A}$ / fm^2	r_c / fm [Fri04]	$\delta\langle r_c^2\rangle^{60,A}$ / fm^2 [Fri04]
58	−510.6(6) [95]	−0.278(9)	3.770(4)	−0.273(4)
59	−215.2(11)[74]	−0.185(10)		
60	0.0	0.000(4)	3.806(2)	
61	283.7(11)[42]	0.078(3)	3.818(3)	0.091(4)
62	505.5(3) [33]	0.223(4)	3.836(3)	0.229(4)
63	787.4(7) [25]	0.275(4)		
64	1029.9(4) [27]	0.365(5)	3.853(3)	0.360(4)
65	1326.6(18)[45]	0.370(12)		
66	1534.1(8) [64]	0.482(10)		
67	1797.8(7) [81]	0.508(16)		
68	1996.5(9) [99]	0.610(14)		
70	2382.6(42)[133]	0.799(13)		

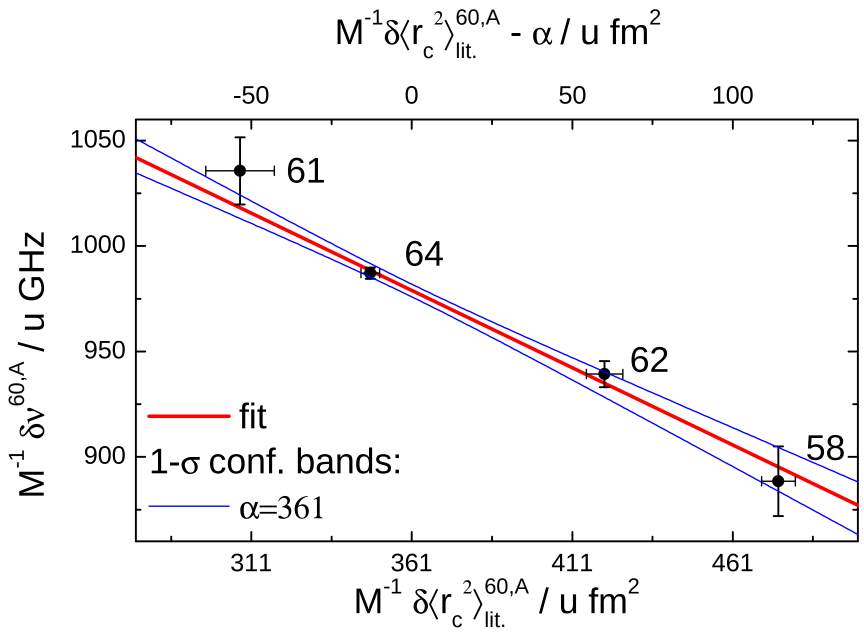

Figure 5.11.: King-plot of the measured modified isotope shifts of the stable nickel isotopes from 2016 versus the modified change in mean-square charge radii from [Fri04]. The red line is a linear fit to the data including uncertainties in x and y direction and the blue lines indicate the 1σ-confidence bands. The upper x-axis is shifted by a constant factor α=361 u fm^2 in order to minimize the correlation between slope and offset of the fit, see text for details.

shifting the origin of the x-axis into the center of the measured data points by introducing a constant offset α to all x-values modifying equation 2.69 to [Ham18]

$$\delta\nu_{\text{mod.}}^{A,A'} = \underbrace{M^{-1}\delta\nu^{A,A'}}_{y} = F\cdot\underbrace{\left(M^{-1}\cdot\delta\langle r^2\rangle_{\text{lit.}}^{A,A'} - \alpha\right)}_{x} + K_\alpha . \tag{5.14}$$

Here, the correlation is reduced to 0.05 by using $\alpha = 361$ u fm^2, which is shown as the upper x-axis in Fig. 5.2.1.2 and the new y-intercept from the fit is found to be

$$K_{361} = 979(3)\,\text{GHz}\,\text{u} . \tag{5.15}$$

Thereby the relative uncertainty of the offset was reduced by almost an order of magnitude, but does not have the physical meaning of the mass-shift anymore. The field shift factor stays unaffected from this transformation. The importance of this procedure lies in the fact that in the following procedure Gaussian error propagation can be used.
By solving Eq. (5.14) for $\delta\langle r^2\rangle^{A,A'}$, the change in rms charge radii relative to the reference isotope ^{60}Ni of an isotope with mass number A can now be calculated by

$$\delta\langle r^2\rangle^{60,A} = \frac{\delta\nu^{60,A} - M\cdot K_\alpha}{F} + M\cdot\alpha . \tag{5.16}$$

With the eliminated correlation between F and K_α the uncertainty of the change in rms charge radius can now be calculated simply by Gaussian error propagation according to

$$\Delta\delta\langle r^2\rangle^{60,A} = \left[\left(\frac{\Delta\delta\nu^{60,A}}{F}\right)^2 + \left(\Delta M \cdot \left[\alpha - \frac{K_\alpha}{F}\right]\right)^2 + \left(\frac{M \cdot \Delta K_\alpha}{F}\right)^2 + \left(\frac{\Delta F \cdot \left(\delta\nu^{60,A} - M \cdot K_\alpha\right)}{F^2}\right)^2\right]^{1/2} . \tag{5.17}$$

Here ΔK_α, ΔF are the uncertainties of the field and mass shift factor from the shifted King-plot, the uncertainty in the reduced mass ΔM as in Eq. (5.9) and $\Delta\delta\nu^{60,A}$ is the statistical uncertainty of the isotope shift. It is worth mentioning that the systematic uncertainty of the isotope shift can be neglected, since a systematic shift in the high-voltage would result in a shift similar to the mass shift and therefore it is decoupled from the field shift through the King-plot procedure and cannot influence $\Delta\delta\langle r^2\rangle$. The results are listed in Tab. 5.4.

5.2.1.3 Hyperfine parameters 2016

In 2016 the odd isotopes ^{59,61,63,65,67}Ni were measured. As described in chapter 5.1.1.1 the spectrum was fitted as a sum of all hyperfine peaks with the free parameters for the center of gravity, upper / lower A and B factor and the intensity for each of the peaks. Only the isotopes ^{59,63}Ni required to fix the relative intensities of the peaks to the Racah coefficients, all other isotopes could be fitted appropriately without this restriction. The hyperfine factors A and B could be left free except for ^{67}Ni, were the smallest peak was only acquired in file #191 and all other ^{67}Ni-files required to fix A_l/A_u to the ratio that was found in the other isotopes to make the fit converge. The obtained A and B factors for 2016 are listed in Tab. 5.5.

Table 5.5.: Hyperfine parameters $A_{l/u}$, $B_{l/u}$ found in the 2016 beam time.

A	I	A_u / MHz	A_l / MHz	B_u / MHz	B_l / MHz
59	3/2	−176.1(16)[1]	−452.7(11)[1]	−31.5(55)[1]	−56.7(68)[1]
61	3/2	−176.9(6) [1]	−454.8(4) [1]	−49.0(23)[1]	−100.6(28)[1]
63	1/2	352.3(16)[1]	904.5(11)[2]		
65	5/2	107.8(4) [1]	276.5(3) [1]	−28.4(29)[1]	−56.8(35)[1]
67	1/2	423.8(3) [1]	1088.7(6) [2]		

5.2.2 Results of the 2017 beam time

5.2.2.1 Isotope shifts 2017

In 2017 the center frequency of the reference isotope ^{60}Ni was much more stable over time since we calibrated the wavemeter at least once per hour, between two reference files as is clearly visible in Fig. 5.12a. The first files marked in red are offset by about 8 MHz from the average of the other measurements, which can be clearly ascribed to the operating conditions of the CEC. The temperature was chosen too high, which also required an adaption of the line profile. This affects the reference isotope and the radioactive isotope in the same way and cancels in the calculation of the isotope shift. In Fig. 5.12b the cancellation is demonstrated: The isotope ^{58}Ni was measured with the overheated cell (red) and later repeated with the cell under regular conditions (black). No apparent difference in the isotope shift is observed under different operating conditions.

In 2017, all isotopes as in 2016 were measured, except the odd isotopes ^{59,63}Ni, which were left out, because of lack of beam time. All isotope shifts from 2017 were merged to one final data set, which is listed in Tab. 5.6.

The King plot of this data set is shown in Fig. 5.13. Again the mass- and field shift factors were determined first without shifting the x-axis resulting in a correlation between F and K_0 of -0.995 and then with the x-axis shifted by $\alpha = 360\,\mathrm{u\,fm^2}$ reducing the correlation to only -0.093. The resulting factors are found to be in excellent agreement with the results from the 2016 data set

$$F = -715(68)\,\mathrm{MHz/fm^2} \tag{5.18}$$

$$K_0 = 1233(25)\,\mathrm{GHz\,u} \tag{5.19}$$

$$K_{360} = 975(2)\,\mathrm{GHz\,u}\,. \tag{5.20}$$

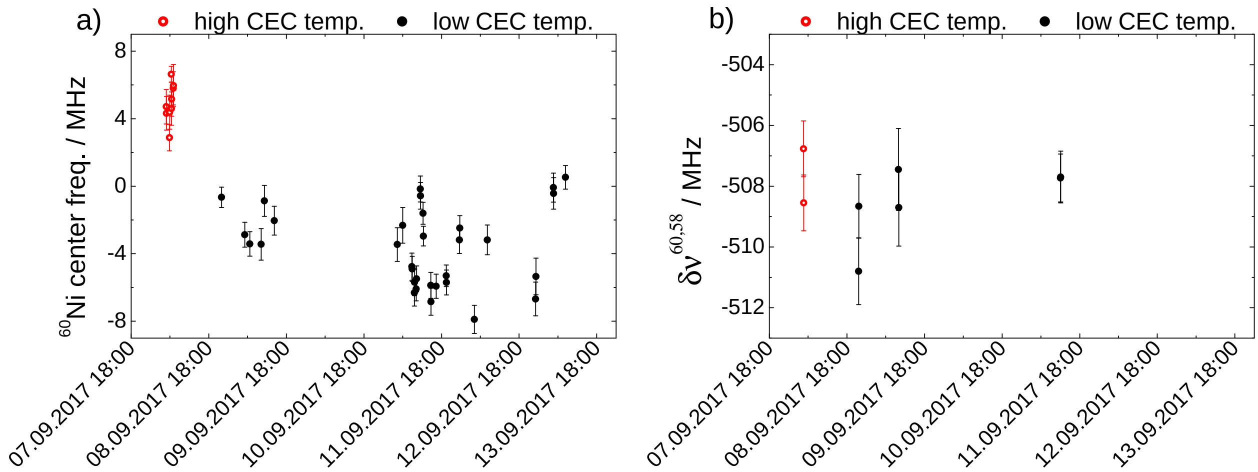

Figure 5.12.: a) Fit results of the reference isotope center frequency in the 2017 beam time. b) Isotope shifts of ^{58}Ni. The red marked files (until file #81) were recorded with the CEC at too high temperatures. Hence, a different line shape than for the data taken later was required. The isotope shift values are not affected since a similar shift in the center frequency also occurs for the radioactive isotope. This is demonstrated in b.

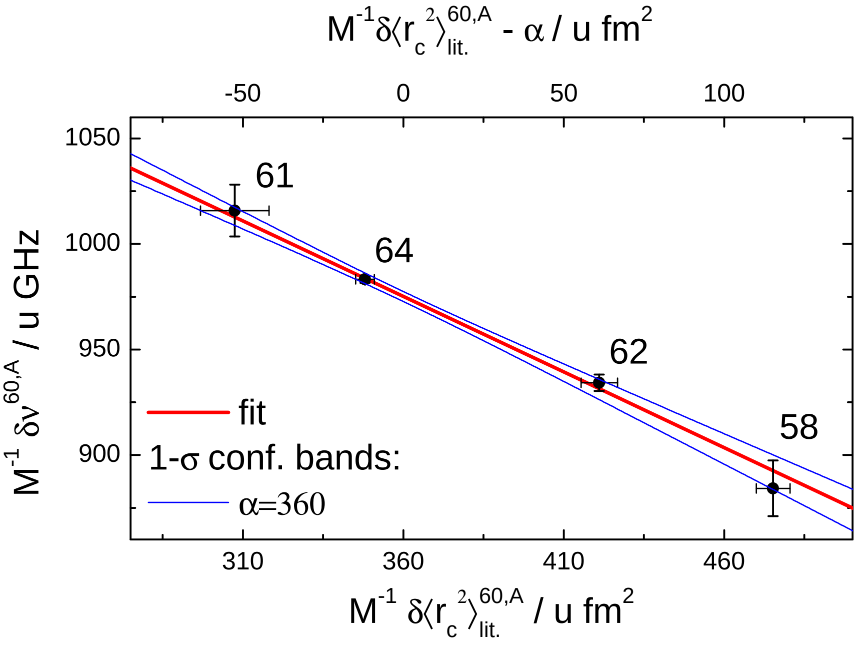

Figure 5.13.: King-plot of the measured modified isotope shifts of the stable nickel isotopes from 2017 versus the modified change in mean-square charge radius from [Fri04]. The red line is a linear fit to the data including uncertainties in x and y direction and the blue lines indicate the 1σ-confidence bands. The upper x-axis is shifted by a constant factor α=360 u fm^2 in order to minimize the correlation between slope and offset of the fit.

Table 5.6.: Isotope shifts and charge radii obtained in the 2017 beam time.

A	$\delta\nu_{IS}^{60,A}$ / MHz	$\delta\langle r_c^2\rangle^{60,A}$ / fm^2	r_c / fm [Fri04]	$\delta\langle r_c^2\rangle^{60,A}$ / fm^2 [Fri04]
58	−508.2(4) [76]	−0.280(7)	3.770(4)	−0.273(4)
60	0.0	0.0	3.806(2)	
61	278.3(10)[32]	0.083(2)	3.818(3)	0.091(4)
62	502.8(3) [21]	0.224(3)	3.836(3)	0.229(4)
64	1025.9(4) [17]	0.364(4)	3.853(3)	0.360(4)
65	1309.9(7) [32]	0.383(9)		
66	1521.3(7) [46]	0.489(7)		
67	1797.6(22)[60]	0.495(14)		
68	1990.4(9) [73]	0.604(12)		
70	2374.7(54)[100]	0.794(13)		

5.2.2.2 Hyperfine parameters 2017

The hyperfine parameters extracted from the fit of the odd isotopes ^{61,65,67}Ni, measured in 2017 are listed in Tab. 5.7. All relative intensities could be left free with a starting point from the Racah coefficients. Each ^{67}Ni spectrum in 2017 contained all three peaks even the smallest one and therefore the ratio of the hyperfine parameters could be left free. All hyperfine parameters agree within their uncertainties with the results from the 2016 beam time listed in Tab. 5.5.

Table 5.7.: Hyperfine parameters $A_{l/u}$, $B_{l/u}$ found in the 2017 beam time.

A	I	A_u / MHz	A_l / MHz	B_u / MHz	B_l / MHz
61	3/2	−177.2(4) [03]	−455.0(3) [1]	−51.5(16)[01]	−103.3(17)[02]
65	5/2	107.7(3) [02]	276.7(2) [1]	−28.9(21)[01]	−62.9(29)[01]
67	1/2	424.0(30)[1]	1088.1(21)[2]		

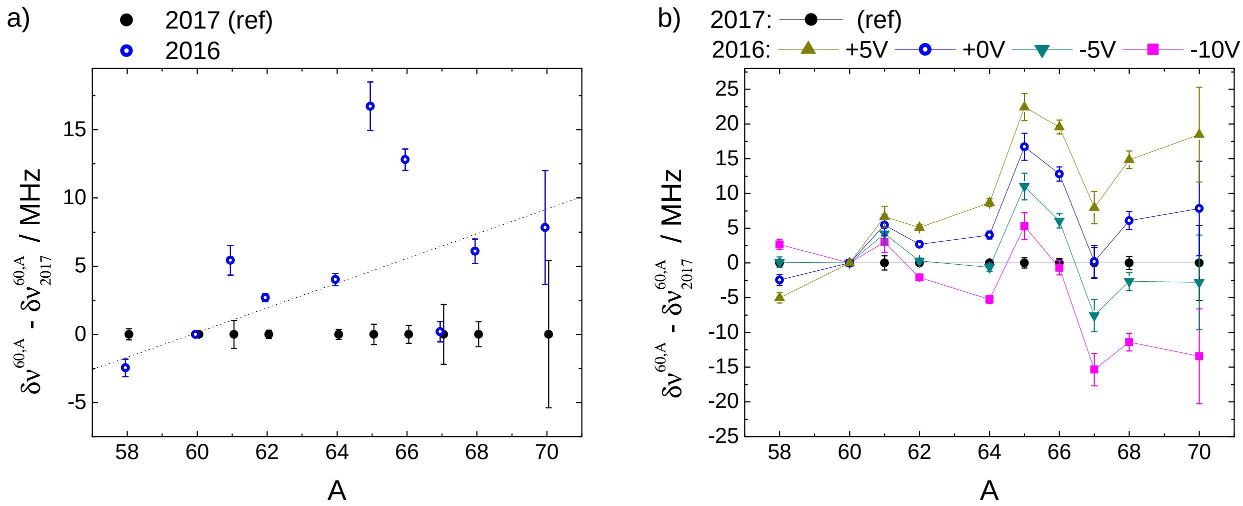

Figure 5.14.: a) Isotope shifts obtained in 2016 relative to the results from 2017 with only their statistical uncertainties. Isotopes ^{59,63}Ni were not measured in 2017 and are therefore ignored in this plot. The dotted line indicates the effect of a systematic voltage offset as discussed in the text. b) Isotope shifts of 2016 have been shifted by assumed offsets in the high-voltage in the range of -10 V to +5 V with an interval of 5 V. Each set is depicted relative to the results from 2017.

The isotope shifts extracted from both beam times are compared in Fig. 5.14a where only the statistical uncertainties are shown. Please note that ^{59,63}Ni are not included since those were measured only in 2016. A quite large scatter is visible, which is for most isotopes much larger than the statistical uncertainties. A systematic shift caused by the high-voltage uncertainty would result in a continuously increasing difference towards larger mass numbers with a crossover at the reference isotope ^{60}Ni, as indicated by the dotted line in Fig. 5.14a. While there is such a trend visible for some isotopes, others do clearly show a different behavior. Exceptionally large discrepancies are observed for ^{65,66}Ni, while ^{67}Ni is in excellent agreement in both beam times. In order to test whether a variation of the high-voltage within its uncertainty range can improve the agreement of the isotope shifts, they have been evaluated for various offsets in the range of -10 V to +5 V in steps of 5 V and the result is shown in Fig. 5.14b: The agreement can be improved in the isotopes ^{58,62,64,68,70}Ni, but the deviation in ^{65}Ni is still about 11 MHz and for ^{67}Ni the situation became worse. Hence, a systematic voltage offset alone cannot explain the observed discrepancies. Most probably, this has to be attributed to the space charge effects in ISCOOL as described before.

In order to ratify this hypothesis the investigation started with the most extreme deviation in ^{65}Ni. Fig. 5.15 shows three files for each beam time, with the ^{65}Ni file in the middle surrounded by the ^{60}Ni reference files acquired before (left) and after (right). The files in 2016 (top) are displayed with a 5 μs gate width indicated by the horizontal gray bars, while the 2017 data (bottom) is shown with a 3 μs gate. The direct comparison between 2016 and 2017 shows that the time structure of the ^{60}Ni reference files is very similar and also the ^{60}Ni-bunches in 2016 would fit within a 3 μs gate, as it was chosen in 2017. In contrast, the files for ^{65}Ni in the middle show a large difference in the time structure between 2016 and 2017: While file #93 in the 2016

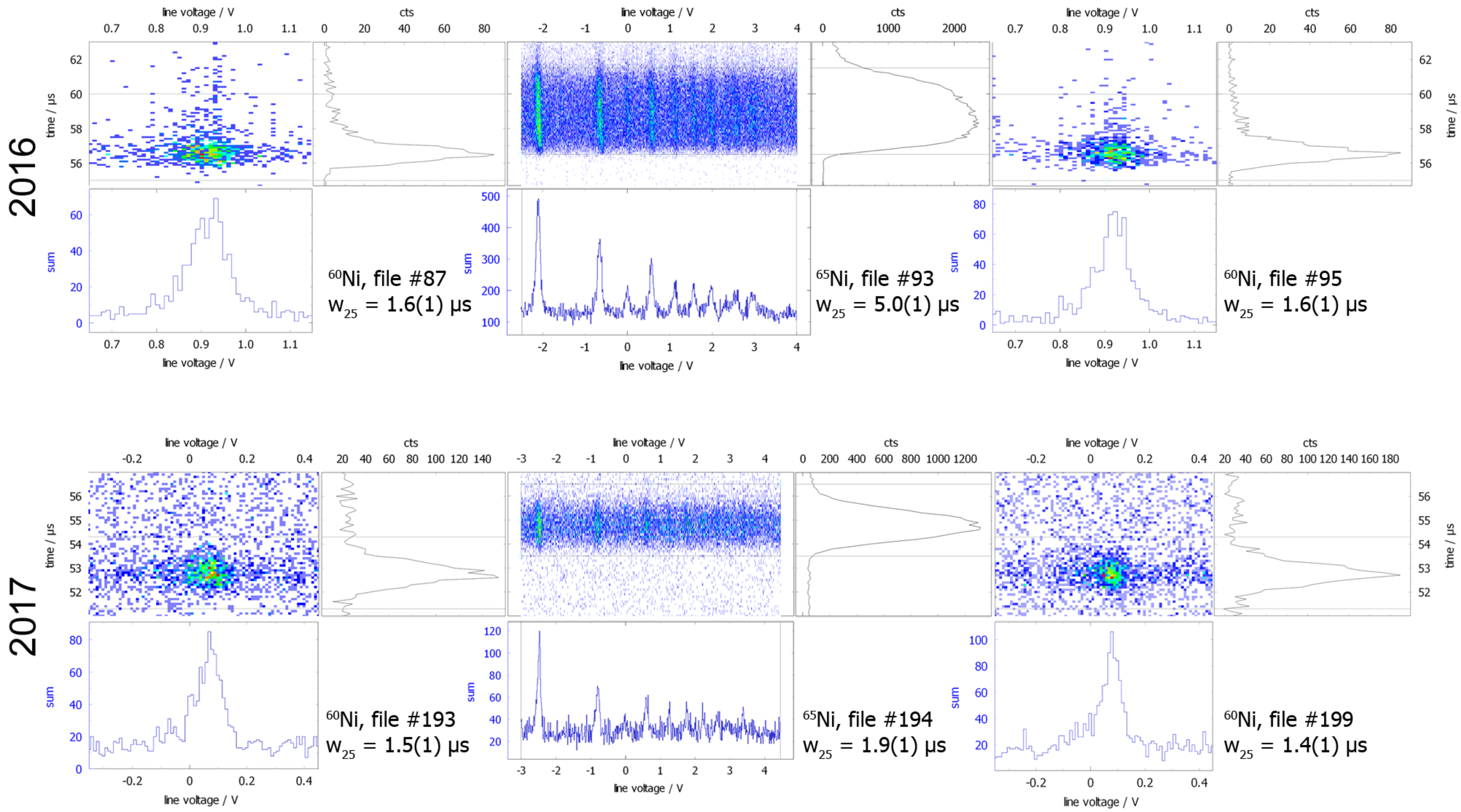

Figure 5.15.: Example spectra of ^{65}Ni (middle) surrounded by two measurements of the reference ^{60}Ni for 2016 (top) and 2017 (bottom). The software gates are set to 5 μs in 2016 (while MCP used for analysis was using 10 μs) and to 3 μs as in 2017. Differences in the time structure of the bunch between the reference file and the ^{65}Ni file cause a deviation in the extracted isotope shifts. For details, see text.

beam time (top) barely fits within a 5 μs time window and is already closer to a flat-top profile than to the Gaussian shape, file #194 in the 2017 beam time fits comfortably within a 3 μs time window and is very close to a Gaussian shape as it is the case for its surrounding reference files. Unfortunately, the ion number per bunch is unknown for all these files, but the time structure lead to the conclusion that in 2016 file #93 had many more ions within one ISCOOL-bunch than its reference files while in 2017 file #194 had roughly the same amount of ions within each bunch as the corresponding reference files.

The results of the script introduced in chapter 5.1.2 to quantify the filling of the buncher using the bunch width at 25% height w_{25} for these files are summarized also in Fig. 5.15. ^{65}Ni-bunches are in 2016 about three times longer than their ^{60}Ni reference bunches, while in 2017 they are only 30 % larger than the reference.

This analysis was performed for all available files and the absolute bunch lengths for 2016 and 2017 are shown in the appendix in Fig. A.1 for each isotope, but excluding the files showing a bunch lengths above 5.5 μs as discussed in chapter 5.1.2. Since the bunch length alone is an insufficient indicator for the possible influence onto the isotope shift, the bunch length ratio between the isotope of interest and the corresponding measurement of the reference isotope was evaluated additionally. The result are plotted in comparison with the isotope shift results from Fig. 5.14a in Fig. 5.16. Similar as with the absolute length a one-to-one correlation between discrepancy and width ratio cannot be made. However, it is obvious that those isotopes that have relatively large deviations in the isotope shift (^{65,66}Ni), but also ^{61,68}Ni, have clearly larger ratios than the other isotopes. On the other hand the cases ^{62,64}Ni show that even with similar ratios close to 1 in both beam times, considerable deviations can still occur. Please note that in

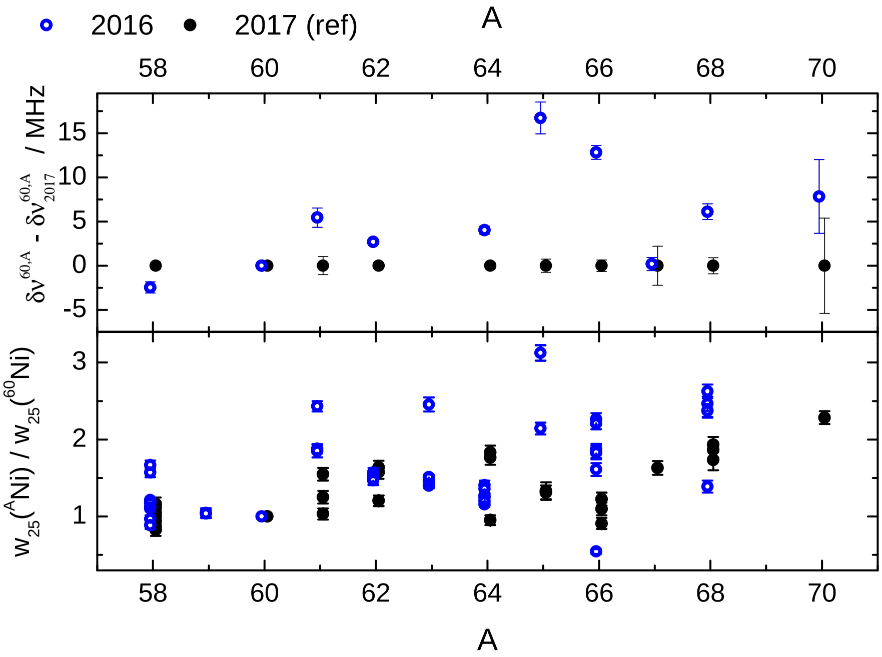

Figure 5.16.: Top: Isotope shifts relative to the results from 2017 with only their statistical uncertainties. Bottom: ratio of the bunch length for each isotope to the bunch length of the corresponding reference measurements of ^{60}Ni. Unfortunately no timing information for ^{67}Ni and ^{70}Ni could be acquired in 2016. Isotopes ^{59,63}Ni were not measured in 2017.

^{58}Ni the negative shift is in accordance with the same shift direction with too large bunches as the other isotopes. It is negative since the resonance is located at lower frequency than the reference isotope ^{60}Ni. A closer look was taken on the four isotopes with the larger deviation. For each of those, the isotope shift extracted from a file is plotted against the ratio of the widths and the absolute bunch length in Fig. 5.17. A correlation with both parameters and a drift to larger isotope shifts is visible. Especially in ^{61,65}Ni it seems that this trend continuous throughout both beam times. But this is not fully conclusive, since the results in ^{68}Ni depict a ambiguous behavior: The files #56 and #57 excluded due to their bunch length seem to fulfill this trend, but the remaining files with similar bunch length ratio and just below the w_{25} exclusion threshold, do not show this trend. The remaining files show a rather constant isotope shift independent to their bunch length ratio. With this inconclusive behavior it is impossible to find a correction factor on the isotope shifts according to the space charge effects caused by the filling of ISCOOL. One can only be advised to operate ISCOOL with a constant number of ions per bunch in order to avoid this, as it was done in the 2017 beam time.

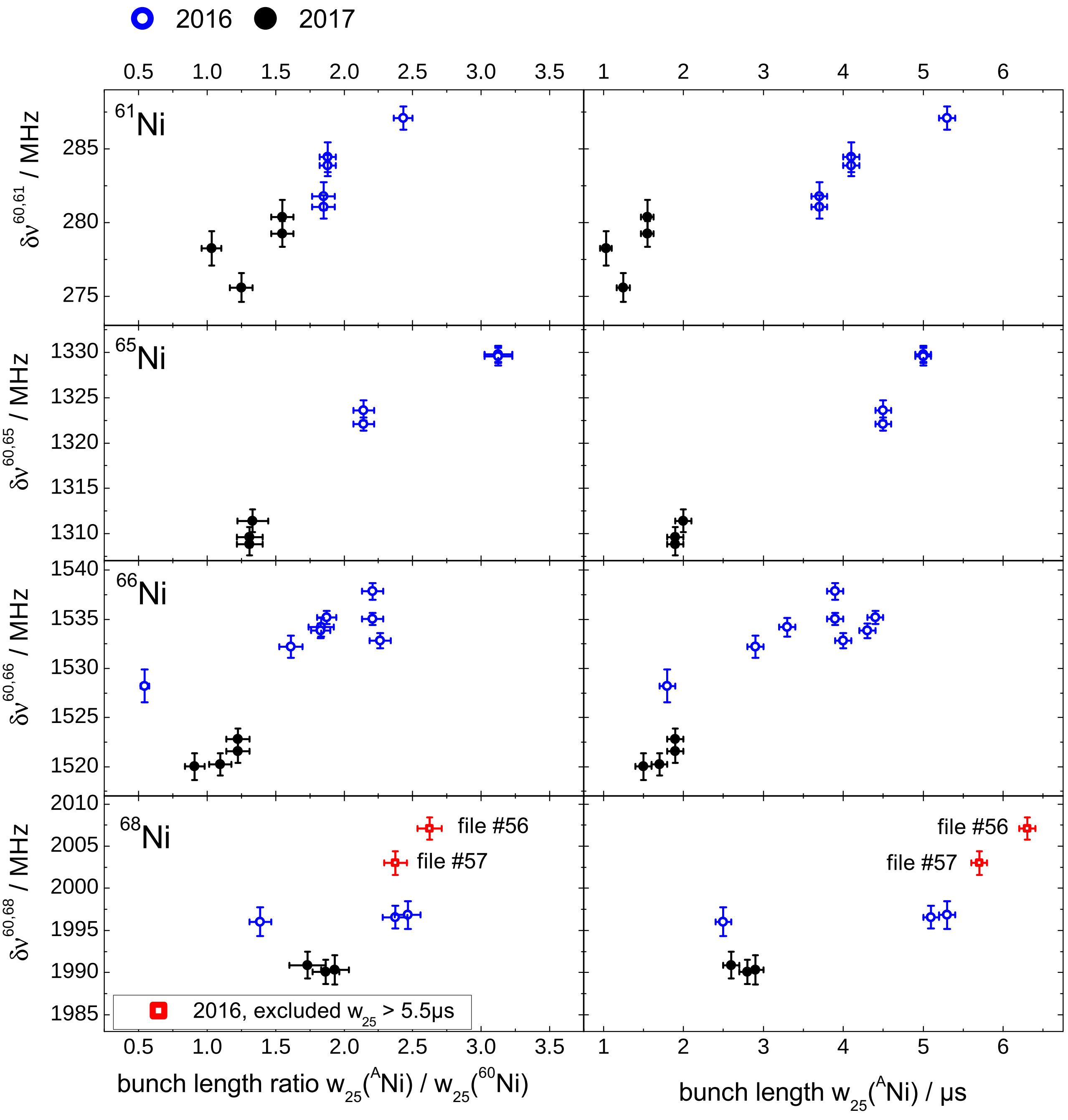

Figure 5.17.: Isotope shift of all ^{61,65,66,68}Ni files acquired in 2016 and 2017 plotted versus their bunch length ratio to their surrounding ^{60}Ni reference files (left) and versus their individual bunch length (right).

5.2.4 Combined final results

In this work the decision is made, that the unfortunate experimental situation described in chapter 5.2.3 forces the exclusion of more files than described in the chapter 5.1.2 due to an assumed overfilling of ISCOOL. Therefore in this work all dispensable files acquired in 2016 are neglected, due to the not ideal experimental conditions. Only the 2016 files relevant for the isotopes ^{59,63}Ni are retained for the final set of results, since these two were not measured in 2017.

There is still an ongoing discussion for an upcoming publication and the disagreement between 2016 and 2017 might be treated differently. Therefore, published values in the future publication might slightly disagree from the ones shown in Tab. 5.8 and Tab. 5.9. However, the final results for the charge radii and nuclear moments are not expected to change to an extent that will affect the following discussion on the nuclear physics conclusions provided in the next chapter.

Table 5.8.: Final results for the isotope shifts and charge radii. The rms charge radius r_c is calculated with $r_c(^{60}\mathrm{Ni}) = 3.806(2)$ fm from [Fri04].

A	$\delta\nu_{\mathrm{IS}}^{60,A}$ / MHz	$\delta\langle r_c^2\rangle^{60,A}$ / fm^2	r_c / fm	r_c / fm [Fri04]	$\delta\langle r_c^2\rangle^{60,A}$ / fm^2 [Fri04]
58	−508.2(4) [76]	−0.280(7)	3.769(2)	3.770(4)	−0.273(4)
$59^{\dagger}$	−215.2(11)[74]	−0.185(10)	3.782(2)		
60	0.0(0) [0]	0.000(0)	3.806(2)	3.806(2)	
61	278.3(10)[32]	0.083(2)	3.817(2)	3.818(3)	0.091(4)
62	502.8(3) [21]	0.224(3)	3.835(2)	3.836(3)	0.229(4)
$63^{\dagger}$	787.4(7) [25]	0.275(4)	3.842(2)		
64	1025.9(4) [17]	0.364(4)	3.853(2)	3.853(3)	0.360(4)
65	1309.9(7) [32]	0.383(9)	3.856(2)		
66	1521.3(7) [46]	0.489(7)	3.870(2)		
67	1797.6(22)[60]	0.495(14)	3.870(3)		
68	1990.4(9) [73]	0.604(12)	3.885(2)		
70	2374.7(54)[100]	0.794(13)	3.909(3)		

Table 5.9.: Final hyperfine parameters $A_{l/u}$, $B_{l/u}$.

A	I	A_u / MHz	A_l / MHz	B_u / MHz	B_l / MHz
$59^{\dagger}$	3/2	−176.1(16)[04]	−452.7(11)[1]	−31.5(55)[01]	−56.7(68)[01]
61	3/2	−177.2(4) [03]	−455.0(3) [08]	−51.5(16)[01]	−103.3(17)[02]
$63^{\dagger}$	1/2	351.4(9) [08]	904.2(6) [2]		
65	5/2	107.7(3) [02]	276.7(2) [05]	−28.9(21)[01]	−62.9(29)[01]
67	1/2	424.0(30)[08]	1088.1(21)[2]		

[†] Extracted from the 2016 beam time, change in ms charge radii were extracted using the King-Plot shown in Fig. 5.2.1.2.

6 Nickel - discussion

In this chapter the evolution of the charge radii along the chain of nickel isotopes is discussed and compared to the neighboring elements copper and zinc. Afterwards special attention is given to the correlation between the charge radius and the dipole polarizability in the radioactive ^{68}Ni which is a perfect test case for recent ab-initio calculations. The discussion is completed by presenting the nuclear moments identified from the observed hyperfine structure.

6.1 Charge radii

The nuclear mean-square charge radius is a fundamental property of the nucleus and it is well-known that this observable is very sensitive to nuclear shell effects, deformation and halos [Ott89; Cam16]. While the theoretical reproduction of the charge radius across the whole chart of nuclides remains challenging, experimental results keep progressing towards more and more exotic nuclei [Fri04]. They provide new insight on the nuclear structure and benchmarks for theoretical descriptions, challenging and supporting the development of theoretical approaches. Already from the first experiments using nuclear reactions [Rut11] and electron scattering experiments, it has been found that the density of nuclei is roughly constant and therefore the volume of the nucleus increases with A and the radius correspondingly with $\sqrt[3]{A}$, a fact that is already employed by the liquid-drop model and the Bethe-Weizsäcker mass formula [Wei35]. With increasing precision of the experiments it became possible to observe small deviations from this general trend and to connect these to nuclear structure effects. Particularly optical spectroscopy measurements have reached an outstanding level of precision and allow the determination of charge radii of short-lived exotic nuclei with a model independent approach. This allows to study the evolution of the charge radius of different elements far away from stability in order to find differences and similarities linked by underlying nuclear structure. Especially prominent examples are the huge odd-even staggering in the Hg isotopes that was caused by nuclear shape coexistence [Bon72; Küh77]. Another prominent example is the *kink* in the evolution of charge radii within an isotopic chain that can be observed when crossing a shell closure [Cam16; Thi81; Mül83]. Here, the differential change of the charge radius along the isotope chain changes significantly, which can be clearly seen in a plot of the charge radii versus the mass number. With the exception of $N = 20$ [Ros15] this *kink* can be observed at all major neutron shell closures. For example it has been deeply studied in lead ($Z = 82$), where the size of the nucleus increases significantly more on addition of another neutron, once the magic neutron number $N = 126$ is exceeded, as can be seen in the inset in Fig. 6.1 taken from [Gor19]. In a shell-model picture, the kink can be understood as follows: Once the magic neutron number is exceeded, neutrons will occupy a new shell with a larger radial extent and therefore due to the neutron-proton interaction, protons will follow this expansion in order to reduce the symmetry energy and the charge radius increases accordingly. Specifically in [God13], the kink was explained by the population of the $1i_{11/2}$ shell instead of the $2g_{9/2}$, leading to an increased overlap with the proton orbital wavefunction of the deeply-bound proton orbitals with the principal quantum number 1. More recent investigations in tin ($Z = 50$) have exhibited a clear kink at $N = 82$ [Gor19], as it is shown in the main part of Fig. 6.1. Similar as lead and nickel, the tin

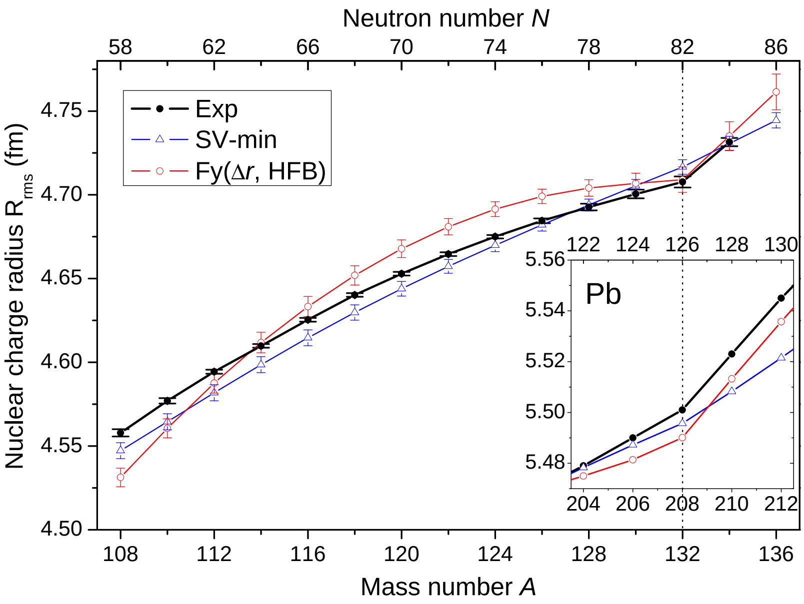

Figure 6.1.: Root-mean-square charge radii of the even Sn isotopes across the shell gap at $N = 82$ (Exp) in comparison to the nuclear density functional theories, see text. Inset: Even Pb isotopes across the magic neutron number $N = 126$. Plot taken from [Gor19].

isotopes have a closed proton shell ($Z = 50$) and provide a good test case for theory. Fig. 6.1 includes also recent results from nuclear density functional theory. Here, two parametrizations are shown, namely the SV-min, which is based on the well established Skyrme functional and the Fayans functional, which includes additional pairing and surface density-gradient terms and was recently optimized using charge radii results from the calcium chain [Rei17; Mil19]. Analysis of the Pb and Sn cases lead to the conclusion, that the reduction in pairing, which is found at magic neutron numbers, is the main mechanism to produce this kink in lead and tin [Gor19]: In this description, the nucleus is very compact at the magic neutron number, since excitations across the shell gap are suppressed leading to a minimum in wavefunction admixtures, hence a minimum in correlations and deformations. In between the shell closures correlations and deformations increase, resulting in an increased charge radius towards mid-shell, which can be seen as a parabolic trend on top of the smooth trend from the droplet model. On top of this trend the odd-even staggering can be observed, as a *zig-zag* pattern in the charge radius versus the neutron number, were the odd-neutron number nuclei usually have a smaller charge radius than the average of their even-neutron number neighbors would suggest. Note, that odd-N isotopes are not shown in Fig. 6.1, but it can be observed along the isotopic chains of Zn, Cu and Ni in Fig. 6.2 and will be discussed below. In odd-neutron number nuclei the unpaired valence neutron blocks certain states, due to the Pauli-principle, leading to a reduction in correlations, hence a reduced charge radius.

Fig. 6.2 shows the change of the ms charge radius relative to ^{60}Ni for the nickel isotopes as extracted from our data. These values are listed in Tab. 5.8. The trend in charge radii for the neighboring elements copper ($Z = 29$) [Bis16] and zinc ($Z = 30$) [Xie18] are depicted with an offset relative to nickel. This offset is chosen as a typical value in this area of the nuclear chart and is not of further interest. All three elements were combined in one plot to highlight similarities and differences in the trend of the radii: One can clearly see that all three chains show a parabolic trend on top of a linear trend between the shell closures at $N = 28$ and $N = 50$.

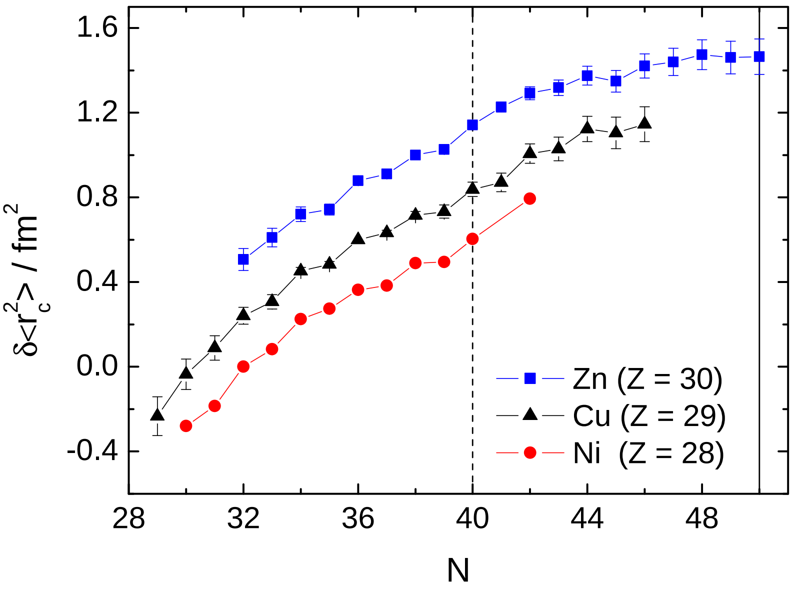

Figure 6.2.: Change in mean-square charge radii relative to ^{60}Ni versus the neutron number N. Change in ms charge radii from Cu [Bis16] and Zn [Xie18] are plotted with an offset in $\delta\langle r_c^2\rangle$ in order to compare the trends with Ni. At $N = 40$ the dashed line indicates the neutron sub-shell closure and the solid line depicts the neutron shell closure at $N = 50$.

The neutron number $N = 40$ is indicated by a dashed line. The usual odd-even staggering is clearly visible. A noticeable exception is the ^{71}Zn which shows an inverted odd-even staggering at $N = 41$. Similar inversions are found in this region for heavier elements [Kei95; Lie96] and were explained by core polarization caused by the single unpaired nucleon. This is discussed in more detail in [Kei95; Lie96; Bis16].

6.1.1 Charge radii across $N = 40$

The $N = 40$ sub-shell closure has become a topic of large interest recently, since it has been shown that ^{68}Ni exhibits features of a doubly magic nucleus: A relatively high lying $I^\pi = 2^+$ state [Bro95] and the low $B(E2)$ transition rate [Sor02] are such indications. A theoretical analysis of ^{68}Ni has argued that these features are not caused by a magic neutron number, but by the parity change between the pf orbitals ($N = 28-40$) to the $g_{9/2}$ orbital above $N = 40$ [Lan03]. Furthermore, high-precision mass measurements, which are also very sensitive to nuclear shell gaps, could only show a very weak sub-shell closure disappearing quickly when increasing the number of protons [Rah07; Gue07]. Laser spectroscopic measurements came to similar findings in the charge radii of copper ($Z = 29$) and gallium ($Z = 31$) [Bis16], where a weak effect of a sub-shell closure has been observed in copper but not in gallium. In order to highlight the effect around the sub-shell closure, it is useful to subtract the charge radius calculated from the droplet model for a spherical nucleus, according to Eq. (2.6) from the experimental results. The results are shown in Fig. 6.3, with the odd-neutron numbers (hollow symbols) drawn separately from the even-neutron numbers (full symbols) for each element accentuating the odd-even staggering in this region and its inversion at ^{71}Zn as discussed above. The expected parabolic trend between the shell closures is clearly visible for all three elements, but at $N = 40$ it is

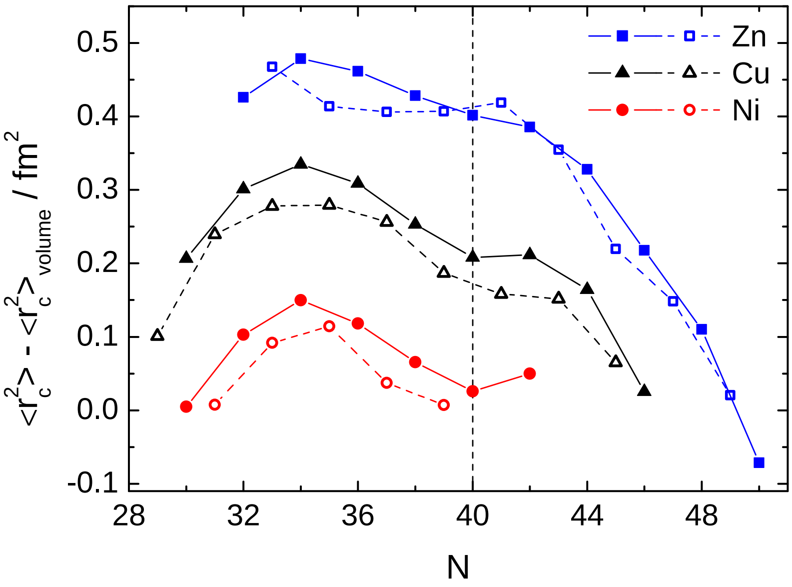

Figure 6.3.: Mean-square charge radii of Ni, Cu, and Zn relative to the radius of the droplet model. Even (full symbols) and odd (open symbols) neutron numbers are drawn separately.

disturbed by a local minimum in copper and nickel, whereas in zinc such a minimum is not visible. Hence, the charge radii support the hypothesis, that a weak sub-shell closure exists for Ni and even weaker for Cu, but disappears rather quickly away from the proton-shell closure.
In order to quantify the odd-even staggering and the strength of the kink around the sub-shell closure, it is useful to calculate the three-point indicator of the charge radius, as it is defined, e.g., in [Gor19]

$$\Delta_{kn}^{(3)} r(Z,N) = \frac{1}{2} \cdot [r(Z,N+k) - 2r(Z,N) + r(Z,N-k)] \ . \qquad (6.1)$$

In order to obtain the *strength* of the kink, we use $k = 2$, while $k = 1$ will be used to gain knowledge of the odd-even staggering. Fig. 6.4a shows the experimental results for the even isotopes in Zn, Cu and Ni in the neutron number range from $N = 32$ to $N = 40$. One can see nicely the degrading of the kink strength at the sub-shell closure, by introducing protons into the $\nu 2p_{3/2}$ shell, by comparing the three elements at $N = 40$. Ni shows a three-point indicator of $\Delta_{2n}^{(3)} r(28,40) = 0.0048$ fm, which is reduced to $\Delta_{2n}^{(3)} r(29,40) = 0.0029$ fm in copper and further reduced to $\Delta_{2n}^{(3)} r(30,40) = 0.0005$ fm in zinc. Filling three protons into the $\nu 2p_{3/2}$ shell, reduces the *kink-strength* by an order of magnitude and it seems to completely remove the sub-shell gap. Still the kink in nickel is rather small compared to a doubly magic shell gap, like in Sn with $\Delta_{2n}^{(3)} r(50,82) = 0.0083$ fm [Gor19].
Nickel shows a normal odd-even staggering and in order to quantify the magnitude of the odd-even staggering the three-point-indicator $\Delta_{1n}^{(3)} r(28,N)$ was calculated. The results for Zn, Cu and Nickel are shown in Fig. 6.4b for the neutron numbers from $N = 31$ to $N = 39$. This range is dictated by the fact that ^{69}Ni ($N = 41$) could not be measured. Odd neutron numbers show a positive $\Delta_{1n}^{(3)} r(28,N)$, as it is expected in a normal odd-even staggering. It is interesting to note that for Ni isotopes the trend seems to be opposite compared to Zn and Cu: While the later

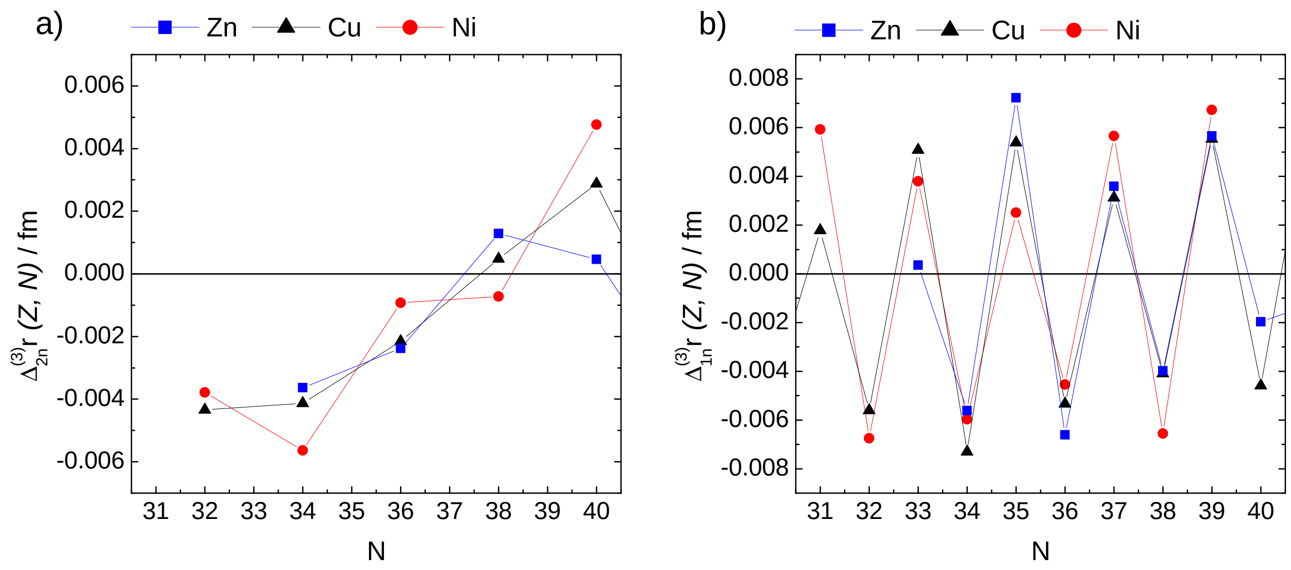

Figure 6.4.: Three-point indicator calculated according to Eq. (6.1) for the experimentally determined radii of Zn, Cu and Ni. a) $k = 2$ for the even-neutron isotopes in the range of $N = 32 - 40$ in order to quantify the kink at sub-shell closure. b) $k = 1$ in order to highlight the odd-even staggering.

exhibits the largest staggering at about the middle of the pf sub-shell, it is smallest there for Ni and increases towards the shell-closures. However, there is still too little known about the odd-even staggering to draw definite conclusions from this observation.

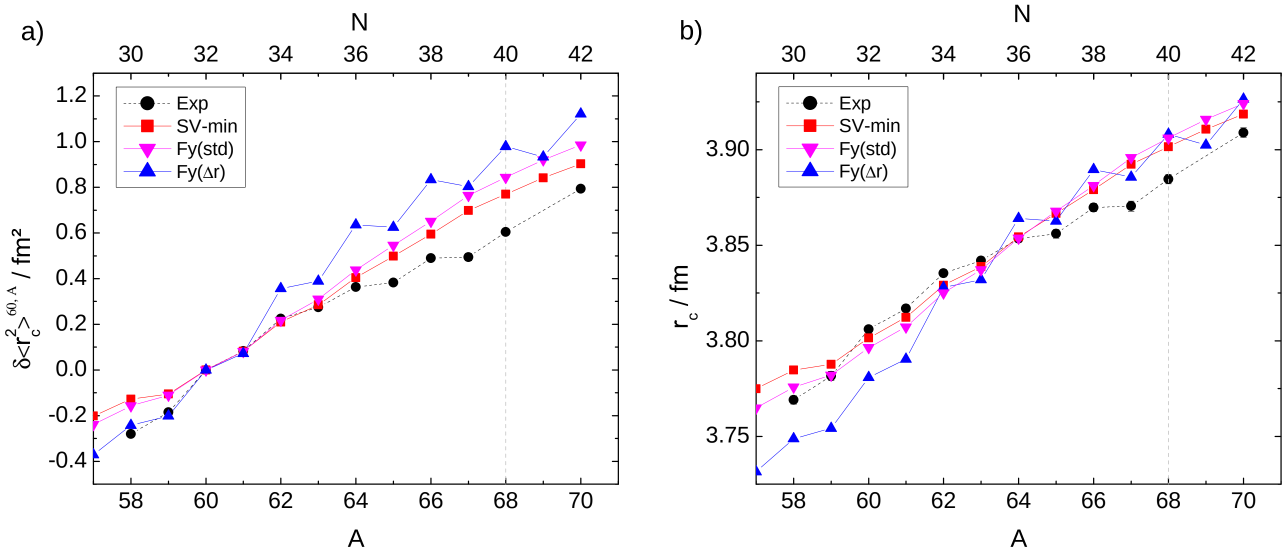

Figure 6.5.: Left: Experimental changes in ms charge radii relative to ^{60}Ni, compared to the results of selected nuclear density functionals. Right: Similar comparison for rms charge radii of the Ni isotopes.

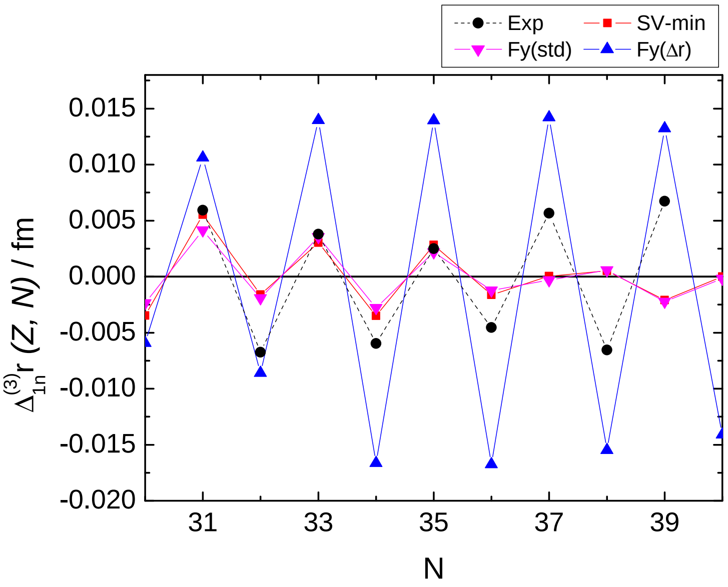

Figure 6.6.: Three-point indicator $\Delta^{(3)}_{kn}r$ of the rms charge radius for the nickel isotopes, with $k = 1$ to highlight the odd-even staggering in comparison to nDFT calculations

6.1.2 Comparison to nuclear density functional theory

Recently nuclear Density Functional Theory (nDFT) calculations [Rei19], which performed so well in calcium, tin and lead were performed also for nickel. The resulting charge radii are plotted together with the experimental results in Fig. 6.5, with the mean-square charge radii relative to ^{60}Ni on the left and the root-mean-square charge radii on the right. The shown parametrizations are SV-min, based on the well-established Skyrme functional and the Fayans parametrization with two different set of parameters. In the standard Fayans parameter set Fy(std), the additional gradient terms characterizing this potential seems not to be activated and it behaves rather like the SV-min parametrization. Only in the Fy(Δr) parameter set, which has been optimized on the steep rise of the charge radii across ^{48}Ca towards ^{52}Ca, these gradient terms seem to be activated. This results in a large odd-even staggering and an enhanced parabolic trend between the shell closures, as it has also been seen in tin, lead and calcium.
Comparing the result with the experimental data shows that the relative trend is not very well reproduced: The Fy(Δr) matches the trend in between $A = 58 - 61$, but then overestimates the charge radius in the following isotopes. Also the odd-even staggering is over-expressed as it is typical for this functional. The SV-min and Fy(std) parametrizations match the experimental results between $A = 60 - 63$, but exhibit a mostly linear increase, not following the experimental slightly parabolic trend. All parametrizations do not exhibit a sign of the sub-shell closure at ^{68}Ni. This can be quantified using the two-neutron three-point difference $\Delta^{(3)}_{2n}$, which is zero ($\simeq$ 0.0001 fm) for Fy(Δr) and slightly negative for SV-min and Fy(std). But some caution is required here since the uncertainties of the theoretical values caused by ground-state correlations are rather large. Calculations of these correlations are rather sophisticated and first test have shown that the uncertainties are at least comparable to the observed differences [Rei19]. However, all parametrizations reproduce roughly the nuclear size in the region from ^{62}Ni to ^{66}Ni. All parametrizations match the normal behavior in the odd-even staggering as it was seen in the experimental data at the beginning of the neutron shell. SV-min and Fy(std) show a very

similar trend, underestimating the odd-even staggering a little bit and reducing the amplitude further towards $N = 36$ where in the following the odd-even staggering is inverted, in clear contrast to the experimental findings. The Fy(Δr) parametrization significantly overestimates the odd-even staggering, as it has been in all other cases investigated so far [Rei17; Ham18; Mil19; Gor19], but it does not invert its normal odd-even staggering behavior. The size of $\Delta_{1n}^{(3)}$ is approximately constant among the complete region with the exception of the first isotopes. In summary it can be stated that the Fy(Δr) does not describe the Ni isotopic chain as good as it is the case for the proton-magic Ca and Sn isotopes. An appreciable $N = 40$ sub-shell closure is not observable in theory. The reason for this behavior will be a topic of further exploration.

6.1.3 Charge radius and dipole polarizability of ^{68}Ni

Currently, Coupled-Cluster (CC) theory calculations in nickel, based on χEFT interactions and advertised as the *gold-standard* around shell closures are very close to being finalized and will be published soon. But already now, coupled-cluster calculations are finalized for ^{68}Ni at the $N = 40$ sub-shell closure. First calculations have been focused on this isotope since it is the only short-lived isotope for which the dipole polarizability $\alpha_D(^{68}\text{Ni})$ has been measured [Ros13] and this combined with the charge radius provides an excellent benchmark for theory.
Before discussing the results in nickel it is noteworthy to mention recent calculations in the stable, doubly-magic ^{48}Ca [Hag15]. These helped to improve the understanding of the neutron and proton distributions in nuclei, as well as their difference encapsulated in the so called neutron-skin thickness $\Delta r_{n,p} = r_n - r_p$ with the rms charge radius of the proton r_p and neutron r_n. The latter has found to be surprisingly small, with only $\Delta r_{n,p} = 0.12 - 0.15\,\text{fm}$ and just a weak correlation of the investigated interactions to the rms charge radius was found. Another outcome of the calculations was that the employed interactions have shown a strong correlation between the rms charge radius r_c and the dipole polarizability α_D. This is depicted in Fig. 6.7, with the dashed lines, as they were presented in [Hag15]. All five χEFT interactions include three-nucleon forces and are named after Entem and Machleidt [Mac11] as EM1-4 and NNLO$_{\text{sat}}$ [Eks15]. All include linearized 2 particles - 2 holes ($2p-2h$) excitations, which will be referred to as *D/D* in the following. There is a clear linear correlation between the calculated r_c and the α_D values as represented by the fitted line to the five data points. The error band of this line was chosen in order to include the full error bars of the single points. The individual error bars were chosen to be 4% on the dipole polarizability and 1% on the rms charge radius. When this was published, the experimental α_D of ^{48}Ca was still unknown. Based on the fit and the well-known charge radius of ^{48}Ca the dipole polarizability of ^{48}Ca was predicted as $\alpha_D(^{48}\text{Ca}) = 2.19 - 2.60\,\text{fm}^3$. This was found to be in good agreement with the experimental value of $\alpha_D(^{48}\text{Ca}) = 2.07(22)\,\text{fm}^3$ measured subsequently by inelastic proton scattering [Bir17]. Further higher-order coupled-cluster calculations [Mio18] in respect to [Hag15] included also linearized 3 particles - 3 holes ($3p-3h$) correlations. The results are shown by the solid lines in Fig. 6.7, for the EM3 (1.8/2.0) and NNLO$_{\text{sat}}$ interaction and will be referred to as T-1/D in the following. Here, α_D is reduced compared to the D/D calculations, by about 15% in NNLO$_{\text{sat}}$ and about 6% in EM3 (1.8/2.0). The latter interaction is *softer* than NNLO$_{\text{sat}}$, which has a rather *hard core*, meaning that the interaction between the nucleons on short distances is stronger repulsive. One should note that the charge radius is found to be completely insensitive on including $3p-3h$ correlations. With these calculations, the agreement between experiment and theory is very good and the NNLO$_{\text{sat}}$ interaction agrees with both observables.

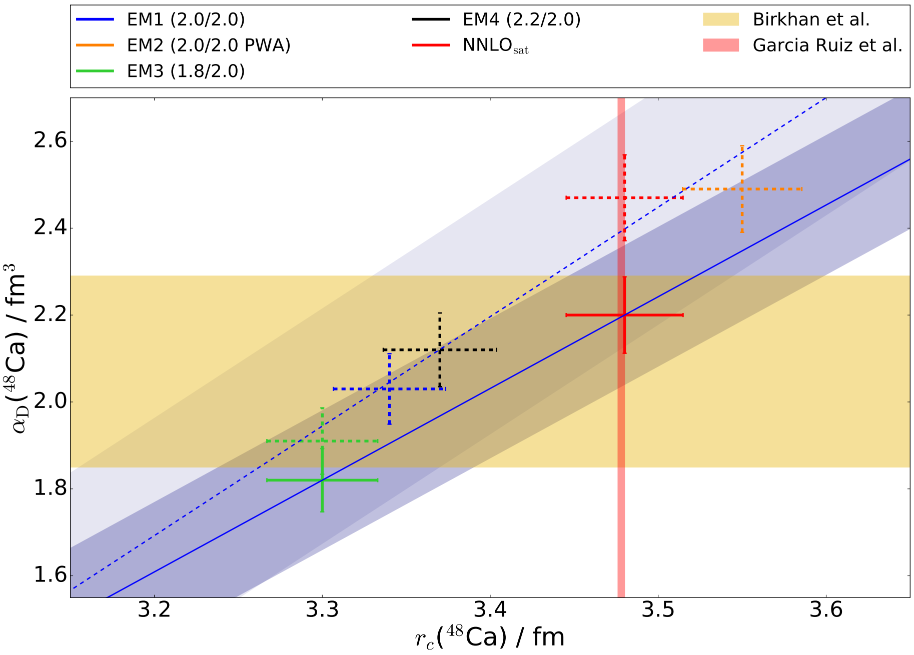

Figure 6.7.: Theoretical (data points) [Hag15] and experimental rms charge radii r_c [GR16] plotted versus the dipole polarizability α_D of ^{48}Ca [Bir17]. A straight line was fitted to the theoretical data points and is represented by the blue line accompanied by their error bands designed to fit the full error boxes of each point. Dashed lines correspond to the χEFT-interactions including $2p-2h$ interactions (*D/D*), while solid lines also include $3p-3h$ in the ground state (*T-1/D*).

With this good agreement in the stable ^{48}Ca, it was of large interest to expand this investigation to more complex nuclei, like the short-lived ^{68}Ni. In ^{68}Ni the dipole polarizability was determined from Coulomb excitations in inverse kinematics and by measuring the invariant mass in the one- and two-neutron decay channels [Ros13]. The experimental value is found to be $\alpha_D = 3.40(23)\,\mathrm{fm}^3$ with an upper limitation of 28.4 MeV. Since the experimental approach cannot measure the full energy range, the measured dipole response has to be extrapolated to cover the full energy range from zero to some upper limit, where the contribution to the dipole polarizability becomes insignificant. Therefore the experimental value was corrected accordingly to $\alpha_D = 3.88(31)\,\mathrm{fm}^3$ in [RM15]. This value is depicted in Fig. 6.8 as a horizontal yellow bar. The vertical red bar represents the rms charge radius of $r_c(^{68}\mathrm{Ni}) = 3.885(4)\,\mathrm{fm}$ from Tab. 5.8. The CC results obtained with $2p-2h$ correlations for the five χEFT-interactions are plotted with dashed lines and with solid lines for those including also $3p-3h$ correlations. In both series a harmonic oscillator frequency of $\hbar\omega = 12\,\mathrm{MeV}$ and the number of harmonic oscillator shells $N_{\mathrm{max}} = 14$ was used. The error bars for each interaction were calculated in order to include the remaining $\hbar\omega$-dependency as well as the coupled-cluster truncation error. Similar to ^{48}Ca the χEFT-interactions show a strong correlation of r_c against α_D for both, the D/D precision and the T-1/D precision. A straight line has been fitted again to the individual interactions accompanied by an error band including the full error bars. Similar as in ^{48}Ca the D/D calculations do not overlap with both experimental results and would either predict a smaller r_c or larger α_D. The T-1/D calculations seem to have a similar decreasing effect on α_D as in calcium (from 8% for the softest interaction EM3 (1.8/2.0) to 15% for the hardest interaction NNLO$_{\mathrm{sat}}$). In this case

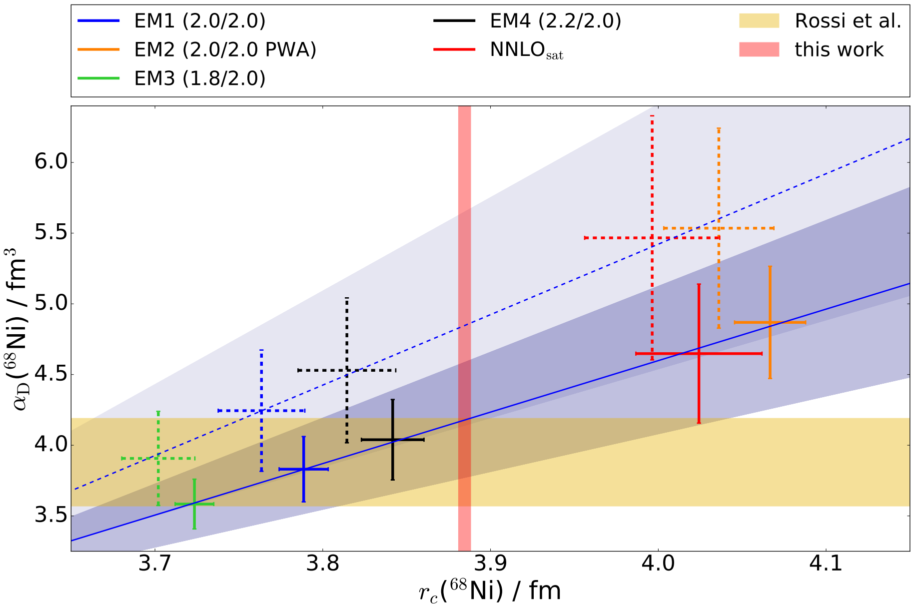

Figure 6.8.: Theoretical (data points) and experimental rms charge radii r_c and dipole polarizability α_D of ^{68}Ni [Ros13; RM15]. A straight line was fitted to the theoretical data points and is represented by the blue line accompanied by their error bands designed to fit the full error boxes of each point. Dashed lines correspond to the χEFT-interactions including 2p-2h excitations (*D/D*), while solid lines also include 3p-3h excitations in the ground state (*T-1/D*).

however r_c is notably increased (up to 0.7 % for the hardest interaction). Therefore the slope of the correlation is decreased and overlaps with both experimental values. This clearly shows the importance of the inclusion of $3p-3h$ correlations into the calculations. With this benchmark it has been shown, that state-of-the-art coupled-cluster calculations are reliable and precise also in the neutron-rich regime explored with ^{68}Ni.

6.2 Hyperfine structure

All nickel isotopes with an odd-neutron number have a nuclear spin larger than zero causing a hyperfine splitting of the atomic levels as described in chapter 2.2.1. Typical resulting spectra of these odd isotopes are shown in Fig. 6.9. The nuclear spin of each isotope can be found by counting the number of resonances in the optical spectrum. With the lower $3d^9 4s\,^3\mathrm{D}_3$ and upper $3d^9 4p\,^3\mathrm{P}_2$ levels, one will expect three peaks for $I = 1/2$, 9 peaks for $I = 3/2$ and 14 peaks for $I = 5/2$, as it is shown in Fig. 2.4. In the $I = 1/2$ isotopes ^{67,63}Ni this is rather simple and the spin identification is doubtless, because all three peaks are visible. Isotopes with higher spins can have unresolved hyperfine transitions. For example, only eight peaks are visible in the $I = 5/2$ isotopes ^{59,61}Ni, because the $F = 5/2 \rightarrow 7/2$ and the $F = 3/2 \rightarrow 3/2$ transitions are very close in energy and overlap in the spectrum. In the $I = 5/2$ isotope ^{65}Ni the spectrum shows about 12 of the expected 14 peaks. Nevertheless the spin assignment is firm, since no other spin possibilities allow a reasonable fit to the data. All spins agree with the literature values listed in Tab. 4.1. It is noteworthy, that the spins are not ordered like one would expect from filling the pf shells with neutrons according to the simplest single-particle model: One would expect that the odd neutron in ^{59}Ni is in the $p_{3/2}$ state, in the $f_{5/2}$ for ^{61,63,65}Ni and in the $p_{1/2}$ for ^{67}Ni. This irregular behavior is probably caused by the degeneracy of the $p_{3/2}$, $f_{5/2}$ and $p_{1/2}$ orbitals, as it is described for example in the GXPF1 interaction, in [Hon02]. Such a degeneracy can lead to different preferred occupations for single nucleons and pairs.

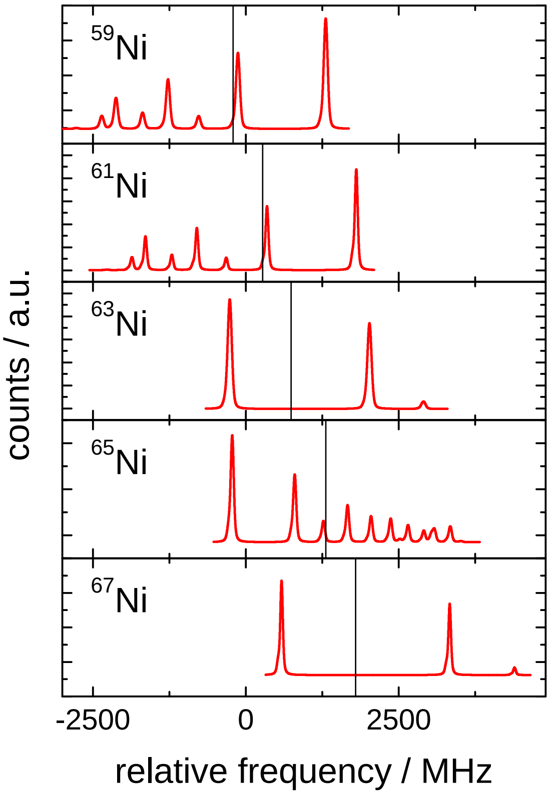

Figure 6.9.: Fitted spectra of the odd nickel isotopes measured in 2016 and 2017. The vertical black line indicates the center of gravity for each isotope. One can directly see the change in spin from $I = 3/2$ to $I = 1/2$ in ^{63}Ni, which changes again to $I = 5/2$ in ^{65}Ni and back to $I = 1/2$ in ^{67}Ni.

The hyperfine structure constants A and B for the lower $3d^9 4s\,^3\mathrm{D}_3$ and upper $3d^9 4p\,^3\mathrm{P}_2$ levels are found from the fit to the data, assuming a hyperfine level splitting according to Eq. (2.56). Please note that the quadrupole splitting vanishes ($B = 0$) for the isotopes ^{63,67}Ni due to the spin $I = 1/2$. The obtained A- and B-factors are listed in Tab. 5.9 and are compared in Tab. 6.1 with the available data for ^{61,63}Ni. Those are in excellent agreement and for ^{63}Ni the accuracy could be improved by almost two orders of magnitude compared to [Dya17]. But of course we cannot compete with the small uncertainties in ^{61}Ni measured with the Atomic Beam Magnetic Resonance (ABMR) [Chi68].

The ratio of the lower and upper A- and B-factors is found to be

$$\frac{A_{\mathrm{upper}}}{A_{\mathrm{lower}}} = 0.3894(6)\ . \tag{6.2}$$

The ratios agree within their respective uncertainties for all isotopes and provide no indication to assume an anomaly in the hyperfine structure with the achieved precision.

Table 6.1.: Hyperfine structure parameters A, B of the lower $3d^9 4s\,^3\mathrm{D}_3$ state compared to the available literature values.

A	I	A / MHz	ref.	B / MHz	ref.
61	3/2	-454.95(26)[8]	this work	-103.30(173)[2]	this work
		-454.972(3)	[Chi68]	-102.951(16)	[Chi68]
		-451(7)	[Dya17]	-106(30)	[Dya17]
63	1/2	904.19(61)[20]	this work		
		903(11)	[Dya17]		

6.2.1 Magnetic dipole moments

The magnetic moments are linked to the hyperfine structure constant A by the relation $A = g_I \mu_N B_0 / J$ (see, Eq. (2.53)). A direct extraction of the magnetic moment μ_I or the nuclear g-factor g_I would require precise knowledge of the local magnetic field B_0. However, magnetic moments of stable isotopes determined by other experimental techniques, like Nuclear Magnetic Resonance (NMR), can provide very accurate reference values to be scaled with the respective A factors and nuclear spins according to

$$\mu = A \cdot \frac{\mu_{\mathrm{ref}}}{A_{\mathrm{ref}}} \cdot \frac{I}{I_{\mathrm{ref}}}\ . \tag{6.3}$$

Care must be taken because hyperfine structure anomalies can compromise this approach, but as mentioned in the previous chapter, none were observed within the precision of this experiment.

^{61}Ni is the only odd stable isotope and this was studied by [Dra64] using NMR on liquid nickel carbonyl and after diamagnetic correction the magnetic moment is given by $\mu = -0.75002(4)\,\mu_N$ [Sto14]. The A-factor of the $3d^9 4s\,^3\mathrm{D}_3$-state in ^{61}Ni has been determined by $-454.972(3)$ MHz by [Chi68]. The results for the unstable isotopes obtained from Eq. (6.3) are listed in Tab. 6.2 and plotted versus the mass number in Fig. 6.10. They all agree with available

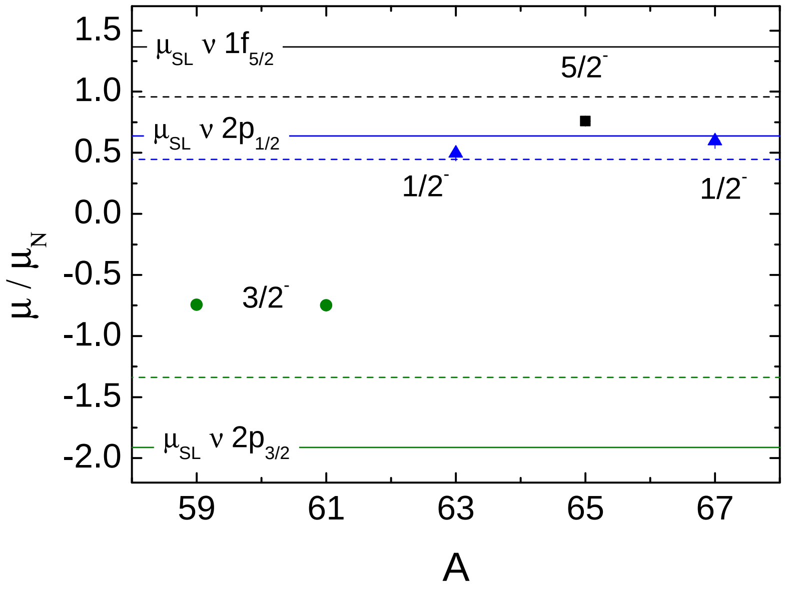

Figure 6.10.: Magnetic moments of the odd nickel isotopes, with the free (solid lines) and effective (dashed lines) Schmidt-value according to the nuclear spins $g_{s,\text{eff}} = 0.7 \cdot g_s = -2.678$ and $g_l = 0$. Error bars are smaller than the depicted symbols.

literature values but are 1-2 orders of magnitude more precise.

In the extreme single-particle shell model all Ni-isotopes with the same spin should have identical magnetic moments, the so-called Schmidt-moments according to Eq. (2.43). Experimental values (points) and Schmidt-values (lines) are depicted in Fig. 6.10, where the color indicates the nuclear spin of the respective isotope. It is obvious that isotopes with the same spin have indeed similar moments, but they are in all cases considerably smaller (in magnitude) than the Schmidt values. This so-called quenching of magnetic moments is a very common observation and is explained by two effects: Configuration mixing reduces the magnetic moment and the magnetic moment operator, as given in Eq. (2.42), already is an approximation. Since for example contributions from meson exchange currents are not taken into account. Their inclusion requires a two-body magnetic moment operator. Details on these corrections can be found for example in [Cas90] and will not be addressed further. These corrections are small for light nuclei and nuclei in the neighborhood of doubly magic nuclides. The latter are often well described by the single-particle model since excitation across shell closures are suppressed. The quenching of nuclear moments is often handled in an empirical way by introducing an effective g-factor. Typically values in the Ni region are reduced by about 30% to $g_{s,\text{eff}} = 0.7 \cdot g_s = -2.678$ and $g_l = 0$ [Wra17]. It is displayed in Fig. 6.10 by the dashed lines in the corresponding colors for each nuclear spin. The effective Schmidt-values $\mu_{\text{SV,eff}}$ describe the magnetic moments better than the Schmidt-limit, but still the moments obtained by the experiment deviate from it by several σ. Only in ^{67}Ni, just one neutron below $N = 40$, the experimental result almost agrees with the Schmidt-Limit. This is another indication for a conceivable sub-shell closure. In the $\nu p_{3/2}$ states, the deviation is the largest and would require a considerably larger reduction factor to match. This probably points towards a strongly mixed wave function for these states. This effect seems to increase, when the $\pi f_{7/2}$ orbital is not completed, hence the magnetic moments in the even $Z < 28$ neighboring elements Cr ($Z = 24$) and Fe ($Z = 26$) are deviating even stronger from the effective Schmidt-values, with ^{53}Cr = -0.47454(3) μ_N and ^{53}Fe = -0.386(15) μ_N.

Table 6.2.: Magnetic dipole moments calculated by Eq. (6.3).

A	I	μ / μ_N	$\mu_{\text{lit.}}$ / μ_N	ref.	μ_{SL} / μ_N	$\mu_{\text{S,eff.}}$ / μ_N
59	3/2	−0.7449(18)[2]			−1.913	−1.339
61	3/2	−0.7486(4)[1]	−0.750 02(4)	[Sto14]	−1.913	−1.339
63	1/2	0.4961(6)[1]	0.496(5)	[Dya17]	0.638	0.446
65	5/2	0.7588(10)[1]	0.69(6)	[Sto14]	1.366	0.957
67	1/2	0.5968(11)[1]	0.601(5)	[Sto14]	0.638	0.446

6.2.2 Electric quadrupole moments

Similarly as for the magnetic moments, the spectroscopic quadrupole moments are based on the known value of ^{61}Ni [Chi68] and calculated according to the scaling relation

$$Q_x = \frac{B_x}{B_{61}} Q_{61} \tag{6.4}$$

using the B factor from the hyperfine structure fitting. The resulting quadrupole moments of the isotopes with $I > 1/2$ are listed in Tab. 6.3. The quadrupole moments of ^{59,65}Ni have been measured for the first time. All electric quadrupole moments are small, which is expected for a semi-magic nucleus with a closed proton shell. All values are positive, indicating a prolate form.

Table 6.3.: Spectroscopic quadrupole moments calculated by Eq. (6.4) based on the literature value of ^{61}Ni from [Chi68].

A	I	Q / b	$Q_{\text{lit.}}$ / b
59	3/2	0.089(11)[8]	
61	3/2	0.163(3)[15]	0.162(15)
65	5/2	0.097(5)[9]	

Quadrupole moments of the $I = 5/2$ isotopes

Of all measured isotopes, only ^{65}Ni has a nuclear spin of $I = 5/2$. With its 37 neutrons it can be expected to form a single-hole state since in the single-particle shell-model only one neutron is missing to complete the $\nu f_{5/2}$ orbital before the $\nu p_{1/2}$-shell. In the lighter odd isotopes, ^{61,63}Ni the $\nu f_{5/2}$-states are low-lying ($\leqslant$ 90 keV) first excited states with lifetimes of 1 μs or less, which cannot be investigated by laser spectroscopy. Only for the single-particle state of $^{61\text{m}}$Ni a quadrupole moment of $Q_s = -0.20(3)$ b has been determined by the Mößbauer technique [Gör71]. In order to fertilize the discussion, the quadrupole moments of the 5/2 ground states of the neighboring ^{65,67}Zn [Wra17] isotopes are also shown in Fig. 6.11a. The g-factor of the Zn isotopes is very close to that expected for a $\nu f_{5/2}$configuration of the unpaired neutron [Wra17]. The quadrupole moments form an almost straight line when filling the $\nu f_{5/2}$ shell, which matches the typical transition of a nucleus from oblate to prolate with a vanishing spectroscopic quadrupole moment at mid-shell according to the single-particle shell model, with an effective charge for the neutron. The similarity of the quadrupole moments of ^{65}Ni and ^{67}Zn is obvious and the slightly larger value of ^{67}Zn is understandable since the open proton-shell of Zn

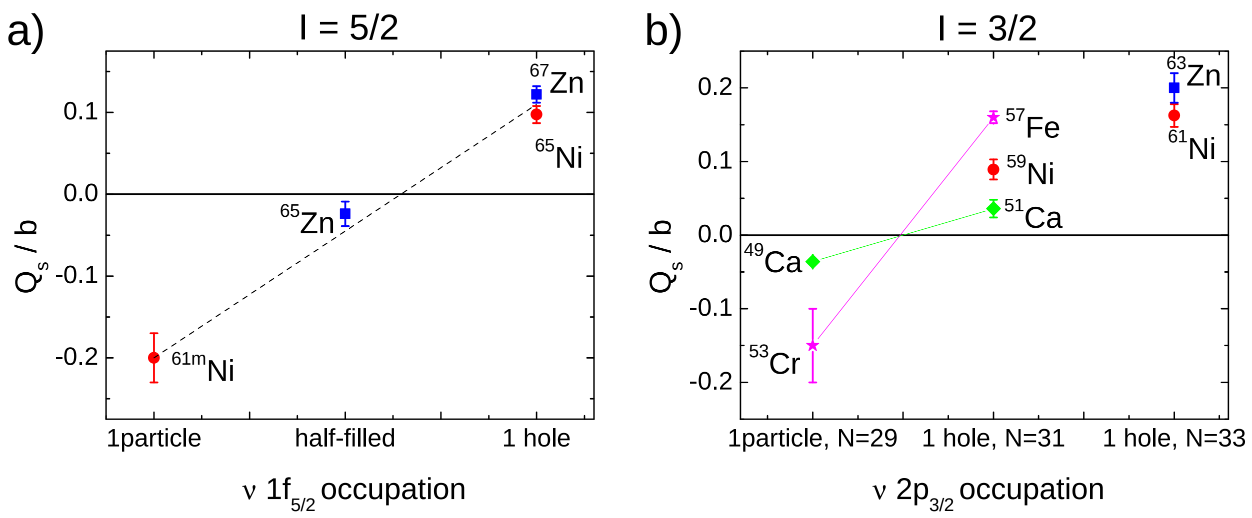

Figure 6.11.: a) Quadrupole moments for $I = 5/2$ in nickel and zinc [Wra17]. Q_s of the isomer ^{61m}Ni from [Sto14]. b) Quadrupole moments for $I = 3/2$ in nickel, zinc [Wra17], calcium [GR15], chromium and iron [Sto14].

can be expected to be more prone to polarization by the valence neutron than the magic-proton core of Ni. Similar patterns have been reported recently for example in calcium isotopes [GR15] and particularly prominent in the Cd $11/2^-$ isomers [Yor13].

Quadrupole moments of the $I = 3/2$ isotopes

The isotopes ^{59,61}Ni have a nuclear spin of $I = 3/2$ in the ground state and this quadrupole moments are included in Fig. 6.11b. Further isotopes are shown as well, in order to widen the discussion. First it has to be noticed that both $I = 3/2$ isotopes investigated here have a positive spectroscopic quadrupole moment therefore a weakly prolate form, which corresponds in the single-particle picture to a 1-hole configuration. However, the magnetic moment of these isotopes were already found to strongly deviate from the Schmidt value which indicates a mixed state, that cannot be attributed to a single-particle configuration. For the $N = 33$ 1-hole state, also ^{63}Zn ($I^\pi = 3/2^-$) is shown, which has a quadrupole moment very similar to the one in ^{61m}Ni, but slightly larger arguably for the same reason as explained for $I = 5/2$. Strikingly, Q_s of ^{59}Ni is considerably larger than that of ^{51}Ca. This can be related to the much softer ^{56}Ni proton-core than the relatively stiff $Z = 20$ core of ^{48}Ca. Finally the quadrupole moments can be compared to those of the proton-mid-shell isotopes ^{57}Fe and ^{53}Cr that show a much larger Q_s in comparison to the corresponding Ca isotopes due to increased quadrupole correlations. ^{59}Ni falls right within these two. It would be interesting to measure the spectroscopic quadrupole moment of ^{57}Ni ($I^\pi = 3/2^-$) in order to see if it falls in between ^{49}Ca and ^{53}Cr and represents the single-particle state.

7 Summary

In this work a new time-resolving data acquisition system (DAQ) for bunched-beam collinear laser spectroscopy called TILDA was developed and commissioned during a measurement campaign of nickel isotopes at COLLAPS. The real-time computing of TILDA is based on FPGAs encapsulated in a PXI-framework while the main program is realized in python, a high-level language that allows the next generation of students to get quickly familiarized with the program and adopt it to their needs. The time-resolved data has enabled unprecedented control and optimization during online monitoring of the temporal bunch structure and extend the offline-analysis capabilities significantly. The bunch structure reveals for example space-charge effects in the cooler and buncher. In a first measurement campaign, where TILDA was running in a passive mode parallel to the old DAQ system (MCP), only this feature allowed to understand unexpected shifts and broadening of the resonances caused by varying filling levels of ISCOOL. A detailed systematic study of this dependency is foreseen as an offline-test in the long shutdown within the next years. Furthermore, the time-resolved acquisition allows to set the temporal gates firmly around the region of interest, which allowed us to reduce the time gate to only 3 μs instead of the conservative 10 μs time-gates with the old DAQ. The corresponding background reduction leads to an increase in sensitivity. The decision to use primarily the data from the second measurement campaign for the final set of results was to a great deal supported by the improved data taking and control of the setup gained by TILDA.

TILDA has by now been copied and is in use at two further collinear laser spectroscopy experiments: COALA (COllinear Apparatus for Laser spectroscopy and Applied science) at TU Darmstadt and at CRYRING at GSI, where collinear laser spectroscopy is performed at a storage ring. The TRIGA-Laser beam-line, where most developments took place, is now temporarily situated at the Argonne National Laboratory and will be used for measurements on short-lived isotopes produced by CARIBU (Californium Rare Isotope Breeder Upgrade) and for measurements of the proton-halo candidate ^{8}B at ANL in the near future. Subsequently it will reach its final destination at the Low-Energy-Branch of the upcoming FAIR facility and will be operated by the LaSpec collaboration. Along the way TILDA will be kept up-to-date via a common git-server, currently situated at the TU Darmstadt and profit from the developments that are performed at the other setups.

The scientific output of this thesis are the ground-state properties of the isotopes $^{58-68,70}$Ni, measured using bunched-beam CLS at the COLLAPS experiment. At the neutron-rich production limit around $N = 42$ a customized trigger-pattern was used in order separate the few hundred ^{70}Ni isotopes per proton pulse from the vast amount of ^{70}Ga isobars. While the latter have a quick release from the target after proton impact, the nickel isotopes are delayed. This was employed to suppress accumulation of ^{70}Ga in the ISCOOL cooler and buncher and to improve the detection sensitivity. Successfully crossing the $N = 40$ sub-shell closure was essential to obtain information about a sub-shell closure in the isotopic chain. From the measured isotope shifts the charge radii were extracted using a King-Plot procedure and their trend revealed a kink in the evolution of the charge radius at ^{68}Ni, even more clearly than in the neighboring elements copper and zinc, where it is barely visible in copper and vanishes in zinc. The odd-even staggering in nickel is of normal ordering, with a decreased charge radius of the odd-N isotopes in comparison to the even-N isotopes. The three-point one neutron indicator $\Delta^{(3)}_{1n}(Z,N)$ was used to quantify the strength of the odd-even staggering and it was found to be rather constant, with a slight decrease towards the middle of the pf-shell. The experimental data was compared with theoretical results from nuclear Density Functional Theory (nDFT) and coupled-cluster calculations using interactions based on Chiral Effective Field Theory (χEFT). Surprisingly, the Fayans functional Fy(Δr) that performed so successful on the charge radii in the Ca, Cd and Sn chains does not describe the behavior in the Ni isotopes similarly well. The SV-min parametrization behaves very similar to the Fy(std) and both fail to describe the parabolic trend between shell closures as it is seen in the experimental results. The parabola in the Fy(Δr) parametrization shows a stronger curvature, but also fails to match the experimental charge radii. None of the nDFT parametrizations show a kink at the $N = 40$ sub-shell closure. The new experimental data will be an important benchmark for further development of the Fayans functional.

Coupled-cluster calculations using a variety of interactions based on χEFT became recently available for ^{68}Ni and show a strong correlation between the charge radius and the nuclear dipole polarizability. Comparison with the charge radius of this isotope, determined in this work, clearly demonstrate that the inclusion of 3-particle 3-hole excitations in the coupled-cluster calculations considerably improved the agreement with the experiment. ^{68}Ni is the first short-lived isotope for which experimental data of both observables is now available and is at the forefront where χEFT-based coupled-cluster calculations are now available.

From the hyperfine structure in the optical spectra of the odd-N isotopes the magnetic dipole and the electric quadrupole moments were extracted. The magnetic dipole moments showed that the $I = 3/2$ isotopes clearly differ from a simple single-particle model and a strong configuration mixture is to be expected in their wave function. Only ^{67}Ni at the sub-shell closure is very close to the expected Schmidt-value which can be interpreted as another sign of a shell closure. Further laser spectroscopic investigations beyond $N = 40$ and towards the doubly magic ^{78}Ni ($N = 50$) are of high interest to deepen the understanding of the structure at $N = 40$. Currently, the yields at ISOLDE are not sufficient for this kind of investigation, which is largely caused by the slow release from the target but also to the overwhelming production of isobars especially when the proton beam directly hits the production target. A new neutron converter is under development that might relax the latter problem. However, nuclear lifetimes quickly drop below 1 s beyond ^{70}Ni and this will limit the rate that can be delivered from thick-target experiments. One way out would be the production of molecular volatile Ni compounds to facilitate a quick release. This has to be combined with a break-up of the molecule for example inside ISCOOL. A similar approach has recently been used at COLLAPS for Germanium. Another possibility is the production at an in-flight facility where the produced isotopes are afterwards stopped in a gas-cell and extracted into vacuum through differential pumping stages applying ion guides or funnel structures. The only collinear beamline currently coupled to such a device is the BECOLA experiment at the National Superconducting Cyclotron Facility (NSCL) at Michigan State University (MSU). They have recently measured the doubly magic ^{56}Ni and identified first resonances of ^{55}Ni. Further work towards ^{54}Ni has been proposed and will be carried out soon. This will establish the kink of the charge radii at ^{56}Ni ($N = 28$) and provide information on the neutron skin by the comparison with the mirror partner ^{54}Fe. Once the upgrade to FRIB is completed, BECOLA will also have the chance to work further into the neutron-rich region. Further work can be carried out in the future at the Low-Energy Beamline of FAIR at the LASPEC experiment.

8 Literature

[Bar07] R. J. Bartlett and M. Musia. “Coupled-cluster theory in quantum chemistry”. In: *Rev. Mod. Phys.* 79 (1 2007), pp. 291–352. DOI: `10.1103/RevModPhys.79.291`.

[Ben03] M. Bender, P.-H. Heenen, and P.-G. Reinhard. “Self-consistent mean-field models for nuclear structure”. In: *Rev. Mod. Phys.* 75 (1 2003), pp. 121–180. DOI: `10.1103/RevModPhys.75.121`.

[Bet08] K. Bethge, G. Walter, and B. Wiedemann. *Kernphysik*. Springer, 2008.

[Bir17] J. Birkhan et al. “Electric Dipole Polarizability of ^{48}Ca and Implications for the Neutron Skin”. In: *Phys. Rev. Lett.* 118 (25 2017), p. 252501. DOI: `10.1103/PhysRevLett.118.252501`.

[Bis16] M. L. Bissell et al. “Cu charge radii reveal a weak sub-shell effect at $N = 40$”. In: *Phys. Rev. C* 93 (6 2016), p. 064318. DOI: `10.1103/PhysRevC.93.064318`.

[Bla92] B. Blank et al. “Charge-changing cross sections of the neutron-rich isotopes8,9,11Li”. In: *Zeitschrift für Physik A Hadrons and Nuclei* 343.4 (1992), pp. 375–379. DOI: `10.1007/BF01289813`.

[Bon72] J. Bonn et al. “Sudden change in the nuclear charge distribution of very light mercury isotopes”. In: *Physics Letters B* 38.5 (1972), pp. 308 –311. DOI: `10.1016/0370-2693(72)90253-5`.

[Bro95] R. Broda et al. “$N = 40$ Neutron Subshell Closure in the ^{68}Ni Nucleus”. In: *Phys. Rev. Lett.* 74 (1995), p. 868.

[Cam16] P. Campbell, I.D. Moore, and M.R. Pearson. “Laser spectroscopy for nuclear structure physics”. In: *Progress in Particle and Nuclear Physics* 86 (2016), pp. 127 –180. DOI: `10.1016/j.ppnp.2015.09.003`.

[Cas90] B. Castel and I. S. Towner. *Modern theories of nuclear moments*. English. Oxford : Clarendon Press ; New York : Oxford University Press, 1990.

[Cat03] R. Catherall et al. “Radioactive ion beams produced by neutron-induced fission at ISOLDE”. In: *Nucl. Inst. and Meth. in Phys. B* 204 (2003), pp. 235 –239. DOI: `10.1016/S0168-583X(02)01915-8`.

[Cat17] R. Catherall et al. “The ISOLDE facility”. In: *Journal of Physics G: Nuclear and Particle Physics* 44.9 (2017), p. 094002. DOI: `10.1088/1361-6471/aa7eba`.

[Che10] B. Cheal et al. “Nuclear Spins and Moments of Ga Isotopes Reveal Sudden Structural Changes between $N = 40$ and $N = 50$”. In: *Phys. Rev. Lett.* 104 (25 2010), p. 252502. DOI: `10.1103/PhysRevLett.104.252502`.

[Chi68] W. J. Childs and L. S. Goodman. “Hyperfine-Structure Studies of ^{61}Ni, and the nuclear Ground-State Electric Quadrupole Moment”. In: *Phys. Rev.* 170 (1 1968), pp. 136–140. DOI: `10.1103/PhysRev.170.136`.

[Dem10] W. Demtröder. *Experimentalphysik 3, Atome, Molekule und Festkorper*. Springer, 2010.

[Dem11] W. Demtröder. *Laserspektroskopie 1*. Springer, 2011.

[Dra06] G. Drake. *Atomic, Molecular, and Optical Physics*. Springer, 2006.

[Dra64] L.E. Drain. “The magnetic moment of Ni61”. In: *Physics Letters* 11.2 (1964), pp. 114 –115. DOI: `10.1016/0031-9163(64)90633-X`.

[Dug14] T. Duguet. “The Nuclear Energy Density Functional Formalism”. In: (2014), pp. 293–350. DOI: `10.1007/978-3-642-45141-6_7`.

[Dya17] A. B. Dyachkov et al. “Hyperfine structure of electronic levels and the first measurement of the nuclear magnetic moment of ^{63}Ni”. In: *The European Physical Journal A* 53.1 (2017), p. 13. DOI: `10.1140/epja/i2017-12197-5`.

[Eks15] A. Ekström et al. “Accurate nuclear radii and binding energies from a chiral interaction”. In: *Phys. Rev. C* 91 (5 2015), p. 051301. DOI: `10.1103/PhysRevC.91.051301`.

[Ent03] D. R. Entem and R. Machleidt. “Accurate charge-dependent nucleon-nucleon potential at fourth order of chiral perturbation theory”. In: *Phys. Rev. C* 68 (4 2003), p. 041001. DOI: `10.1103/PhysRevC.68.041001`.

[Epe09] E. Epelbaum, H.-W. Hammer, and U.-G. Meißner. “Modern theory of nuclear forces”. In: *Rev. Mod. Phys.* 81 (4 2009), pp. 1773–1825. DOI: `10.1103/RevModPhys.81.1773`.

[Fay00] S.A. Fayans et al. “Nuclear isotope shifts within the local energy-density functional approach”. In: *Nuclear Physics A* 676.1 (2000), pp. 49 –119. DOI: `10.1016/S0375-9474(00)00192-5`.

[Fed08] V.N. Fedosseev et al. “ISOLDE RILIS: New beams, new facilities”. In: *Nucl. Inst. and Meth. in Physics B* 266.19 (2008). Proceedings of the XVth International Conference on Electromagnetic Isotope Separators and Techniques Related to their Applications, pp. 4378 –4382. DOI: `10.1016/j.nimb.2008.05.038`.

[Fra08] H. Franberg et al. “Off-line commissioning of the ISOLDE cooler”. In: *Nucl. Inst. and Meth. in Phys. B* 266.19 (2008), pp. 4502 –4504. DOI: `10.1016/j.nimb.2008.05.097`.

[Fri04] G. Fricke and K. Heilig. *Nuclear Charge Radii*. Vol. 20. Group I: Elementary Particles, Nuclei and Atoms Volume 20. Springer, 2004.

[GM48] M. Goeppert Mayer. “On Closed Shells in Nuclei”. In: *Phys. Rev.* 74 (3 1948), pp. 235–239. DOI: `10.1103/PhysRev.74.235`.

[GM49] M. Goeppert Mayer. “On Closed Shells in Nuclei. II”. In: *Phys. Rev.* 75 (12 1949), pp. 1969–1970. DOI: `10.1103/PhysRev.75.1969`.

[God13] P. M. Goddard, P. D. Stevenson, and A. Rios. “Charge Radius Isotope Shift Across the N=126 Shell Gap”. In: *Phys. Rev. Lett.* 110 (3 2013), p. 032503. DOI: `10.1103/PhysRevLett.110.032503`.

[Gor17] C. Gorges. *Kollineare Laserspektroskopie an Calcium und Zinn an TRIGA-LASER und ISOLDE*. Doktorarbeit an der Technischen Universität Darmstadt. 2017.

[Gor19] C. Gorges et al. “Laser Spectroscopy of Neutron-Rich Tin Isotopes: A Discontinuity in Charge Radii across the $N = 82$ Shell Closure”. In: *Phys. Rev. Lett.* 122 (19 2019), p. 192502. DOI: `10.1103/PhysRevLett.122.192502`.

[GR15] R. F. Garcia Ruiz et al. “Ground-state electromagnetic moments of calcium isotopes”. In: *Phys. Rev. C* 91 (4 2015), p. 041304. DOI: `10.1103/PhysRevC.91.041304`.

[GR16] R. F. Garcia Ruiz et al. “Unexpectedly large charge radii of neutron-rich calcium isotopes”. In: *Nature Physics* 12 (2016). Article, 594 EP –. DOI: `10.1038/nphys3645`.

[Gue07] C. Guenaut et al. “High-precision mass measurements of nickel, copper, and gallium isotopes and the purported shell closure at $N = 40$”. In: *Phys. Rev. C* 75 (4 2007), p. 044303. DOI: `10.1103/PhysRevC.75.044303`.

[Gör71] J. Göring. “The Nuclear Moments of the 67.4 keV Level in ^{61}Ni”. In: *Zeitschrift für Naturforschung A* 61 (11 1971), pp. 1931–1932. DOI: `10.1515/zna-1971-1126`.

[Hag09] G. Hagen et al. “Ab initio computation of neutron-rich oxygen isotopes”. In: *Phys. Rev. C* 80 (2 2009), p. 021306. DOI: `10.1103/PhysRevC.80.021306`.

[Hag14] G. Hagen et al. “Coupled-cluster computations of atomic nuclei”. In: *Reports on Progress in Physics* 77.9 (2014), p. 096302. DOI: `10.1088/0034-4885/77/9/096302`.

[Hag15] G. Hagen et al. “Neutron and weak-charge distributions of the ^{48}Ca nucleus”. In: *Nature Physics* 12 (2015), pp. 186–190. DOI: `10.1038/nphys3529`.

[Ham18] M. Hammen et al. “From Calcium to Cadmium: Testing the Pairing Functional through Charge Radii Measurements of $^{100-130}$Cd”. In: *Phys. Rev. Lett.* 121 (10 2018), p. 102501. DOI: `10.1103/PhysRevLett.121.102501`.

[Heb11] K. Hebeler et al. “Improved nuclear matter calculations from chiral low-momentum interactions”. In: *Phys. Rev. C* 83 (3 2011), p. 031301. DOI: `10.1103/PhysRevC.83.031301`.

[Hof56] Robert Hofstadter. “Electron Scattering and Nuclear Structure”. In: *Rev. Mod. Phys.* 28 (3 1956), pp. 214–254. DOI: `10.1103/RevModPhys.28.214`.

[Hon02] M. Honma et al. “Effective interaction for pf-shell nuclei”. In: *Phys. Rev. C* 65 (6 2002), p. 061301. DOI: `10.1103/PhysRevC.65.061301`.

[Ins14] National Instruments. *NI LabVIEW High-Performance FPGA Developer’s Guide*. 2014.

[Kau13] S. Kaufmann. *Spezifikation der Energieunschärfe gekühlter und gepulster Ionenstrahlen mittels Laserspektroskopie*. Diplomarbeit an der Johannes–Gutenberg Universität Mainz. 2013.

[Kau76] S. L. Kaufman. “High-resolution laser spectroscopy in fast beams”. In: *Optics Communications* 17.3 (1976), pp. 309–312. DOI: `10.1016/0030-4018(76)90267-4`.

[Kei95] M. Keim et al. “Laser-spectroscopy measurements of 72–96Kr spins, moments and charge radii”. In: *Nuclear Physics A* 586.2 (1995), pp. 219 –239. DOI: `10.1016/0375-9474(94)00786-M`.

[Kin84] W. H. King. *Isotope shifts in atomic spectra*. Springer US, 1984.

[Klü09] P. Klüpfel et al. “Variations on a theme by Skyrme: A systematic study of adjustments of model parameters”. In: *Phys. Rev. C* 79 (3 2009), p. 034310. DOI: `10.1103/PhysRevC.79.034310`.

[Krä10] J. Krämer. *Construction and Commissioning of a Collinear Laser Spectroscopy Setup at TRIGA Mainz and Laser Spectroscopy of Magnesium Isotopes at ISOLDE (CERN)*. Doktorarbeit an der Johannes–Gutenberg Universität Mainz. 2010.

[Küh77] T. Kühl et al. “Nuclear Shape Staggering in Very Neutron-Deficient Hg Isotopes Detected by Laser Spectroscopy”. In: *Phys. Rev. Lett.* 39 (4 1977), pp. 180–183. DOI: `10.1103/PhysRevLett.39.180`.

[Lan03] K. Langanke et al. “How magic is the magic ^{68}Ni nucleus?” In: *Phys. Rev. C* 67 (4 2003), p. 044314. DOI: `10.1103/PhysRevC.67.044314`.

[Les16] M. Lestinsky et al. “Physics book: CRYRING@ESR”. In: *The European Physical Journal Special Topics* 225.5 (2016), pp. 797–882. DOI: `10.1140/epjst/e2016-02643-6`.

[Let87] V. S. Letokhov and V. I. Mishin. “Ultrasensitive Laser Photoionization Spectroscopy of Short-Lived Isotopes and Very Rare Atoms”. In: *Laser Spectroscopy VIII*. Ed. by Willy Persson and Sune Svanberg. Berlin, Heidelberg: Springer Berlin Heidelberg, 1987, pp. 167–175. DOI: `10.1007/978-3-540-47973-4_44`.

[Lie96] P. Lievens et al. “On the odd-even staggering of mean-square charge radii in the light krypton and strontium region”. In: *Europhysics Letters (EPL)* 33.1 (1996), pp. 11–16. DOI: `10.1209/epl/i1996-00296-0`.

[Maa19] B. Maaß et al. “Nuclear Charge Radii of ^{10,11}B”. In: *Phys. Rev. Lett.* 122 (18 2019), p. 182501. DOI: `10.1103/PhysRevLett.122.182501`.

[Mac11] R. Machleidt and D.R. Entem. “Chiral effective field theory and nuclear forces”. In: *Physics Reports* 503.1 (2011), pp. 1 –75. DOI: `10.1016/j.physrep.2011.02.001`.

[Mey83] W. D. Meyers and K.-H. Schmidt. “An update on droplet-model charge distributions”. In: *Nuclear Physics A* 410 (1983), pp. 61–73. DOI: `10.1016/0375-9474(83)90401-3`.

[Mil19] A. J. Miller et al. “Proton superfluidity and charge radii in proton-rich calcium isotopes”. In: *Nature Physics* 15.5 (2019), pp. 432–436. DOI: `10.1038/s41567-019-0416-9`.

[Mio18] M. Miorelli et al. “Computing the dipole polarizability of ^{48}Ca with increased precision”. In: *Phys. Rev. C* 98 (1 2018), p. 014324. DOI: `10.1103/PhysRevC.98.014324`.

[Mül83] A.C. Müller et al. “Spins, moments and charge radii of barium isotopes in the range $^{122-146}$Ba determined by collinear fast–beam laser spectroscopy”. In: *Nucl. Phys. A* 403 (1983), p. 234.

[Mül89] W. Müller et al. “Magnetic hyperfine interaction studies of isolated Ni impurities in Pd and Pd-Pt alloys”. In: *Phys. Rev. B* 40 (11 1989), pp. 7633–7641. DOI: `10.1103/PhysRevB.40.7633`.

[Neu06] R. Neugart and G. Neyens. “Nuclear Moments”. In: *The Euroschool Lectures on Physics with Exotic Beams, Vol. II*. Ed. by Jim Al-Khalili and Ernst Roeckl. Vol. 700. Lecture Notes in Physics. Springer Berlin Heidelberg, 2006, pp. 135–189. DOI: `10.1007/3-540-33787-3_4`.

[Neu17] R. Neugart et al. “Collinear laser spectroscopy at ISOLDE: new methods and highlights”. In: *Journal of Physics G: Nuclear and Particle Physics* 44.6 (2017), p. 064002. DOI: `10.1088/1361-6471/aa6642`.

[Neu81a] R. Neugart. “Laser Spectroscopy on Mass-Separated Radioactive Beams”. In: *Nuclear Instruments and Methods* 186 (1981), pp. 165–175. DOI: `10.1016/0029-554X(81)90902-2`.

[Neu81b] R. Neugart et al. “Fast-beam laser spectroscopy of neutron-rich barium isotopes”. In: *Hyperfine Interactions* 9.1 (1981), pp. 151–157. DOI: `10.1007/BF01020911`.

[Neu86] R. Neugart, W. Klempt, and K. Wendt. “Collisional ionization as a sensitive detection scheme in collinear laser-fast-beam spectroscopy”. In: *Nuclear Instruments and Methods in Physics Research Section B: Beam Interactions with Materials and Atoms* 17.4 (1986), pp. 354 –359. DOI: `https://doi.org/10.1016/0168-583X(86)90125-4`.

[Nie02] A. Nieminen et al. “On–line ion cooling and bunching for collinear laser spectroscopy”. In: *Physical review letters* 88.9 (2002), p. 094801. DOI: `10.1103/PhysRevLett.88.094801`.

[Ott89] E.W. Otten. “Nuclear Radii and Moments of Unstable Isotopes”. English. In: *Treatise on Heavy Ion Science*. Ed. by D.Allan Bromley. Springer US, 1989, pp. 517–638. DOI: `10.1007/978-1-4613-0713-6_7`.

[Pau08] D. Pauwels et al. “Shape isomerism at $N = 40$: Discovery of a proton intruder state in ^{67}Co”. In: *Phys. Rev. C* 78 (4 2008), p. 041307. DOI: `10.1103/PhysRevC.78.041307`.

[Pau10] D. Pauwels et al. “Pairing-excitation versus intruder states in ^{68}Ni and ^{90}Zr”. In: *Phys. Rev. C* 82 (2 2010), p. 027304. DOI: `10.1103/PhysRevC.82.027304`.

[Puc15] M. Puchalski, J. Komasa, and K. Pachucki. “Explicitly correlated wave function for a boron atom”. In: *Phys. Rev. A* 92 (6 2015), p. 062501. DOI: `10.1103/PhysRevA.92.062501`.

[Rah07] S. Rahaman et al. “Masses of neutron-rich Ni and Cu isotopes and the shell closure at $Z = 28$, $N = 40$”. In: *Euro. Phys. Journal A* 34.1 (2007), pp. 5–9. DOI: `10.1140/epja/i2007-10489-y`.

[Rei17] P.-G. Reinhard and W. Nazarewicz. “Toward a global description of nuclear charge radii: Exploring the Fayans energy density functional”. In: *Phys. Rev. C* 95 (6 2017), p. 064328. DOI: `10.1103/PhysRevC.95.064328`.

[Rei19] P.-G. Reinhard. In: *private communication* (2019).

[RM15] X. Roca-Maza et al. “Neutron skin thickness from the measured electric dipole polarizability in ^{68}Ni, ^{120}Sn, and ^{208}Pb”. In: *Phys. Rev. C* 92 (6 2015), p. 064304. DOI: `10.1103/PhysRevC.92.064304`.

[Ros13] D. M. Rossi et al. “Measurement of the Dipole Polarizability of the Unstable Neutron-Rich Nucleus ^{68}Ni”. In: *Phys. Rev. Lett.* 111 (24 2013), p. 242503. DOI: `10.1103/PhysRevLett.111.242503`.

[Ros15] D. M. Rossi et al. “Charge radii of neutron-deficient ^{36}K and ^{37}K”. In: *Phys. Rev. C* 92 (1 2015), p. 014305. DOI: `10.1103/PhysRevC.92.014305`.

[Rut11] E. Rutherford. “LXXIX. The scattering of α and β particles by matter and the structure of the atom”. In: *The London, Edinburgh, and Dublin Philosophical Magazine and Journal of Science* 21.125 (1911), pp. 669–688. DOI: `10.1080/14786440508637080`.

[Ryd15] C.A. Ryder et al. “Population distribution subsequent to charge exchange of 29.85 keV Ni$^+$ on sodium vapor”. In: *Spectrochimica Acta Part B: Atomic Spectroscopy* 113 (2015), p. 16. DOI: `10.1016/j.sab.2015.08.004`.

[Sch78] B. Schinzler et al. “Collinear laser spectroscopy of neutron-rich Cs isotopes at an on-line mass separator”. In: *Physics Letters B* 79.3 (1978), pp. 209 –212. DOI: `10.1016/0370-2693(78)90224-1`.

[Sor02] O. Sorlin et al. “${}^{68}_{28}\mathrm{Ni}_{40}$: Magicity versus superfluidity”. In: *Phys. Rev. Lett.* 88 (9 2002), p. 092501. DOI: `10.1103/PhysRevLett.88.092501`.

[Sor08] O. Sorlin and M.-G. Porquet. “Nuclear magic numbers: New features far from stability”. In: *Progress in Particle and Nuclear Physics* 61.2 (2008), pp. 602 –673. DOI: `10.1016/j.ppnp.2008.05.001`.

[Sto14] N. J. Stone. “Table of Nuclear Magnetic Dipole and Electric Quadrupole Moments”. In: *International Nuclear Information System* 45.11 (2014), p. 171. DOI: `RN:45029196`.

[Sud17] Toshimi Suda and Haik Simon. “Prospects for electron scattering on unstable, exotic nuclei”. In: *Progress in Particle and Nuclear Physics* 96 (2017), pp. 1 –31. DOI: `10.1016/j.ppnp.2017.04.002`.

[Tan19] R. Taniuchi et al. “^{78}Ni revealed as a doubly magic stronghold against nuclear deformation”. In: *Nature* 569.7754 (2019), pp. 53–58. DOI: `10.1038/s41586-019-1155-x`.

[Thi81] C. Thibault et al. “Hyperfine structure and isotope shift of the D_2 line of ${}^{76-98}$Rb and some of their isomers”. In: *Phys. Rev. C* 23 (6 1981), pp. 2720–2729. DOI: `10.1103/PhysRevC.23.2720`.

[Wan17] M. Wang et al. “The AME2016 atomic mass evaluation (II). Tables, graphs and references”. In: *Chinese Physics C* 41.3 (2017), p. 030003. DOI: `10.1088/1674-1137/41/3/030003`.

[Wei35] C. F. v. Weizsaecker. “Zur Theorie der Kernmassen”. In: *Zeitschrift fuer Physik* 96.7 (1935), pp. 431–458. DOI: `10.1007/BF01337700`.

[Wei90] S. Weinberg. “Nuclear forces from chiral lagrangians”. In: *Physics Letters B* 251.2 (1990), pp. 288 –292. DOI: `10.1016/0370-2693(90)90938-3`.

[Wel17] A. Welker et al. “Binding Energy of ^{79}Cu: Probing the Structure of the Doubly Magic ^{78}Ni from Only One Proton Away”. In: *Phys. Rev. Lett.* 119 (19 2017), p. 192502. DOI: `10.1103/PhysRevLett.119.192502`.

[Wir95] R. B. Wiringa, V. G. J. Stoks, and R. Schiavilla. “Accurate nucleon-nucleon potential with charge-independence breaking”. In: *Phys. Rev. C* 51 (1 1995), pp. 38–51. DOI: `10.1103/PhysRevC.51.38`.

[Wra17] C. Wraith et al. “Evolution of nuclear structure in neutron-rich odd-Zn isotopes and isomers”. In: *Physics Letters B* 771.Supplement C (2017), pp. 385 –391. DOI: `10.1016/j.physletb.2017.05.085`.

[Xie18] L. Xie. In: *private communication* (2018).

[Xu14] Z. Y. Xu et al. “β-Decay Half-Lives of ^{76,77}Co, ^{79,80}Ni, and ^{81}Cu: Experimental Indication of a Doubly Magic ^{78}Ni”. In: *Phys. Rev. Lett.* 113 (3 2014), p. 032505. DOI: `10.1103/PhysRevLett.113.032505`.

[Yam11] T. Yamaguchi et al. “Scaling of Charge-Changing Interaction Cross Sections and Point-Proton Radii of Neutron-Rich Carbon Isotopes”. In: *Phys. Rev. Lett.* 107 (3 2011), p. 032502. DOI: `10.1103/PhysRevLett.107.032502`.

[Yor04] D. York et al. “Unified equations for the slope, intercept, and standard errors of the best straight line”. In: *American Journal of Physics* 72.3 (2004), pp. 367–375. DOI: `10.1119/1.1632486`.

[Yor13] D. T. Yordanov et al. “Spins, Electromagnetic Moments, and Isomers of$^{107-129}$Cd”. In: *Phys. Rev. Lett.* 110 (2013), p. 192501. DOI: `10.1103/PhysRevLett.110.192501`.

[Yor16] D. T. Yordanov et al. “Simple Nuclear Structure in $^{111-129}$Cd from Atomic Isomer Shifts”. In: *Phys. Rev. Lett.* 116 (2016), p. 032501.

[Yu02] C.-H. Yu et al. “Rotational bands with terminating properties in ^{59}Ni”. In: *Phys. Rev. C* 65 (6 2002), p. 061302. DOI: `10.1103/PhysRevC.65.061302`.

[Zie12] F. Ziegler et al. “A new Pulse-Pattern Generator based on LabVIEW-FPGA”. In: *Nucl. Instr. Meth. A* 679 (2012), pp. 1–6. DOI: `10.1016/j.nima.2012.03.010`.

A Appendix

A.1 Isotope shifts of all files versus the bunch length

In this chapter the plots of all isotopes are to be found for completion since not all were shown in the discussion around this issue in chapter 5.2.3. The basic idea behind these plots is to find a connection between the isotope shift and the amount of ions per bunch in ISCOOL.

A.1.1 Bunch length of all files

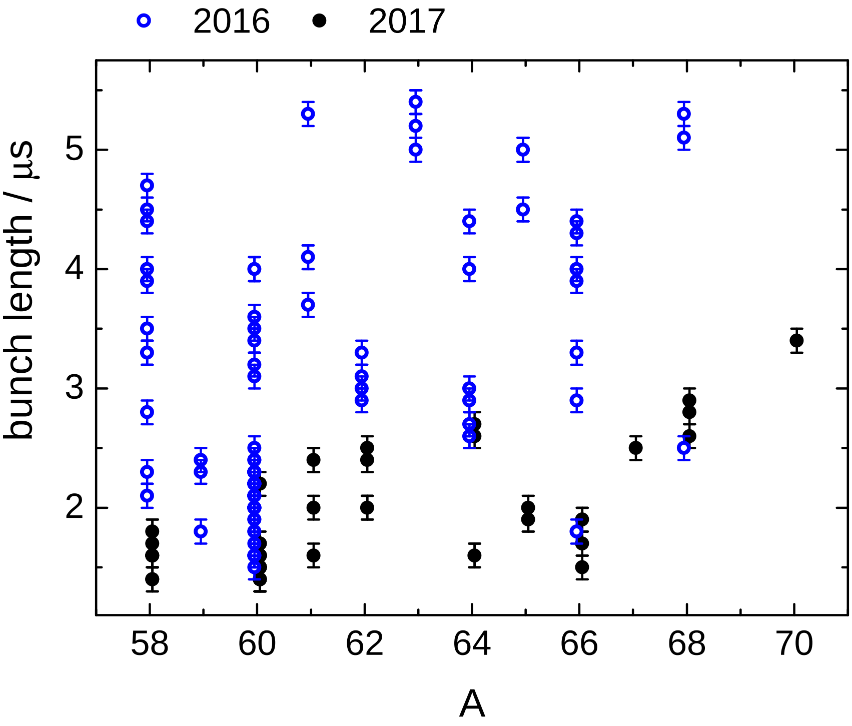

Figure A.1.: Bunch lengths with 25% of the maximum counts for all relevant files of the 2016 and 2017 beam time. Unfortunately for ^{67,70}Ni no time-resolved data was acquired in 2016 and ^{59,63}Ni were missed out in 2017.

A.1.2 ^{58}Ni

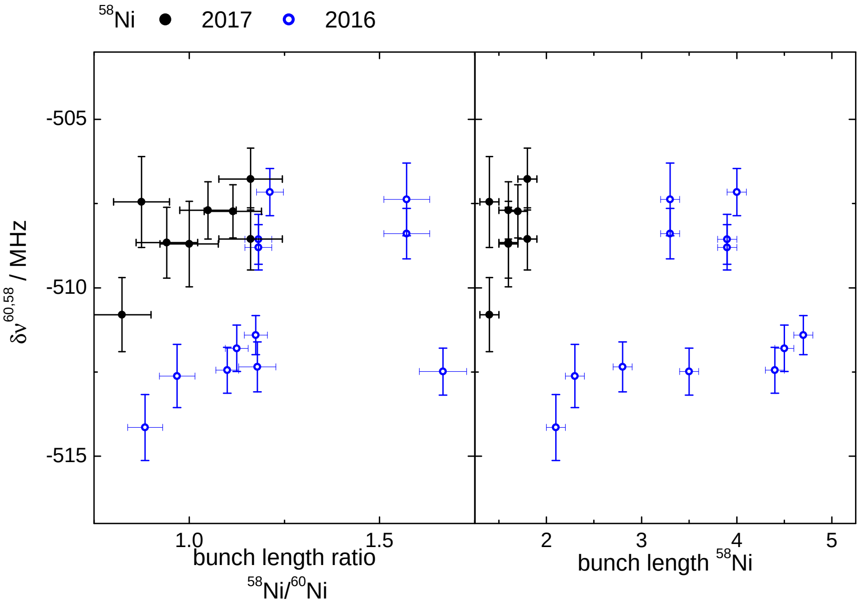

Figure A.2.: Isotope shift of all ^{58}Ni files acquired in 2016 and 2017 plotted versus their bunch length ratio to their surrounding ^{60}Ni reference files (left) and versus their individual bunch length (right).

A.1.3 ^{59}Ni

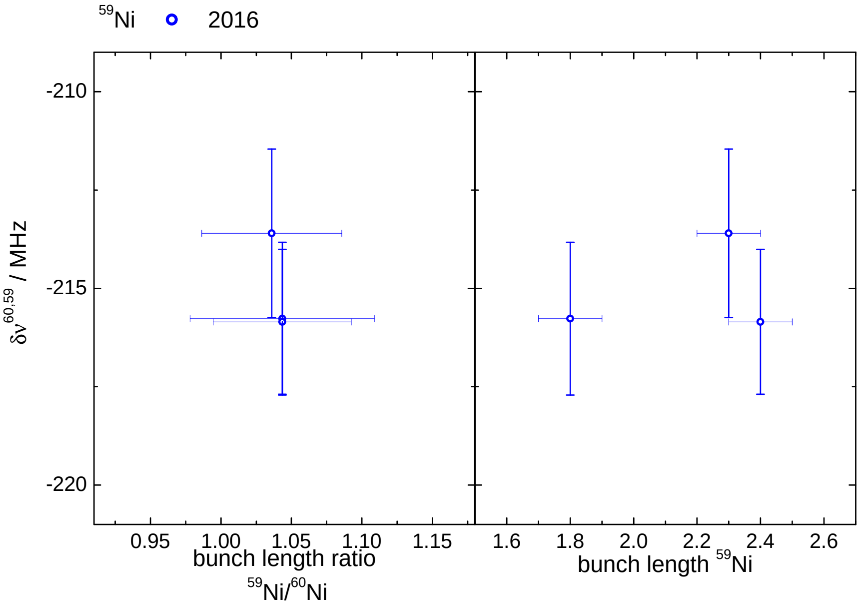

Figure A.3.: Isotope shift of all ^{59}Ni files acquired in 2016 and 2017 plotted versus their bunch length ratio to their surrounding ^{60}Ni reference files (left) and versus their individual bunch length (right).

A.1.4 ^{61}Ni

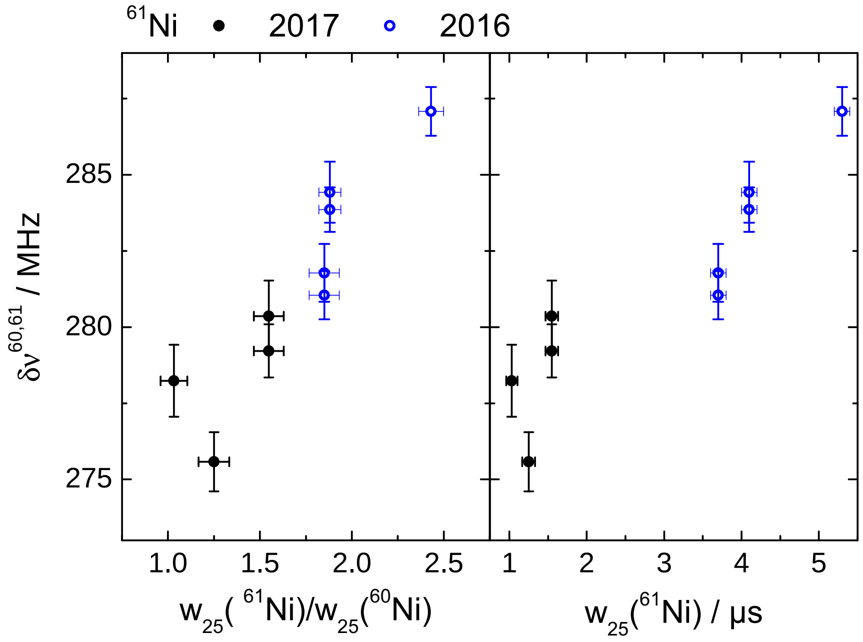

Figure A.4.: Isotope shift of all ^{61}Ni files acquired in 2016 and 2017 plotted versus their bunch length ratio to their surrounding ^{60}Ni reference files (left) and versus their individual bunch length (right).

A.1.5 ^{62}Ni

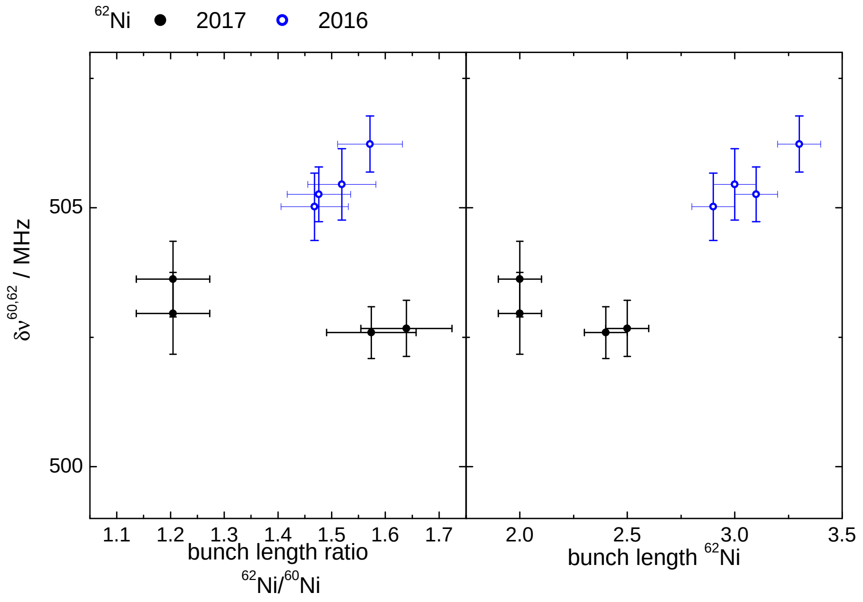

Figure A.5.: Isotope shift of all ^{62}Ni files acquired in 2016 and 2017 plotted versus their bunch length ratio to their surrounding ^{60}Ni reference files (left) and versus their individual bunch length (right).

A.1.6 ^{63}Ni

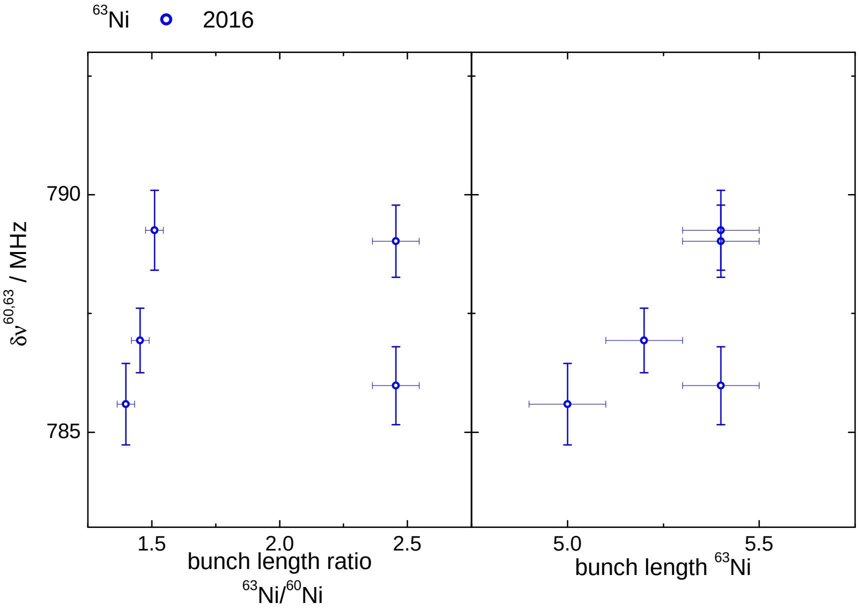

Figure A.6.: Isotope shift of all ^{63}Ni files acquired in 2016 and 2017 plotted versus their bunch length ratio to their surrounding ^{60}Ni reference files (left) and versus their individual bunch length (right).

A.1.7 ^{64}Ni

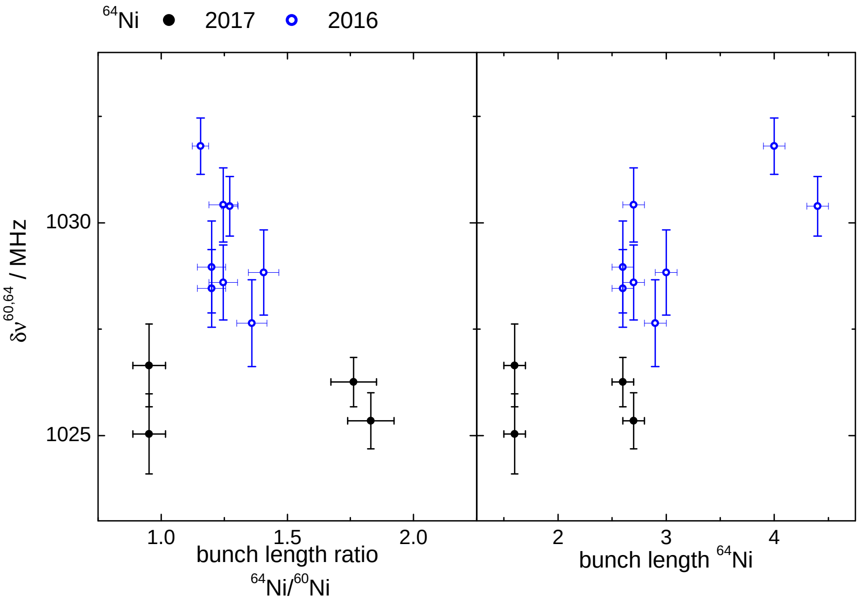

Figure A.7.: Isotope shift of all ^{64}Ni files acquired in 2016 and 2017 plotted versus their bunch length ratio to their surrounding ^{60}Ni reference files (left) and versus their individual bunch length (right).

A.1.8 ^{65}Ni

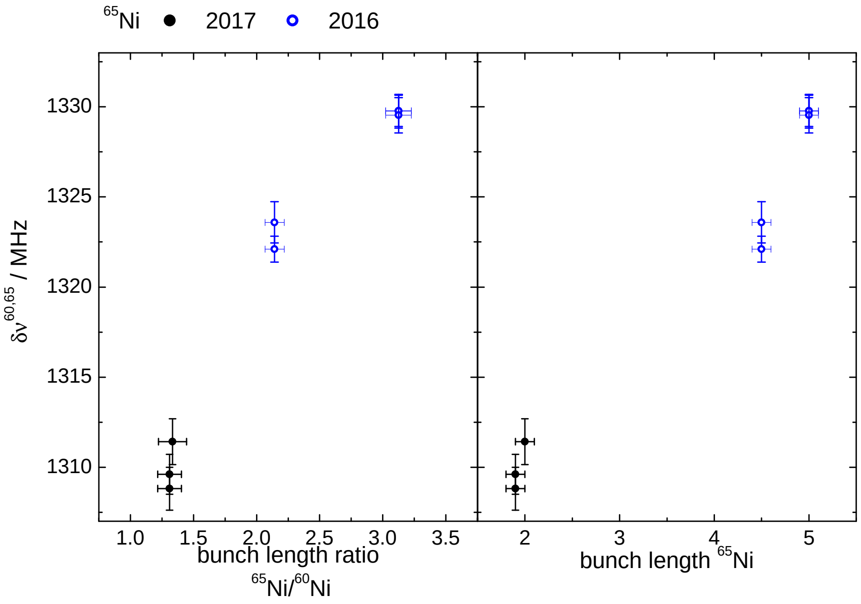

Figure A.8.: Isotope shift of all ^{65}Ni files acquired in 2016 and 2017 plotted versus their bunch length ratio to their surrounding ^{60}Ni reference files (left) and versus their individual bunch length (right).

A.1.9 ^{66}Ni

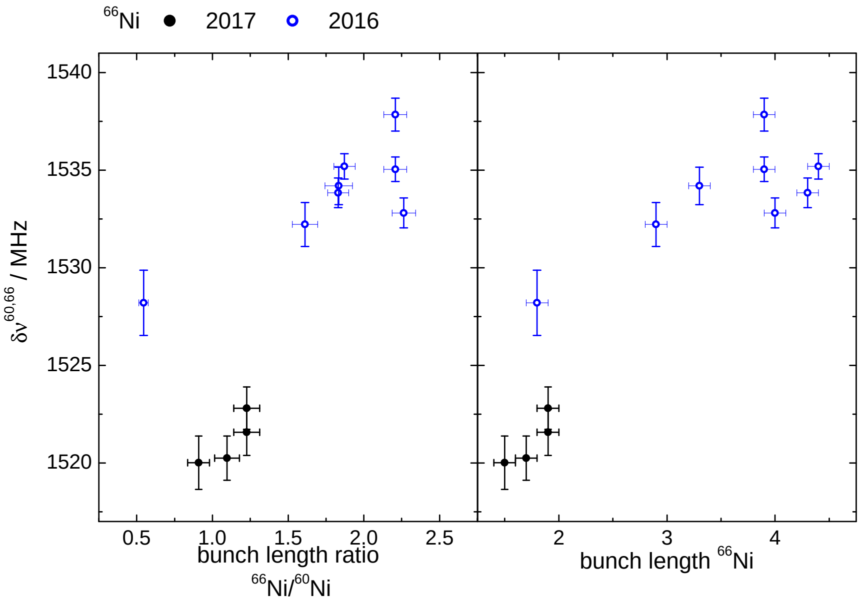

Figure A.9.: Isotope shift of all ^{66}Ni files acquired in 2016 and 2017 plotted versus their bunch length ratio to their surrounding ^{60}Ni reference files (left) and versus their individual bunch length (right).

A.1.10 ^{68}Ni

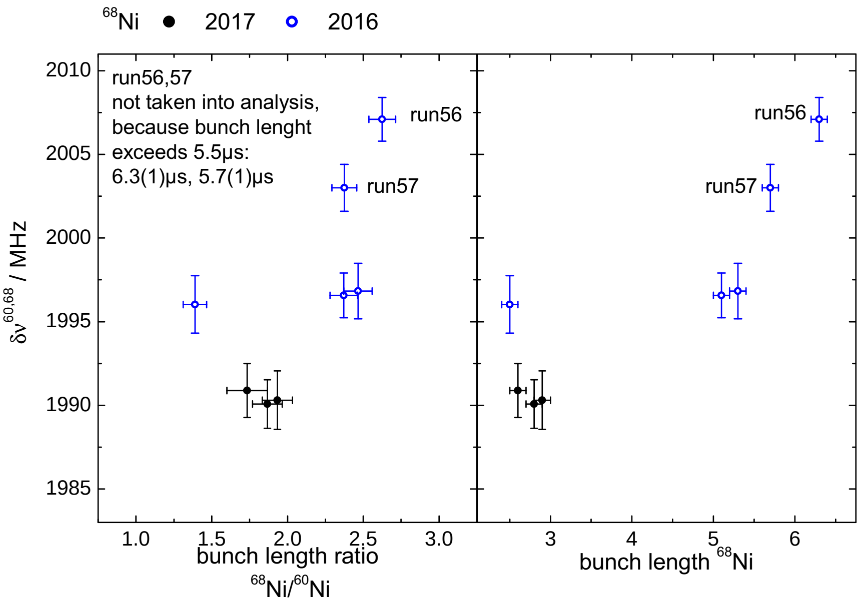

Figure A.10.: Isotope shift of all ^{68}Ni files acquired in 2016 and 2017 plotted versus their bunch length ratio to their surrounding ^{60}Ni reference files (left) and versus their individual bunch length (right).

Acknowledgment

In the following I would like to thank all colleagues and friends for the support, that have helped to make this thesis possible. First of all I thank Wilfried Nörtershäuser for the opportunity to work in this exciting field in form of a PhD. Without his guidance this PhD would not have been achievable. I am glad that I could learn a fraction from his extensive expertise in the field and that he was always available, when I was in need of an advise, whether it be on short notice or in the semi-annual HGS-HIRe meetings. Also many thanks goes to Christoph Düllmann and Jörg Krämer for co-mentoring me in the framework of this program. For examining this thesis as a second advisor I thank Thomas Aumann.

Further I would like to thank all members of the LaserSpHERe group, for the great atmosphere, smooth co-working and all the expertise provided untroubled and quickly. Especially Christian Gorges and Michael Hammen as the remaining local experts of TRIGA-LASER experiment were always fun to work with. Sincere thanks goes to Michael for guiding me into the puzzling world of programming and helping me in the foundation of TILDA. You got me really fascinated in this field and not only by impressing me with your programming skills, but also by being a friend besides the office hours. Christian, we started together and I could not imagine a better discussion partner. Thank you for all the advice, helping me with the programming or in the lab, voluntary supporting the acquisition during the night shift, sharing an office with me for such a long time and above all being a friend. I also thank everybody who came by regularly, or on short notice, when we were operating TRIGA-LASER and were in need of additional workforce. When anything was acting strange with the beam line Jörg was never shy of a visit, if he was not there anyhow helping out to operate the experiment. If the Laser was having a bad day, Rodolfo Sanchéz was always only a phone call away and never ceased to amaze us with his skills, always tutoring and explaining while steadily turning knobs. Then of course I thank Christopher Geppert for passing by almost on a daily basis, either at the experiment or during lunch breaks and providing all his expertise that he has acquired throughout his years in laser spectroscopy, when we were puzzled by unexpected effects in the experiment or in a need of an advice. On the technical site I would like to thank Tobias Gerhardt, for all the help in developing the DAC-board, which was intergrated in the TTL-Linedriver and all the further electronic support.

I am also very grateful to all the Darmstadt members of the LaserSpHERe group who always welcomed me when I was on a visit and supported me with the local infrastructure. In the introduction of TILDA at the COALA beam line, especially Felix Sommer is to be thanked, since he spent a lot of hours adapting the required local changes in TILDA. Further I thank you for taking the time to learn TILDA to the *bone* in order to continue the development of TILDA in the near future and I hope that you will find someone as eager as you to pass TILDA on to. Also I thank everybody who was using TILDA already in an early phase and provided me with valuable feedback.

A warm welcome was also always ensured when visiting COLLAPS and therefore I would like to thank the whole collaboration and especially the local group. It was a wonderful and challenging work environment and I would like to thank you all for the support during the nickel beam times. Especially in chaotic times, like in the first nickel beam time, where a weasel had caused a CERN wide power cut, all of you showed your expertise and had the experiment running again in no

time, after the operators did their magic and got ISOLDE back online. Your combined experience has also shown to be very helpful in all the feedback I received to improve TILDA throughout the years. A special thanks goes to Stephan Malbrunot-Ettenauer, who was always available for a fruitful discussion, even when operating on multiple experiments and always had a helping hand when introducing TILDA at COLLAPS. Same goes for Hanne Heylen and Ronald Garcia-Ruiz who made my stays very enjoyable and a great learning experience. Also I would like to thank Mark Bissell for all the help with the laser system and getting the frequency doubling working, even if the crystal was cut in the inverted dimensions. I thank also Rainer Neugart for the discussions during the analysis of the data.

Andrè, Nils and Oliver I would like to thank you very much, without you around I would have not made it through my diploma. You made my time at the university very special and I am glad to have you as friends.

From time to time studying had driven me up the walls and I am glad that I found a healthy way of doing so with the *Klettergruppe-Uni-Mainz*. I would like to thank you all for sharing this passion with me, I am grateful to have met all these nice people here, who had such a strong influence on my life besides studying.

At last but not least, I want to give a huge thank you to my family. I thank my parents for their support, love and belief in me. Also I would like to thank my brother Henning and his wife for everything during all those years. The largest thank you belongs to my wife Vera, for being so understanding through all those years and supporting me in every way. I would not be here without you around. Also I thank my son Kilian to enliven my days on the last steps of this work.

Simon Kaufmann

Personal data

date of birth: 18.01.1988
place of birth: Koblenz
e-mail: s.kaufmann@uni-mainz.de

Graduation

04/2014 - 11/2019	**Graduation** in the group of Prof. Wilfried Nörtershäuser, Institut für Kernphysik, Technische Universität Darmstadt. Thesis title: *Laser spectroscopy of nickel isotopes with a new data acquisition system at ISOLDE* Regular participation at experiments at CERN Conseil Européen pour la Recherche Nucléaire Member of the Helmholtz Graduate School for Hadron and Ion Research

University education

11/2013 - 04/2014	**Scientific assistant**, Johannes-Gutenberg Universität Mainz
11/2012 - 11/2013	**Diploma thesis** in the group of Prof. Wilfried Nörtershäuser, Institut für Kernchemie, Johannes-Gutenberg Universität Mainz. Thesis title: *Spezifikation der Energieunschärfe gekühlter und gepulster Ionenstrahlen mittels Laserspektroskopie*
04/2008 - 11/2013	**Studies of physics**, Johannes-Gutenberg Universität Mainz

School and civilian service

2007 - 2008	**Civilian service**, Johanniter-Unfall-Hilfe e.V.
1998 - 2007	**Abitur**, Gymnasium Höhr-Grenzhausen

List of publications

Publications in peer-reviewed journals

2019

Nuclear charge radii of 62-80Zn and their dependence on cross-shell proton excitations
L. Xie, X. F. Yang, C. Wraith, C. Babcock, J. Bieroń, J. Billowes, M. L. Bissell, K. Blaum, B. Cheal, L. Filippin, K. T. Flanagan, R. F. Garcia Ruiz, W. Gins, G. Gaigalas, M. Godefroid, C. Gorges, L. K. Grob, H. Heylen, P. Jönsson, S. Kaufmann, M. Kowalska, J. Krämer, S. Malbrunot-Ettenauer, R. Neugart, G. Neyens, W. Nörtershäuser, T. Otsuka, J. Papuga, R. Sánchez, Y. Tsunoda, D. T. Yordanov
Phys. Lett. B **797**, 134805 (2019)

Laser Spectroscopy of Neutron-Rich Tin Isotopes: A Discontinuity in Charge Radii across the $N = 82$ Shell Closure
C. Gorges, L. V. Rodríguez, D. L. Balabanski, M. L. Bissell, K. Blaum, B. Cheal, R. F. Garcia Ruiz, G. Georgiev, W. Gins, H. Heylen, A. Kanellakopoulos, S. Kaufmann, M. Kowalska, V. Lagaki, S. Lechner, B. Maaß, S. Malbrunot-Ettenauer, W. Nazarewicz, R. Neugart, G. Neyens, W. Nörtershäuser, P.-G. Reinhard, S. Sailer, R. Sánchez, S. Schmidt, L. Wehner, C. Wraith, L. Xie, Z. Y. Xu, X. F. Yang, and D. T. Yordanov
Phys. Rev. Lett. **122**, 192502 (2019)

Lifetimes and g-factors of the HFS states in H-like and Li-like bismuth
V. Hannen, J. Vollbrecht, Z. Andelkovic, C. Brandau, A. Dax, W. Geithner, C. Geppert, C. Gorges, M. Hammen, S. Kaufmann, K. König, Y. A. Litvinov, M. Lochmann, B. Maaß, J. Meisner, T. Murböck, R. Sánchez, M. Schmidt, S. Schmidt, M. Steck, T. Stöhlker, R. C. Thompson, C. Trageser, J. Ullmann, C. Weinheimer, W. Nörtershäuser
J. Phys. B: At. Mol. Opt. Phys. **52**, 085003 (2019)

2018

Investigating the large deformation of the 5/2+ isomeric state in ^{73}Zn: An indicator for triaxiality
X. F. Yang, Y. Tsunoda, C. Babcock, J. Billowes, M. L. Bissell, K. Blaum, B. Cheal, K. T. Flanagan, R. F. Garcia Ruiz, W. Gins, C. Gorges, L. K. Grob, H. Heylen, S. Kaufmann, M. Kowalska, J. Krämer, S. Malbrunot-Ettenauer, R. Neugart, G. Neyens, W. Nörtershäuser, T. Otsuka, J. Papuga, R. Sánchez, C. Wraith, L. Xie, and D. T. Yordanov
Phys. Rev. C **97**, 044324 (2018)

2017

Evolution of nuclear structure in neutron-rich odd-Zn isotopes and isomers
C. Wraith, X. F. Yang, L. Xie, C. Babcock, J. Bieroń, J. Billowes, M. L. Bissell, K. Blaum, B. Cheal, L.

Filippin, R. F. Garcia Ruiz, W. Gins, L. K. Grob, G. Gaigalas, M. Godefroid, C. Gorges, H. Heylen, M. Honma, P. Jönsson, S. Kaufmann, M. Kowalska, J. Krämer, S. Malbrunot-Ettenauer, R. Neugart, G. Neyens, W. Nörtershäuser, F. Nowacki, T. Otsuka, J. Papuga, R. Sánchez, Y. Tsunoda, D. T. Yordanov
Phys. Lett. B **771**, 385-391 (2017)

High precision hyperfine measurements in Bismuth challenge bound-state strong-field QED, *J. Ullmann, Z. Andelkovic, C. Brandau, A. Dax, W. Geithner, C. Geppert, C. Gorges, M. Hammen, V. Hannen, S. Kaufmann, K. König, Y. A. Litvinov, M. Lochmann, B. Maaß, J. Meisner, T. Murböck, R. Sánchez, M. Schmidt, S. Schmidt, M. Steck, T. Stöhlker, R. C. Thompson, C. Trageser, J. Vollbrecht, C. Weinheimer, and W. Nörtershäuser*
Nat. Commun. **8**, 15484 (2017)

Development of a sensitive setup for laser spectroscopy studies of very exotic calcium isotopes
R. F. Garcia Ruiz, C. Gorges, M. Bissell, K. Blaum, W. Gins, H. Heylen, K. König, S. Kaufmann, M. Kowalska, J. Krämer, P. Lievens, S. Malbrunot-Ettenauer, R. Neugart, G. Neyens, W. Nörtershäuser, D. T. Yordanov and X. F. Yang
J. Phys. G: Nucl. Part. Phys. **44**, 044003 (2017)

Unexpectedly large difference of the electron density at the nucleus in the 4p $^2P_{1/2,3/2}$ fine-structure doublet of Ca$^+$
C. Shi, F. Gebert, C. Gorges, S. Kaufmann, W. Nörtershäuser, B. K. Sahoo, A. Surzhykov, V. A. Yerokhin, J. C. Berengut, F. Wolf, J. C. Heip, P. O. Schmidt
Appl. Phys. B **123**, 2 (2017)

2016

Isomer shift and magnetic moment of the long-lived 1/2+ isomer in $^{79}_{30}$Zn$_{49}$: Signature of shape coexistence near ^{78}Ni
X. F. Yang, C. Wraith, L. Xie, C. Babcock, J. Billowes, M. L. Bissell, K. Blaum, B. Cheal, K. T. Flanagan, R. F. Garcia Ruiz, W. Gins, C. Gorges, L. K. Grob, H. Heylen, S. Kaufmann, M. Kowalska, J. Kraemer, S. Malbrunot-Ettenauer, R. Neugart, G. Neyens, W. Nörtershäuser, J. Papuga, R. Sánchez, and D. T. Yordanov
Phys. Rev. Lett. **116**, 182502 (2016)

2015

Isotope shift of ^{40,42,44,48}Ca in the $4s\,^2S_{1/2} \rightarrow 4p\,^2P_{3/2}$ transition
C. Gorges, K. Blaum, N. Frömmgen, Ch. Geppert, M. Hammen, S. Kaufmann, J. Krämer, A. Krieger, R. Neugart, R. Sanchez, and W. Nörtershäuser
J. Phys. B: At. Mol. Opt. Phys. **48**, 245008 (2015)

An improved value for the hyperfine splitting of hydrogen-like ^{209}Bi^{82+}
J. Ullmann, Z. Andelkovic, A. Dax, W. Geithner, C. Geppert, C. Gorges, M. Hammen, V. Hannen, S. Kaufmann, K. König, Y. Litvinov, M. Lochmann, B. Maass, J. Meisner, T. Murböck, R. Sánchez, M.

Schmidt, S. Schmidt, M. Steck, T. Stöhlker, R. C Thompson, J. Vollbrecht, C. Weinheimer and W. Nörtershäuser
J. Phys. B: At. Mol. Opt. Phys. **48**, 144022 (2015)

2014

An RFQ cooler and buncher for the TRIGA-SPEC experiment
T. Beyer, K. Blaum, M. Block, Ch. E. Düllmann, K. Eberhardt, M. Eibach, N. Frömmgen, C. Geppert, C. Gorges, J. Grund, M. Hammen, S. Kaufmann, A. Krieger, Sz. Nagy, W. Nörterhäuser, D. Renisch, C. Smorra, E. Will
Appl. Phys. B **114**, 129-136 (2014)